THESIS FOR THE DEGREE OF DOCTOR OF PHILOSOPHY IN CIVIL ENGINEERING

On the impact of temperature perturbations on the creep of sensitive clay

YANLING LI

Department of Architecture and Civil Engineering

Division of Geology and Geotechnics

CHALMERS UNIVERSITY OF TECHNOLOGY

Göteborg, Sweden 2019

On the impact of temperature perturbations on the creep of sensitive clay

YANLING LI
ISBN : 978-91-7905-101-3

Doktorsavhandlingar vid Chalmers tekniska högskola
Ny serie nr. 4568
ISSN 0346-718X
Department of Architecture and Civil Engineering
Division of Geology and Geotechnics
Chalmers University of Technology
SE-412 96 Göteborg
Sweden
Telephone: +46 (0)31-772 1000

Cover:
Brief illustration on temperature perturbations for soils

Chalmers Reproservice
Göteborg, Sweden 2019

On the impact of temperature perturbations on the creep of sensitive clay

Thesis for the degree of Doctor of Philosophy in Civil Engineering
YANLING LI
Department of Architecture and Civil Engineering
Division of Geology and Geotechnics
Chalmers University of Technology

Abstract

Temperature affects the soil response, but is not fully understood and quantified and thus often ignored. The temperature fluctuations resulting from energy foundations and construction activities, such as excavations and soil stabilization, however, may lead to changes in the hydro-mechanical response of the clay. Especially, the sensitive clays that are abundant in Scandinavia, may be detrimentally affected. The fragile natural bonds between the clay platelets of sensitive clays are prone to disturbances from environmental changes, including temperature perturbations. The change in hydro-mechanical properties, such as the compressibility and the creep-rate, can affect the long-term stability of the geothermal structures. The aim of the Thesis is to study the impact of temperature perturbations on the creep of sensitive clay.

A systematic series of temperature-controlled laboratory tests (5 to 25 °C), including oedometer tests with static and cyclic thermal loading steps, has been carried out on natural and remoulded samples of natural sensitive clay from the Utby test-site in Gothenburg, Sweden. An original time-saving test protocol is developed to obtain sufficient data within the duration of the project. The results demonstrate that the influence of the temperature on the creep rate of sensitive clays depends on the amount of natural bonding. Heating increments lead to larger changes in creep rate than cooling decrements. The thermal loading cycles lead to larger permanent strains when compared to the static heating and cooling paths.

Thorough analyses of the results using the temperature-invariant rate-dependent model implemented in a multi-physics numerical framework indicates that the temperature dependency can be uniquely linked to the amount of natural bonding in the clay sample. Consequently, the temperature-invariant model is modified by correlating the apparent preconsolidation pressure with temperature and the amount of natural bonding in the clay samples. The temperature-dependent model, Creep-SCLAY1ST, improves the predictions of the mechanical response under static thermal loading considerably, whilst the modelling of the cyclic loading paths proved to be somewhat unsatisfactory. The latter is not a shortcoming of the proposed model modification, rather an intrinsic limitation of the underlying temperature-invariant model.

Keywords: geothermal, temperature, sensitive clays, natural bonding, oedometer tests, multi-physics modelling, apparent preconsolidation pressure, static thermal loading, thermal cycles

"The more I learn, the more I realize how much I don't know."

— Albert Einstein

Preface

Acknowledgements

I would like to thank my supervisors, Minna Karstunen, Jelke Dijkstra and Mats Karlsson for their precious time, patience and coaching during this journey of nearly five years. I am especially grateful to Aaro Pirhonen and Peter Hedborg who helped constructing my laboratory setup. I am also indebted to all the PhD students, post-docs and researchers I had the pleasure to work and interact with, whether they are still at Chalmers or pursueing the next step in their career. It was a great pleasure to meet and work with all of you guys.

I want to thank my friends and colleagues here in Sweden, in China and elsewhere in the world, it was an honour to meet you, to become your friend, to grow up and to become a better person, and to discover the wonderfulness of things that life can offer. You provided huge support, lovely companionship, endless patience and faithful encouragement.

Most importantly, my lovely mama and baba, thank you for bringing me to this colourful world and your unconditional love and support.

Finally, the financial support by the Swedish Research Council FORMAS under contract number 2013-771 and Chalmers University of Technology is greatly acknowledged.

Nomenclature

Other variables may appear.

Abbreviation

CRS	Constant Rate of Strain
CSL	Critical State Line
NC	Normally consolidated
OC	Overconsolidated
OCR	Overconsolidation ratio
PID	Proportional–Integral–Derivative
THM	Thermo-Hydro-Mechanical

Greek Symbols

α	Inclination of the reference surface
α_T	Thermal expansion coefficient of clay particles
α_{iso}	Inclination of the reference surface without anisotropy in the structure
α_{K0}	Inclination of the reference surface at K_0^{NC} condition
β	Visco-plastic exponent
β_T	Exponent for the temperature dependency of preconsolidation pressure
χ	Degree of bonding
χ_0	Initial degree of bonding
δ_{ij}	Kronecker delta, i,j=1, 2, 3
$\dot{\Lambda}$	Viscoplastic multiplier
η	Stress ratio q/p'
η_{K0}	Stress ratio for one-dimensional compression
κ	Slope of the swelling line from from $e - \ln p'$ curve
κ^*	Modified swelling index from $\varepsilon - \ln p'$ curve
κ_0	Initial swelling index
λ	Slope of the Normal Compression line from $e - \ln p'$ curve
λ^*	Modified compression index from $\varepsilon - \ln p'$ curve
λ_i^*	Slope of the intrinsic compression line
λ_T	Thermal conductivity
λ_{Tf}	Thermal conductivity of the fluid
λ_{Ts}	Thermal conductivity of the soil particles
μ	Viscosity of water
μ_i^*	Intrinsic creep index
Ω	Parameter for heat flow
ω	Absolute rate of rotation
ω_0	Initial phase of cyclic temperature
ω_d	Relative rate of rotation
ω_w	Water content
ϕ'	Friction angle
ρ	Density
σ'_{ij}	Effective stress state
σ'_{max}	Maximum stress state
σ'_{pc}	The apparent preconsolidation pressure
σ'_{v0}	In-situ vertical effective stress
ε^T	Thermal strain
ε^{ir}	Irreversible strain
ε_v^{ir}	Irreversible volumetric strain
ε_d	Shear strain
ε_{ij}^t	Strain after temperature change
ε_{Mij}^e	Elastic strain caused by changes in mechanical loads
ε_{Mij}^{ir}	Irreversible strain caused by changes in mechanical loads
ε_{Tij}^e	Elastic strain caused by temperature

	expansion
ε_{Tij}^{ir}	Irreversible strain caused by temperature expansion
ε_v	Volumetric strain

Roman letters

$\boldsymbol{\sigma}$	Stresses
$\dot{p}$	Increment in the effective mean stress
∇	Gradient operator $\left(\frac{\partial}{\partial x}, \frac{\partial}{\partial y}, \frac{\partial}{\partial z}\right)$
$\mathbf{f}_v$	Body force per unit mass
$\mathbf{q}$	Heat flow in the clay
$\mathbf{u}$	Water flow in the clay
A	Area passed by heating flow
a	Material parameter for temperature dependency of remoulded clays
A_T	Amplitude of the periodic temperature
b	Material parameter for temperature dependency of intact clays
C_p	Specific heat capacity
C_v	Volumetric heat capacity
$C_{v;a}$	Heat capacity of air
$C_{v;s}$	Heat capacity of soil particles
$C_{v;w}$	Heat capacity of water
D'	New diameter of clay sample
D_0	Initial diameter of clay sample
e_0	Initial void ratio
f	Yield surface
f_{ref}	Reference surface
G	Shear modulus
g	Potential surface
g_0	Gravity of earth
h'	New height of clay sample
h_0	Initial height of clay sample
I_1	First stress invariant
K	Intrinsic permeability
k	Hydraulic conductivity
K_0	Coefficient of earth pressure at rest
K_B	Bulk modulus
L	The length of the domain
M	Slope of the critical state line
m	Mass
M_c	Inclination of Critical State line in compression tests.
n	Porosity of saturated clay
O_1	The first oedometer cell
p'	Mean effective stress
p'^{eq}	Equivalent stress
p'^{eq}_{ref}	Equivalent stress of the reference surface
P'^{eq}_{Tref}	Equivalent stress at reference temperature
P'^{eq}_{T}	Equivalent stress at new temperature
p'_c	Preconsolidation pressure
Q	The amount of heat
q	Deviatoric stress
R	Heating rate in °C/hour
S_u	Undrained shear strength
S_{11}	The first step for the first oedometer cell
s_{ij}	Deviatoric stress in tensor form
T	Temperature
t	Time
T_0	Initial temperature
t_p	Period for one full cycle
T_{avg}	Average annual temperature
T_{ref}	Reference temperature
U_v	Degree of consolidation
V_a	Volume of air
V_s	Volume of soil particles
V_w	Volume of water

Contents

Abstract **i**

Preface **v**

Acknowledgements **v**

Nomenclature **vii**

Contents **ix**

Contents **1**

1 Introduction **5**
1.1 Motivation · · · · · 5
1.2 Aims and objectives · · · · · 8
1.3 Outline of the Thesis · · · · · 9

2 Thermal behaviour of natural clays **10**
2.1 Background · · · · · 10
2.2 Response of clays to temperature change · · · · · 11
2.3 Numerical Modelling · · · · · 25
2.4 Proposed research · · · · · 33

3 Experimental and numerical methodology **34**
3.1 Temperature-controlled oedometer test setup · · · · · 34
3.2 Material: Natural sensitive clay in Gothenburg area · · · · · 45
3.3 Multi-physics modelling in COMSOL · · · · · 47
3.4 Test programme · · · · · 52

4 Oedometer tests with static thermal loading **59**
4.1 Experimental results · · · · · 59
4.2 Numerical analyses of experimental results · · · · · 76

5 Thermal modelling of sensitive clays **88**
5.1 Thermal dependency of apparent preconsolidation pressure · · · · · 88
5.2 Creep-SCLAY1ST for thermal modelling of sensitive clays · · · · · 92
5.3 Verification of Creep-SCLAY1ST · · · · · 96

6 Oedometer tests with thermal loading cycles **106**
6.1 Clay with thermal cycles in laboratory tests · · · · · 106
6.2 Simulation results on oedometer tests with thermal cycles · · · · · 114
6.3 Discussion · · · · · 119

7 Conclusions and recommendations **120**

A Appendix A. Calibration of the oedometer cells **123**

B Appendix B. Experimental results with cyclic thermal loading **126**

References **131**

Contents

List of Figures

1.1 Scheme of geothermal pile system. 5
1.2 Cross-sectional view of typical heat exchangers. 6
1.3 Distribution of sensitive clays in Sweden. 7
2.1 In situ test of energy pile. 12
2.2 Temperature-controlled triaxial apparatus and its loading paths (Cekerevac and Laloui 2004). 13
2.3 Temperature control with external heating source. 14
2.4 Thermal volumetric changes of Boom clay samples at different OCR values. 17
2.5 The apparent preconsolidation pressure of intact samples. 18
2.6 Effect of temperature on the slope of the critical state line and mobilised shear strength in the $p' - q$ space. 20
2.7 Results of permeability in terms of intrinsic permeability K. 21
2.8 Creep exponent (n) versus tension load. 23
2.9 Temperature in the clay close to geothermal structures. 25
2.10 The physical interpretation of Ω and thermal anisotropy. 26
3.1 Boundary conditions in an oedometer test. 35
3.2 Temperature change with the different methods. 35
3.3 Pore pressures during fast heating and cooling. 36
3.4 Simulated pore pressures generated under different heating rates. 36
3.5 Temperature gradient within the oedometer test setup for slow heating. . 37
3.6 Oedometer test layout. 38
3.7 Temperature evolution during cooling and heating. 38
3.8 Fast thermal loading system. 39
3.9 Fast thermal loading system with pore pressure measurements. 40
3.10 Temperature regulation controlled by Labview. 41
3.11 Displacement of the test cells. 42
3.12 Sensitivity of the oedometer cells to the temperature change. 43
3.13 Pore pressure evolution during temperature change. 44
3.14 Pore pressure evolution under mechanical loading. 44
3.15 Utby test site located Northeast of Gothenburg from SGU Kartvisare. . . 46
3.16 Oedometer tests under a reference temperature of 7°C. 46
3.17 Stress state and reference surface. 50
3.18 Test analyses for for slow heating and cooling tests. 56
3.19 Average temperature for each month in a year in Gothenburg area. 57
4.1 Development of strain under mechanical loading. 60
4.2 Strain development during cooling. 60
4.3 The evaluation of compression curves. 61
4.4 Difference in heating and cooling. 62

4.5 Strain development during mechanical loading. 63
4.6 The evaluation of compression curves at different temperature. 65
4.7 Compression curves under different target temperatures. 66
4.8 Definition of the modified compression and swelling index. 67
4.9 Changes in the modified compression index with temperature. 67
4.10 Changes in the modified swelling index with temperature. 68
4.11 Variation of the hydraulic conductivity with temperature. 69
4.12 Variation of the intrinsic permeability with temperature. 71
4.13 Changes in creep rate with stress level under certain temperature. 72
4.14 Changes in creep rate as function of stress level at given temperature. . . 74
4.15 Changes in creep rate as function of temperature at given stress level. . . 75
4.16 Parameters calibration for Creep-SCLAY1S. 77
4.17 Different loading paths selected for numerical simulations. 80
4.18 Remoulded sample from the depth of 6 m, loading path O_1. 81
4.19 Remoulded sample from the depth of 9 m, loading path O_1. 81
4.20 Intact sample from the depth of 6 m Cell 04, loading path O_1. 82
4.21 Intact sample from the depth of 6m Cell05, loading path O_2. 83
4.22 Intact sample from the depth of 6 m Cell 06, loading path O_3. 83
4.23 Intact sample from the depth of 9 m Cell 10, loading path O_1. 85
4.24 Intact sample from the depth of 9 m Cell 11, loading path O_2. 85
4.25 Intact sample from the depth of 9 m Cell 12, loading path O_3. 86
4.26 Change in void ratio under thermal load steps for samples from a depth of 6 m. 87
4.27 Change in void ratio under thermal load steps for samples from a depth of 9 m. 87
5.1 Change in void ratio when loading beyond the apparent preconsolidation pressure. 89
5.2 Sketch for isotropic compression under different temperatures. 89
5.3 Temperature dependency of the apparent preconsolidation pressure for samples with different amounts of bonding. 91
5.4 Determination of parameters a and b for thermal dependency. 91
5.5 Predictions with the two power relationships as a function of the amount of bonding. 93
5.6 Stress state and reference surface 93
5.7 Sketch for isotropic compression. 95
5.8 Results on sample remoulded from 6 meter Cell 04 with Creep-SCLAY1ST. 97
5.9 Results on remoulded sample from 9 meter Cell 10 with Creep-SCLAY1ST. 97
5.10 Change in void ratio under thermal loading at a stress level just after the apparent preconsolidation pressure. 98
5.11 Results on intact sample from 6 meter Cell04 with Creep-SCLAY1ST. . . 98
5.12 Results on intact sample from 6 meter Cell 05 with Creep-SCLAY1ST. . . 99
5.13 Results on intact sample from 6 meter Cell 06 with Creep-SCLAY1ST. . . 99
5.14 Results on intact sample from 9 meter Cell 10 with Creep-SCLAY1ST. . . 100
5.15 Simulation results on intact sample from 9 meter Cell 11 with Creep-SCLAY1ST. 101

5.16 Simulation results on intact sample from 9 meter Cell 12 with Creep-SCLAY1ST. 101
5.17 Results on thermal loading steps with Creep-SCLAY1ST. 102
5.18 Boundary conditions for CRS and undrained triaxial tests. 103
5.19 Simulations of CRS test under different temperatures with Creep-SCLAY1ST. 103
5.20 Simulations of CRS test with different amounts of initial bonding with Creep-SCLAY1ST. 104
5.21 Simulation results of undrained triaxial shearing at different temperatures with Creep-SCLAY1ST. 105
6.1 Boundary conditions for oedometer tests with thermal cycles. 107
6.2 Temperature in oedometer tests with temperature cycles. 108
6.3 Pore pressure and void ratio of samples at 60 kPa during thermal cycles with a period of 12 hours. 109
6.4 Pore pressure and void ratio of samples under different stress levels during thermal cycles with a period of 12 hours. 110
6.5 Pore pressure and change in void ratio in oedometer tests with temperature cycles with a period of 12 hours for intact clay. 111
6.6 Pore pressure and change in void ratio in oedometer tests with temperature cycles with a period of 12 hours for remoulded clay. 112
6.7 Strain evolution under mechanical loading after cyclic thermal loading. . . 113
6.8 The area that is influenced by energy pile penetration and temperature change. 114
6.9 Excess pore water pressures resulting from thermal loading cycles simulated with Creep-SCLAY1S and Creep-SCLAY1ST. 115
6.10 Cyclic 1D compression curve in p'-q space. 116
6.11 Simulated p'-q response for thermal cyclic oedometer tests using Creep-SCLAY1S & Creep-SCLAY1ST. 117
6.12 Simulated time-void ratio curves for thermal cyclic oedometer tests using Creep-SCLAY1S & Creep-SCLAY1ST. 118
6.13 Simulated time-compression curves for thermal cyclic oedometer tests using Creep-SCLAY1S & Creep-SCLAY1ST - complete time series for all load steps. 118
A.1 Calibration on Cell 04 to Cell 07. 123
A.2 Calibration on Cell 08 to Cell 11. 124
A.3 Calibration on Cell 13 to Cell 15. 125
B.1 Temperature in oedometer tests with temperature cycles for intact sample. 126
B.2 Temperature in oedometer tests with temperature cycles for remoulded sample. 127
B.3 Pore pressure and void ratio of samples under different stress levels during thermal cycles, t_P =4 hours. 128
B.4 Pore pressure and void ratio of samples under different stress levels during thermal cycles, t_P =8 hours. 129
B.5 Pore pressure and void ratio of samples under different stress levels during thermal cycles, t_P =16 hours. 130

List of Tables

1.1 Sensitivity of natural clays. (Rankka et al. 2004) 7
2.1 Thermal consolidation parameters at 20°C. 11
2.2 Temperature-controlled laboratory tests on clays. 15
2.3 Dynamic viscosity and density of water (Korson et al. 1969). 21
2.4 Engineering mechanical properties of soil under temperature change. . . . 22
2.5 Thermal properties for soil at 20°C (Tarnawski and Wagner 1991). 27
2.6 Yield surfaces and hardening laws for temperature-dependent constitutive models for clays. 31
3.1 Basic index properties of Utby clay. 45
3.2 Measured and (estimated) physical and thermal properties of Utby clay. . 47
3.3 Test procedure for oedometer cooling tests for the clay from one depth. . 55
3.4 Applied temperatures in heating and cooling tests. 55
3.5 Plan for data analysis after a group of tests. 57
3.6 Cyclic loading process for samples from one depth. 58
4.1 Creep-SCLAY1S parameters for Utby clay. 78
4.2 Additional parameters for the model simulations. 78
4.3 Selected tests for numerical simulations. 80

1 Introduction

1.1 Motivation

Given the current trend of global warming, sustainable development is increasingly important. Geothermal structures, such as energy foundations, will help to provide energy in an environmentally friendly way by exploiting the shallow subsurface (i.e. < 100 m). The temperature in the ground close to the surface is affected by the ambient temperature of the air and the changes with weather. The temperature below a certain depth in the subsurface, however, is constant, and similar to the average air temperature over the year. This depth depends on the thermal properties of the ground, hence the soil type. The consequence is that in the winter or the summer, the temperature in the ground is either higher or lower than the air temperature, respectively. This temperature difference can be utilised in making heating, ventilation, and air conditioning (HVAC) systems for buildings more efficient (Arson et al. 2013; Bourne-Webb, Amatya, and Soga 2012; Florides and Kalogirou 2007; Laloui and Di Donna 2011; Suryatriyastuti et al. 2012). A possible solution for an energy foundation is to equip piles with additional thermal loops as shown in Fig. 1.1. In these, so called energy- or geothermal piles, closed loops of pipes are placed in which a fluid is circulated to extract and store heat in the pile itself, and the soil surrounding it, as illustrated in Fig. 1.2. In these systems, heat subsequently transfers from the fluid through the pipes and the pile itself into the subsoil.

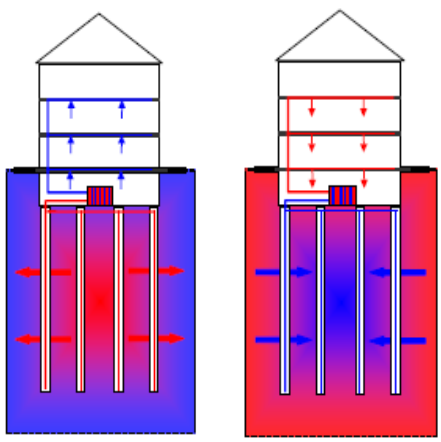

Figure 1.1: Scheme of geothermal pile system: (a) Energy storage; (b) Energy extraction.

The temperature of the the material surrounding the heat exchanger is influenced by the fluid flow in the pipe and, depending on the temperature difference, undergoes a heating or cooling process. Most fine-grained soils that experience a change in temperature

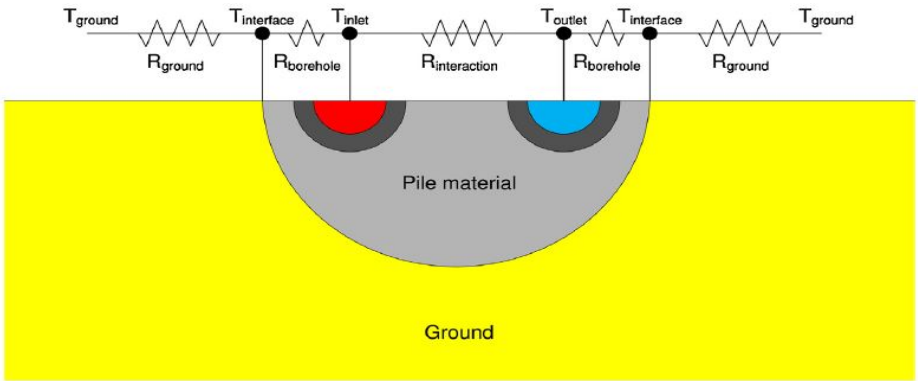

Figure 1.2: Cross-sectional view of typical heat exchangers(Abdelaziz et al. 2014).

generate excess pore water pressures, due to the difference in the thermal expansion coefficients between the pore water and the minerals of which most soil particles are composed of. Because of the low hydraulic conductivity, stiff and or compacted clays are used as barrier for nuclear waste repositories far below the ground surface (>200 m). In these applications the temperature can be high around the heating source, sometimes even sufficiently high (70 to 92°C) to induce failure (Hueckel and Pellegrini 1992). Unlike nuclear waste repositories, energy foundations, such as geothermal piles (Fig. 1.1), only change the temperature of the surrounding soil in a limited temperature range (0 to 50°C). In this case, the temperature change is unlikely to induce failure in the soil resulting from generating excess pore water pressures. For sensitive natural clays, however, a modest change in the effective stress or the apparent preconsolidation pressure is sufficient to change the material behaviour considerably. This in turn can gradually degrade the initial amount of natural bonding, and hence may affect the mechanical properties, such as the emerging creep rate, the stiffness and the (undrained) strength.

Previously, the major concerns of geothermal piles have included the design, the energy efficiency and the added costs of the complete system. Furthermore, most geothermal piles have been installed in stiff soils (Dehkordi and Schincariol 2014; Mimouni and Laloui 2014). In Sweden, however, soft sensitive clays with a large natural water content are very common. Although the water content might be beneficial for energy storage, the thermo-hydro-mechanical response of the sensitive clays to the temperature change around geothermal piles, and its effect on the foundation, is less well understood.

Sensitive clay is a type of clay where the shear strength reduces to a very small fraction of its original value when sheared to large magnitudes of strain at constant water content (remoulded). Sensitivity is defined as the ratio of the peak strength of the soil in its natural undisturbed state to that in the remoulded state at the same water content. The sensitivity varies considerably with the type of clay (and the tests conducted to determine it) (Table 1.1), ranging from 2 to a few hundreds as shown in Fig. 1.3. Depending on the formation and depositional history, marine clays can transfer to quick clays (Mitchell

and Soga 2005). Quick clays are ubiquitous in Scandinavia and Canada, which have comparable geological and climatic conditions. In Sweden, the largest sensitive clay deposits are found at elevations below approximately 80% of the level of the highest historic shoreline (Rankka et al. 2004). Fig. 1.3 shows the occurrence of quick clay, the red circle represents the Gothenburg area.

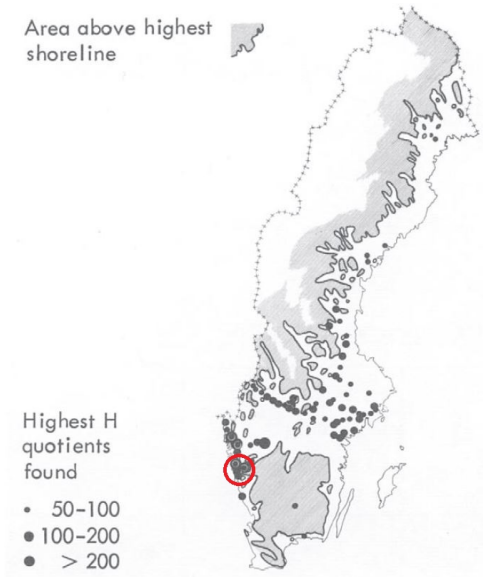

Figure 1.3: Distribution of sensitive clays in Sweden (Jerbo and Hall 1961).

Table 1.1: Sensitivity of natural clays. (Rankka et al. 2004)

Clay type	Term	Sensitivity
Overconsolidated, low to medium plastic clays	Low sensitivity	<8
Normally consolidated, medium plastic clays	Medium sensitivity	8-30
Marine Clays	High sensitivity	>30

For soft sensitive clays, such as those found near Gothenburg, long-term deformation behaviour is one of the main concerns. The impact of temperature on the long-term behaviour of sensitive clays is still subject to research. Several researchers, e.g. Burghignoli et al. (1992) and Towhata, Kuntiwattanakul, Seko, et al. (1993) have shown that thermal loads produce an acceleration of the mechanical creep phenomena. This implies for soft sensitive clays that a small temperature change, e.g. from an energy foundation, could cause unexpected large additional settlements.

Rate-dependency (creep) and the degradation of the initial amount of bonding, called destructuration, are two of the most important mechanisms that differentiate sensitive

clays from other types of clays. A large number of tests (including temperature-controlled triaxial tests and oedometer tests) have been conducted to study the response of soil under thermal loading over a large temperature range and at high stress levels, representative for nuclear waste repositories. In contrast, only a very limited number of tests have been conducted on sensitive natural clays to study the long-term rate- and temperature-dependent behaviour in a temperature range that is representative for energy foundations. Furthermore, it is important to not only study the emerging creep rate as function of temperature, but also as function of temperature loading history.

1.2 Aims and objectives

The aim of this Thesis is to study the rate-dependent behaviour of sensitive natural clay under both static and cyclic thermal loading. This is achieved by using a combination of laboratory testing, thermo-hydro-mechanical modelling, as well as constitutive model development. A systematic series of temperature-controlled oedometer tests are conducted in the temperature range of 5°C to 25°C on intact and remoulded samples of a natural sensitive clay from Gothenburg.

In order to study the influence of static and cyclic thermal loading on the behaviour of a sensitive natural clay, an experimental programme is designed to study the following aspects:

- The volumetric strains and the excess pore pressures during heating and cooling under relevant constant stress state;
- The evolution of hydraulic conductivity and consolidation during thermal loading (heating and cooling) and mechanical loading;
- The temperature dependency of the hydro-mechanical properties of the soil, such as the apparent preconsolidation pressure, stiffness and creep properties;
- The emerging creep rate (both natural and intrinsic) under temperature change.

Furthermore, to interpret the gathered experimental results, we:

- Use advanced constitutive modelling for sensitive natural clay to predict its coupled thermo-hydro-mechanical behaviour;
- Modify a temperature-invariant constitutive model in order to incorporate the influence of temperature;
- Use both temperature-invariant and temperature-dependent models to predict the response of sensitive clays subjected to combined mechanical and thermal loading.

A few limitations apply:

- The focus is on displacement and creep, not strength.
- The focus is on saturated sensitive clays which are lightly overconsolidated;
- The temperature range is selected to be representative for energy foundations, and is therefore relatively small.

1.3 Outline of the Thesis

- Chapter 2. –*Thermal behaviour of natural clays* – In this Chapter, the general background related to the thermal response of soft soils and the expected thermal regime around energy foundations are discussed. A combination of relevant experimental evidence and modelling strategies are summarised.
- Chapter 3. –*Experimental and numerical methodology*– The experimental methodology will be explained and the performance the testing system is demonstrated.
- Chapter 4. –*Oedometer tests with static thermal loading*– A systematic series of slow monotonic cooling and heating tests on intact and remoulded samples is presented and analysed using the temperature-invariant Creep-SCLAY1S model implemented in a fully coupled multi-physics framework.
- Chapter 5. –*Thermal modelling of sensitive clays*– A temperature-dependent model extension (Creep-SCLAY1ST) is developed based on the experimental data presented in Chapter 4.
- Chapter 6. –*Oedometer tests with thermal loading cycles*– The effect of thermal cyclic loading is investigated experimentally, and further analysed using the Creep-SCLAY1S and Creep-SCLAY1ST models.
- Chapter 7. –*Conclusions and recommendations*– Conclusions and recommendations for future research.

2 Thermal behaviour of natural clays

2.1 Background

It is impossible to eliminate temperature changes in natural clays, as even the ambient temperature changes daily. When soils are sampled for testing from a given soil layer, they may have a different temperature than the temperature used in the laboratory (Campanella and Mitchell 1968). Construction activities, such as deep excavations, expose soils to different temperatures than they have had in the past. In addition to these temperature changes caused by the natural heating or cooling, the clays are subjected to even larger temperature disturbances because of human activities in energy projects. For example the (shallow) subsurface is exploited as a geothermal resource (Amatya et al. 2012; Bourne-Webb, Amatya, Soga, et al. 2009; Brandl 2006; Dupray et al. 2014; Gera et al. 1996; Knellwolf et al. 2011; Loveridge and Powrie 2013; McCartney, Sanchez, et al. 2016), or alternatively clays with low permeability are used as an impermeable barrier for nuclear waste storage and disposal (François, Laloui, and Laurent 2009; Gens, Vaunat, et al. 2007; Hueckel and Baldi 1990; Sultan et al. 2002). The properties and responses of the clays under non-isothermal conditions are of a concern in the situations above.

Under temperature change, or during thermal loading of a saturated clay, the soil particles and the pore fluid are the two components that respond to the temperature change. The properties of clay as a porous medium depends highly on the fraction and the type of soil particles and porous fluid (usually water) (Abuel-Naga, Bergado, and Bouazza 2008). During thermal loading (e.g. heating), excess pore pressures are often generated, because of the difference between the thermal expansion coefficients of these two components (soil particles and fluid) in saturated clays. The magnitude of this pore pressure change depends on the hydraulic conductivity, the rate of the thermal loading and the drainage conditions. Among the natural clays, sensitive clays have a large amount of natural bonds between the particles. These bonds depend strongly on the age of the clay, and the sedimentary and geo-chemical environment, and can be easily influenced by the environmental change (such as mechanical loads, temperature, chemical components in water and bacteria). Slow reorganisation of the particles in sensitive clays occurs with time, and can even be accelerated by disturbances, such as changes in temperature or effective stress. Consequently, the macro-level stress-strain-time behaviour of sensitive clay can change as a result of disturbances. In this Chapter, we focus on the situations where temperature is the source of these disturbances.

To investigate the complex processes in natural clays due to temperature change, temperature-controlled laboratory tests have been carried out on different types of clays. Most of these tests are oedometer tests (Eriksson 1989; Towhata, Kuntiwattanakul, Seko, et al. 1993), CRS (Constant Rate of Strain) tests (Marques et al. 2004; Moritz 1995; Tidfors and Sällfors 1989), direct shear tests (Noble and Demirel 1969; Yavari et al. 2016) and triaxial tests (Cekerevac and Laloui 2004; Sultan et al. 2002) that aim to study the basic soil

response under thermal loading, or at different temperatures. The published laboratory observations are, however, somewhat contradictory and inconclusive, which demonstrates that the features of the mechanical behaviour of soil under thermal loading, such as creep rate, shear strength, stiffness, permeability and so forth, are not fully understood. Regardless, thermal constitutive models have been proposed to capture the response of clays to temperature change, based on the comparisons between laboratory and simulation results.

In this Chapter, a brief overview on previous studies on the response of clays to temperature is discussed, focussing on laboratory tests and numerical studies on saturated clays.

2.2 Response of clays to temperature change

The first reaction of the two components in clays, the clay particles and the pore fluid, to temperature change is to expand (contract) upon heating (cooling), just like most of the natural materials. This means that all the components in saturated clays deform, and the magnitude of this deformation can be deduced from the thermal expansion coefficient α_T. The volumetric thermal expansion coefficient α_T is expressed as the volumetric strain taking place under one degree of temperature change. The thermal expansion coefficient α_T for water, which is the most common fluid in the clay, is much higher than that of the mineral particles (which in turn varies dependent on the mineral), see Table 2.1. The bulk modulus K_B for clay particles is, however, much higher than that of the water, as listed in Table. 2.1 for Kaolinite. Bulk modulus K_B represents the ratio between the increment of mean effective stress to the increment of volumetric strain ($\Delta p'/\Delta\varepsilon_v$). Consequently, under temperature change, excess pore pressures can be generated, because water expands more than the soil particles. Once these excess pore pressures cannot dissipate, there is a change in effective stresses that ultimately results in the deformation of the clay skeleton. To investigate the behaviour of clays in a geothermal system, field tests have

Table 2.1: Thermal consolidation parameters at 20°C.

Properties	Volumetric thermal expansion α_T	Bulk modulus K_B
Unit	$\times 10^{-5\circ} C^{-1}$	GPa
Mineral Particles	1.3 - 5.0	35.7-62.2 (Kaolinite)
Water	20.7	2.2 (at 45 °C)

been made by observing of the response of natural sedimentary clays subject to heating (Akrouch et al. 2014; Bourne-Webb, Amatya, Soga, et al. 2009; François, Laloui, and Laurent 2009; Gabrielsson et al. 1997; Popiel et al. 2001). For example, the clays around nuclear repositories, energy storage and energy pile foundation have been studied with field measurements (Akrouch et al. 2014; Bernier et al. 2007; Gabrielsson et al. 1997) as shown in Fig. 2.1. Most of the tests conducted have focused on the energy efficiency and geotechnical behaviour of the piles (Brandl 2006).

The boundary conditions (for water, temperature and mechanical loads), however, are not easy to controll in the field. For example, the effective stresses and the temperature change simultaneously in the clays around geothermal structures. Furthermore, the thermal strains cannot be measured directly, as the water boundary is partially drained, and depends on the heating and cooling rate. Because of the limitations of testing time,

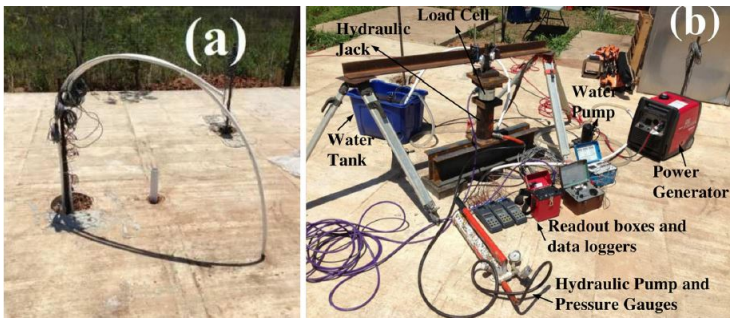

Figure 2.1: In situ test of energy pile. (Akrouch et al. 2014)

measurements, boundary conditions, site and etc., the laboratory tests out-number the field tests. Temperature-controlled laboratory test are a useful tool to systematically study the behaviour of clays under controlled conditions by isolating the change of one specific variable (for example temperature, mechanical load, boundary conditions, solution of the water bath, salinity of the water bath and etc.) from other variables. Thermal loads, similarly to the mechanical loads and other environmental changes, can work as an external variable. The following section focuses on the temperature-controlled laboratory tests that have studied the thermal response of clays. The observations on the basic properties and mechanical parameters of soil thermal under non-isothermal conditions are summarized and discussed.

2.2.1 Overview of the temperature-controlled laboratory tests

A large body of research has been carried out by performing different types of temperature-controlled laboratory tests, to study the stiff clay response for high temperature range for nuclear waste repositories (Baldi et al. 1988), and to investigate the general behaviour of clays under temperature change (Cekerevac and Laloui 2004). Early works on the soil behaviour under temperature loading have studied the influence of temperature on volumetric and strength parameters of soil samples during sampling and transportation (Campanella and Mitchell 1968), because it is believed that the heating can lead to a change in the shear strength, which is most relevant for deep excavations.

Because of pore pressure changes due to the dissimilarities in the thermal expansion coefficient and the bulk modulus of the mineral particles and the water, the temperature-controlled laboratory tests are divided into two categories: drained tests where excess

and negative pore pressure can dissipate, for example oedometer tests (Abuel-Naga, Bergado, and Bouazza 2008; Abuel-Naga, Bergado, Bouazza, and Ramana 2007; François and Laloui 2010; Towhata, Kuntiwattanakul, Seko, et al. 1993; Ye et al. 2013), CRS tests (Moritz 1995) and triaxial tests (usually isotropic compression) with open water boundaries (Cekerevac and Laloui 2004; Delage, Sultan, et al. 2000; N. Tanaka et al. 1997); and undrained tests where the water boundaries are closed (Abuel-Naga, Bergado, and Bouazza 2007; Hueckel and Pellegrini 1992), for example triaxial tests that combine heating, cooling and shearing with complex loading path as shown in Fig. 2.2(b). In triaxial tests, not only the loading path and drainage conditions can be controlled, but also the thermally induced volumetric deformations under drained conditions and thermally induced pore water pressures under undrained condition can be obtained (Abuel-Naga, Bergado, and Bouazza 2007).

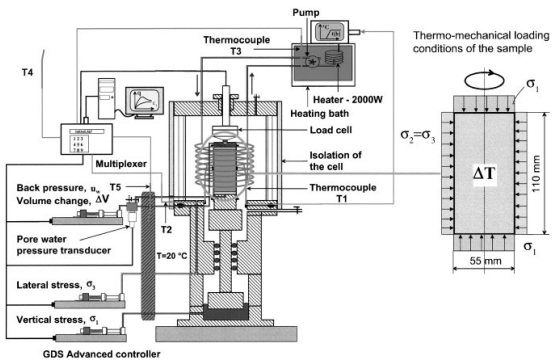

(a) Triaxial apparatus with tempreature control

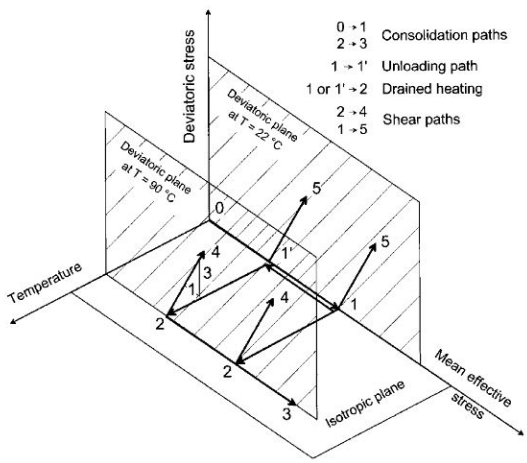

(b) Thermo-mechanical loading paths

Figure 2.2: Temperature-controlled triaxial apparatus and its loading paths (Cekerevac and Laloui 2004).

In most cases, the temperature started from the room temperature, and was controlled between the freezing and boiling point of the pore fluid to avoid a phase change. The representative temperature-controlled laboratory tests on saturated clay (both natural and reconstituted) are summarized in Table. 2.2. The method to control the temperature varies between different tests. It is most common to change the temperature of the samples by measuring and adjusting the temperature of the water bath surrounding a clay sample, either by heating the water directly in the water bath (Fig. 2.2(a)) or by pumping the water from a temperature-controlled source (Fig. 2.3).

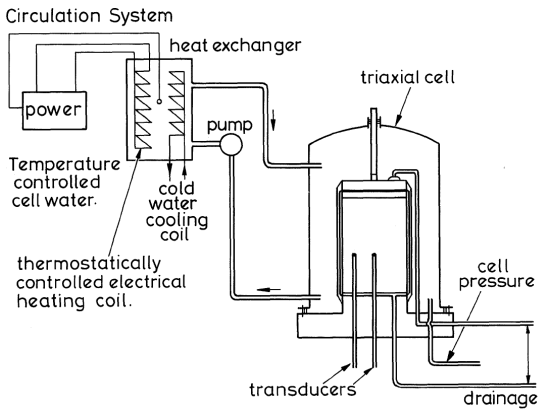

Figure 2.3: Temperature control with external heating source (Savvidou and Britto 1995).

With respect of stress states and temperatures, two main types of loading paths have been used to change just one variable at a time during the tests to investigate the temperature-dependent soil response: heating up or cooling down the sample at constant stress levels; and isothermal mechanical loading the sample at different temperatures. The representative results are discussed in the following.

Table 2.2: Temperature-controlled laboratory tests on clays.

Clay source	Sample type	Water content (%)	Temperature (°C)	Tests type	References
Illite (Pacific)	Remoulded	75	4 - 200	UH, CIUC	Houston et al. 1985
Boom (Belgium)	Intact	26			
Pontida (Italy)	Remoulded	30	20 - 200	UH, UC	Baldi et al. 1988
Kaolin	Remoulded	35			
Luleå (Sweden)	Intact	105 - 110	5 - 50	Oedometer, Creep	Eriksson 1989
Bäckebol (Sweden)		76 - 82			
Upplands (Sweden)		50 - 60			
Värnamo (Sweden)	Intact	40 - 50	25 - 55	CRS, Oedometer	Tidfors and Sällfors 1989
Välen (Sweden)		100 - 130			
Gunilse (Sweden)		30 - 35			
Boom (Belgium)	Intact	26		DH,DC	
Pasquasia (Italy)	Intact	13	18 - 115	DH	Hueckel and Baldi 1990
Pontida (Italy)	Remoulded	30		DH, DC, CIDC, CIUC	
Boom (Belgium)	Intact	Low	21 - 96	UH, UC (cyclic)	Hueckel and Pellegrini 1992
Pasquasia (Italy)		13			
Todi (Italy)					
Fiumicino (Italy)	Remoulded	-	18 - 58	DH, DC (cyclic)	Burghignoli et al. 1992
Bologna (Italy)					
MC clay	Remoulded	-	20 - 90	DH (Oedometer)	Towhata, Kuntiwattanakul, Seko, et al. 1993
Bentonite					
Berthierville		62			
Louiseville	Intact	70	5 - 35	CRS	Boudali et al. 1994
Saint-Jean-Vianney		42			
Linköping (Sweden)	Intact	77-87	8 - 70	CRS, UH, CAUC	Moritz 1995
Kaolin	Remoulded	49 - 62	20 - 90	CIUC	Kuntiwattanakul et al. 1995

Kaolin	Remoulded	-	20 - 80	DH, UH	Savvidou and Britto 1995
Heneda (Japan)	Remoulded	-	20, 50, 80	CRS	Akagi and Komiya 1995
Middleton Peat (USA)	Intact	491 - 624	14 - 66	DH	Fox and Edil 1996
Sand-bentonite buffer (Canada)	Remoulded	-	65 - 100	CIUC, CIDC	Lingnau, Graham, Yarechewski, et al. 1996
Boom	Intact	23 - 26	20 - 110	CIUC	De Bruyn and Thimus 1996
Illitic clay	Remoulded	-	28 - 100	DH, UH, UC, CIUC	N. Tanaka et al. 1997
Boom	Intact	24 - 30	20 - 100	DH	Delage, Sultan, et al. 2000
Boom	Intact		20,80,100	CIDC	Sultan et al. 2002
Todi (Italy)	Remoulded				
Fiumicino (Italy)	Intact	-	18 - 60	DH,DC,UN,UC (cyclic)	Burghignoli et al. 2000
Bologna (Italy)	Intact				
Illite	Remoulded	-	28, 65, 100	DH, UH	Graham et al. 2001
Kaolin	Remoulded	35 - 37	22, 60, 90	DH, CIDC	Cekerevac and Laloui 2004
St-Roch-de-l'Achigan clay (Canada)	Intact	75 - 92	10 - 50	CRS, CIUC	Marques et al. 2004
Bangkok (Thailand)	Intact	90 - 95	25 - 90	DH, DC	Abuel-Naga, Bergado, Bouazza, and Ramana 2007
GMZ-Bent(China)	Intact	-	25 - 80	DH, DC, Cyclic	Ye et al. 2013
Geneva (Switzerland)	Intact	22 - 28	5 - 60	Oedometer, Cyclic	Di Donna and Laloui 2015
Kaolin	Remoulded	-	5 - 40	Direct shear	Yavari et al. 2016

DH (Drained Heating), DC (Drained Cooling), UH (Undrained Heating), UC (Undrained Cooling)
CIUC (Consolidated Isotropic Undrained Compression), CADE (Consolidated Anisotropic Drained Extension)

2.2.2 Thermal loading under constant mechanical loads

Thermal strain ε^T

As already discussed, during thermal loading, the first response of a clay is expansion or contraction. This expansion or contraction leads to the deformation of the clay that, depending on the initial structure of the clay and the temperature increment, is either reversible or irreversible. The thermal strain relates to the current stress level, the stress history, the current temperature and the temperature history. The measurements of volumetric strains under temperature change are essential for developing temperature-dependent constitutive models. These can be obtained from drained heating tests by measuring the deformation of sample or the amount of water that has been expelled out of the sample.

For most of the clays, with open drainage boundary, irreversible strains will be left after a heat-cooling cycle as shown by Sultan et al. (2002) in Fig. 2.4. The magnitude of this irreversible thermal strain is related to the stress history. In the laboratory tests, drained heating has different influence on OC (overconsolidated) and NC (normally consolidated) clay, as illustrated in Fig. 2.4 (Abuel-Naga, Bergado, Bouazza, and Ramana 2007; Baldi et al. 1988; Cekerevac and Laloui 2004; Demars and Charles 1982). For most of the tests, thermal expansion is observed in overconsolidated clay in the early heating period and contraction is observed when the clay is heated with high temperature (Hueckel and Pellegrini 1991).

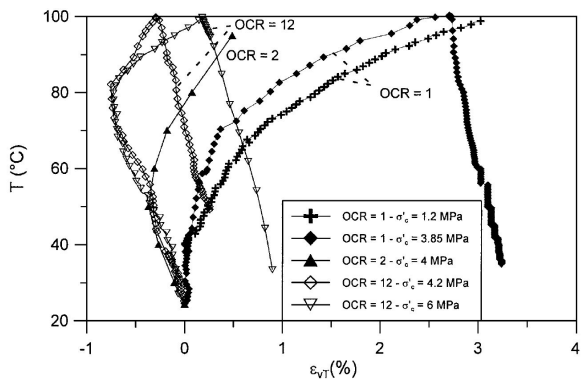

Figure 2.4: Thermal volumetric changes of Boom clay samples at different OCR values (Sultan et al. 2002).

The apparent preconsolidation pressure σ'_{pc}

Because of the irreversible strains in the cooling and heating process, the apparent preconsolidation pressure observed in the laboratory changes. It is generally proven that the apparent preconsolidation pressure decreases with increasing temperature (Abuel-Naga, Bergado, Bouazza, and Ramana 2007; Moritz 1995; Towhata, Kuntiwattanakul,

Seko, et al. 1993; Tsutsumi and H. Tanaka 2012). Heating causes hence quasi-softening behaviour in clay. Because of the limitation of time in incremental loading oedometer tests, most of the correlations between the apparent preconsolidation pressures σ'_{pc} and the temperature are drawn from CRS tests. One of the results for soft clay is shown in Fig. 2.5.

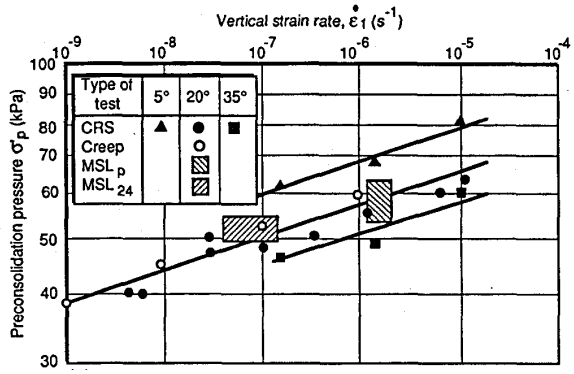

Figure 2.5: The apparent preconsolidation pressure of intact samples (Leroueil and Soares Marques 1996).

There are two processes going on in the clay when a thermal load is applied on the macroscopic level: thermal softening and volumetric strain hardening. It is generally agreed that the preconsolidation pressure deceases because of the softening caused by heating. It means that if the soil is normally consolidated and subjected to heating, the apparent preconsolidation pressure (σ'_{pc}) is smaller than the stress that it is subjected to (σ'_v). Thus, irrecoverable strains develop to partially compensate for the increase in stresses or the decrease in the preconsolidation pressure (Hueckel and Baldi 1990). If the clay is highly overconsolidated, thermal expansion is observed upon increasing temperature. When the reduced apparent preconsolidation pressure matches the current stress that the clay is subjected to, thermal contraction is expected.

When clay samples are heated with closed drainage boundaries, the observed strains are mainly related to the expansion of water (Kuntiwattanakul et al. 1995). The yielding of the clay sample is caused by the generation of the excess pore pressure (increase in Δu and thus increasing q/p') when the external loads are kept constant (Hueckel, François, et al. 2009). Failure of clay is even more likely to happen under undrained heating, because of the combination of decrease in the apparent preconsolidation pressure and increase in q/p' (Hueckel and Pellegrini 1991).

2.2.3 Mechanical loading under constant temperature

When temperature is kept constant, the mechanical and hydraulic properties such as the modified swelling index κ^* and the modified compression index λ^*, the creep rate $C_{\alpha e}$, the permeability K (hydraulic conductivity k) and the shear strength S_u (drained and undrained) under different temperature can be evaluated. For example, in temperature-controlled oedometer or CRS tests, parameters such as the compression and the swelling index can be deduced directly from compression (or stress-strain) curves. The permeability and consolidation coefficients can be derived from time-displacement curves. The laboratory tests are carried out in the same way as traditional tests but at different temperatures. The correlation between temperature and these mechanical properties are summarized in Table. 2.4.

Compression index λ^* and swelling index κ^*

The slopes of the swelling line κ and the Normal Compression line λ are defined in Cam-Clay model as $-\Delta e/\Delta \ln p'$, where e is the void ratio, and are used to describe the compressibility of clays in the elastic and plastic range, respectively. Most compression tests under drained conditions show that λ is independent of temperature (Cekerevac and Laloui 2004; Graham et al. 2001; Mitchell 1969; Plum and Esrig 1969; Sultan et al. 2002). The observations for κ -values, however, varies between different studies. The initial stiffness, represented by the reverse of swelling index is higher for the samples that had been loaded with one thermal cycle (thermally-overconsolidated) than those that were tested under room temperature (Burghignoli et al. 2000; Kuntiwattanakul et al. 1995). For example, the apparent shear modulus seems to increase with temperature (De Bruyn and Thimus 1996; Houston et al. 1985). This indicates that the heating history can affect the stiffness, and that the changes are not be reversed by cooling. In contrast, in some other tests, the initially heated and then cooled normally consolidated sample still exhibited the same stiffness as the heated sample (Abuel-Naga, Bergado, and Lim 2007; Sultan et al. 2002). In some of the numerical simulations, the initial stiffness is deceasing with increasing temperature as the correlation between temperature and swelling index is defined as Eq.(2.1), where B is a material constant measured in laboratory tests for different types of samples.

$$\frac{\kappa}{\kappa_0} = 1 + Bln(\frac{T}{T_0}) \tag{2.1}$$

The slope of critical state line M, friction angle ϕ and undrained shear strength S_u

The shear strength (both drained and undrained) is one of the most important parameters for the design of geotechnical structures. The drained and undrained shear strengths under different temperatures can be obtained directly from the laboratory tests with thermal control. In general, the emerging shear strength depends on the initial stress state, the stress path to failure and the critical state line.

The inclination of the critical state line M can be derived from the friction angle ϕ' using $M = 6\sin\phi'/(3 \pm \sin\phi')$ or obtained from the $p' - q$ figure from triaxial tests. The drained and undrained triaxial shear tests conducted under different temperatures show that the inclination of the critical state line M is temperature-invariant (Abuel-Naga, Bergado, and Lim 2007; Hueckel and Baldi 1990; N. Tanaka et al. 1997) as shown in Fig. 2.6, even though a few tests (Cekerevac and Laloui 2004) do suggest that the friction angle might be influenced by the temperature change.

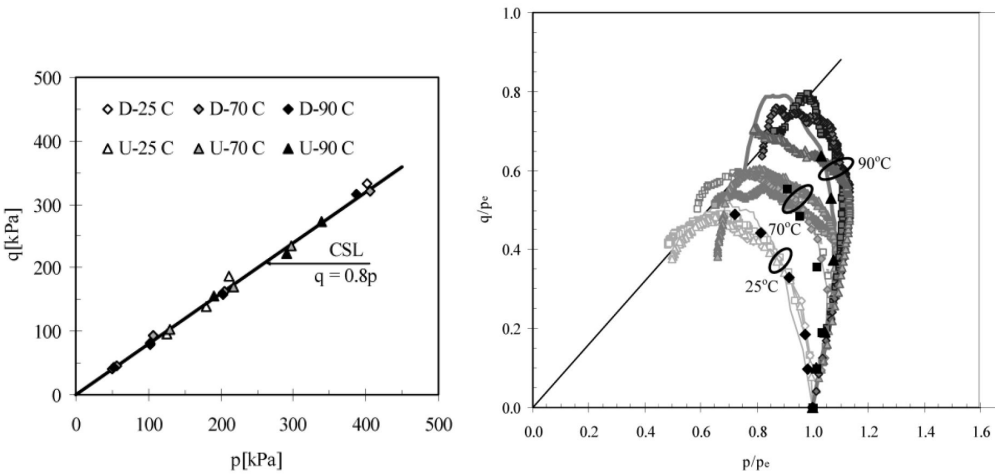

(a) Inclination of CSL

(b) Shear strength under different temperature

Figure 2.6: Effect of temperature on the slope of the critical state line and shear strength in the $p' - q$ space (Abuel-Naga, Bergado, and Lim 2007).

The mobilised shear strength, however, depends highly on the loading path, as well as the temperature and loading histories (drained or undrained consolidation) according to the studies carried out under non-isothermal conditions. Contradictory conclusions are drawn by different researchers based on their laboratory results (Table. 2.4). The temperature history is important for the mobilised shear strengths, as the thermally-overconsolidated clay samples (i.e. sample that have been subjecting to higher temperature than the current temperature) exhibit larger shear strengths than those prepared in normal temperature (Kuntiwattanakul et al. 1995). The same applies to the mechanical loading history: the apparent shear strength increases with temperature for normally consolidated clay, but deceases for overconsolidated clays (Hueckel and Baldi 1990). The shear strength under different temperature depends also on the loading path. The mobilised drained shear strength seems to increase with temperature, whilst the undrained shear strength decreases with temperature (Abuel-Naga, Bergado, and Lim 2007; Houston et al. 1985). In some triaxial shear tests, the shear strength appear to be temperature-invariant (Graham et al. 2001; Houston et al. 1985). The unclear trends on the development shear strengths as a function of temperature shows the necessity of carrying out systematic tests with a

thorough test procedure, supported by numerical modelling to explain the phenomena.

Permeability K and hydraulic conductivity k

In geotechnical engineering, permeability indicates the difficulty of pore fluid going through the pores of the soil skeleton under certain hydraulic gradient. Hydraulic conductivity $k(m/s)$ consists of permeability $K(m^2)$ which is only related to geometry of the pores in the clay, the density $\rho(kg/m^3)$ and the dynamic viscosity $\mu(kg/(ms)\text{or}Pas)$ of water as expressed in Eq.(2.2). The viscosity of water μ is decreasing with increasing temperature (Table. 2.3) (Korson et al. 1969). Towhata, Kuntiwattanakul, Seko, et al. (1993) postulated that the rate of volume change is accelerated by heating because of the reduced dynamic viscosity of the water when heated, which means that the hydraulic conductivity changes in the process of heating.

$$k = K\frac{\rho g_0}{\mu(T)} \tag{2.2}$$

Table 2.3: Dynamic viscosity and density of water (Korson et al. 1969).

Temperature (^{o}C)	5	10	15	20	25
$\mu(\times 10^{-3}Pas)$	1.518	1.307	1.139	1.002	0.890
$\rho(kg/m^3)$	999.9	999.7	999.1	998.2	997.0

If the temperature can affect the organization soil particles, the intrinsic permeability K which depends solely on the property of the soil skeleton, is influenced. However, in the tests done by Delage, Sultan, et al. (2000) on Boom clay, the intrinsic permeability K was found to be insensitive to temperature changes, as shown in Fig. 2.7.

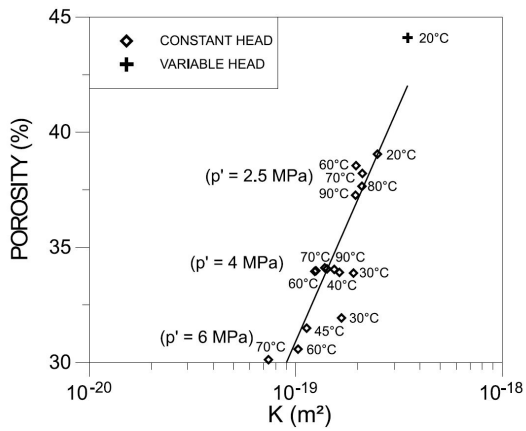

Figure 2.7: Results of permeability in terms of intrinsic permeability K (Delage, Sultan, et al. 2000).

Table 2.4: Engineering mechanical properties of soil under temperature change.

Thermal load	Mechanical load	Shear strength	Yield stress	M	κ	λ	References
D	U	↘	-	-	-	-	Sherif and Burrous 1969
-	Direct shear	↗	-	-	-	-	Noble and Demirel 1969
D	D and U	↗ for D, → for U	↘	→	↗	-	Houston et al. 1985
D	D and U	↘	↘	→	↗	-	Lingnau, Graham, and N. Tanaka 1995
D	D	↘ for OC, ↗ for NC	↘	→	-	-	Hueckel and Baldi 1990
D	U	↗	↘	-	↗	-	Kuntiwattanakul et al. 1995
D	U	↘	-	→	-	-	De Bruyn and Thimus 1996
D and U	U	↗	↘	-	-	↘	N. Tanaka et al. 1997
D and U	U	↘ for U,→ for D	↘	→	↘	→	Graham et al. 2001
D and U	-	-	↘	-	→	→	Sultan et al. 2002
D	D	↗	↘	→	↗	→	Cekerevac and Laloui 2004
D	D and U	↗	→	→	→	→	Abuel-Naga, Bergado, and Lim 2007
-	Direct shear	↗	-	→	-	-	Yavari et al. 2016

↗ Increase with increasing temperature
↘ Decrease with increasing temperature
→ Constant under different temperature
U Undrained; D Drained
OC Overconsolidated;NC Normally Consolidated

2.2.4 Time-dependent behaviour under temperature change

The long-term response of natural sensitive clays is governed by the consolidation, creep and relaxation of the material, as well as the unknown mechanisms that fall under soil aging. The magnitude of these time-dependent effects is influenced by the natural structure and the mineral composition of the clay. Clay structure refers to the combined effect of the fabric and the bonds between the clay particles or aggregates (Delage and Lefebvre 1984; Leroueil and Vaughan 1990) resulting from geological formation of the clays and the subsequent geo-chemical processes. This natural structure is complex, and easily influenced by environmental changes. Additionally, the sensitivity to temperature effects also depends on the mineral composition, for example active clays such as montomorillonite (Hansen et al. 2012) are temperature-sensitive.

Creep is the tendency of a solid material to move slowly or deform permanently under the influence of constant mechanical stresses. Generally creep in geomaterials is defined as the ongoing deformation under constant effective stress, and is the reorganization of soil particle arrangement that develops with time. Creep can occur as a result of long-term exposure to high levels of stress that are still below the apparent preconsolidation pressure of the material. This means that creep can happen at any stress state. There are only a limited number of tests reported that study the creep of clay under temperature changes, even fewer of them focused on soft clay. The limited tests indicate that creep accelerates under elevated temperatures both in the laboratory (Burghignoli et al. 1992; Burghignoli et al. 2000; Coccia and McCartney 2016a; Houston et al. 1985; Nguyen et al. 2017; Plum and Esrig 1969; Towhata, Kuntiwattanakul, Seko, et al. 1993), and in the field (Akrouch et al. 2014; Fox and Edil 1996). The latter results are plotted in Fig. 2.8, where the increasing temperature in stiff clay increased the creep exponent n by the factor of 4 to 5.

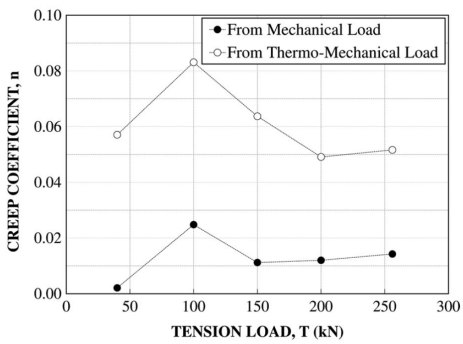

Figure 2.8: Creep exponent (n) versus tension load. (Akrouch et al. 2014).

As discussed earlier, thermal softening and strain hardening can lead the clay to a new equilibrium state with a new apparent preconsolidation pressure (Cui et al. 2000; Towhata, Kuntiwattanakul, Seko, et al. 1993). If a thermal steady state is reached, creep continues with a creep rate that is related to the distance between the current stress state and the

new yield surface (Hicher 2016). However, the interpretation that the increasing creep rates are solely induced by the reduction in apparent preconsolidation pressure upon heating (Leroueil and Soares Marques 1996; Moritz 1995) seems incomplete.

Stacks of clay minerals or particles that form the aggregates in clays are directionally arranged during sedimentation. Structural studies using Scanning Electron Microscopy show that the mineralogy of clay powder remains unchanged when heated to 200 °C (Towhata, Kuntiwattanakul, and Kobayashi 1993). According to the X-Ray study (Zhang et al. 1993), the interlayer spacing is independent of temperature, but the total water content is decreasing with increasing temperature under constant interlayer load. In contrast, in wet samples the orientation of particles and the spaces between and inside the aggregates can change. On the smallest scale (nanometres), it is demonstrated that even if the mineralogy stays the same upon temperature changes, the basal length of the distance between the clay platelets will change irrecoverably (Baldi et al. 1988; Brochard et al. 2017; Hansen et al. 2012), which can lead to a drop in repulsive force. The orientation of the clay platelets of reconstituted clays that are perpendicular to the mechanical loads also change slightly after heating and cooling cycles (Jaradat et al. 2017). In saturated clays, there is mass transfer between free water and absorbed water under heating and cooling (Ma and Hueckel 1993). Hence, the changes in the intrinsic structure and creep rate upon heating and cooling appear to originate from the exchange of free and bonded water within and between the stacks of clay platelets, or the change in the orientation of the stacks.

The temperature of the clay surrounding a geothermal structure is not constant, it changes periodically under the influence of the geothermal structure. Unlike the most type of the cyclic loads that originate from nature and human activities, for example earthquakes ($>$ 1 Hz), wind loads from wind-turbines and traffic loads (0.01 to 0.1 Hz), the thermal cycles caused by heat storage have relative low frequency (1×10^{-5} Hz if counted daily). Similarly to the mechanical loading cycles caused by traffic (Hyodo et al. 1992; Kimoto et al. 2013; Pasten, Shin, et al. 2013), thermal cycles may lead to irreversible deformation. Depending on the ambient environment and the energy demand of the geothermal structure, the heat extraction and storage is a daily, monthly or yearly process. The monthly average value of ambient temperature (solid line in Fig. 2.9) changes annually, the temperature in the shallow surface (red dashed line in Fig. 2.9) changes daily depending on the temperature of the specific day, and the temperature deep in the ground (blue dashed line in Fig. 2.9) varies only according to the demands of the geothermal structure. Therefore, the clay surrounding the geothermal structures is exposed to numerous thermal cycles during the life-time of the geothermal system (as plotted in the Fig. 2.9), even though the frequency of the thermal cycles is relatively low. As mentioned, an increase in temperature can lead to irreversible deformation in the clay which cannot be recovered by cooling (Baldi et al. 1988; Burghignoli et al. 1992; Demars and Charles 1982; Di Donna and Laloui 2015; Eslami et al. 2017), especially normally consolidated sensitive clays. In this way, irreversible strain accumulates after the thermal cycles, which is unfavourable for the long-term stability of the geothermal structure.

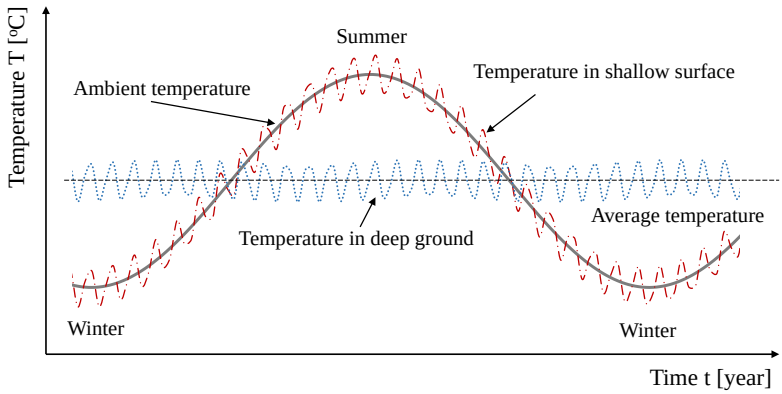

Figure 2.9: Temperature in the clay close to geothermal structures.

2.3 Numerical Modelling

2.3.1 THM multi-physics modelling

Multi-physics simulations is one of the most useful methods to utilise the temperature-dependent constitutive models in the application of geothermal structures. This is called thermo-hydro-mechanical (THM) modelling. Various simulations have been carried out to study the energy efficiency of geothermal system and the mechanical performance of the geothermal structures (Dupray et al. 2014; François, Laloui, and Laurent 2009; Gashti et al. 2014; Gens, Vaunat, et al. 2007; Jeong et al. 2014; Laloui, Nuth, et al. 2006; McCartney and Rosenberg 2011; Salciarini et al. 2017; Suryatriyastuti et al. 2014).

There are three physicsical processes that occur in the clays subjected to temperature changes: heat transfer, water flow and deformation, which requires energy balance, mass balance and equilibrium, respectively. For the simulations of the energy balance, thermal properties, such as the thermal conductivity and the heat capacity, need to be acquired.

When clay is considered as a continuous porous medium under heat transfer in the numerical simulations, the macro-level thermal properties such as thermal conductivity λ_T and specific heat capacity C_v of saturated soil depend on the fraction of soil particles and pore fluid (usually water), which change under temperature fluctuation.

Thermal conductivity λ_T is the rate at which heat passes through a specific material. It is expressed as the amount of heat ΔQ(J) that flows per unit time Δt(s) through a unit area A(m^2) with a temperature gradient of one degree per unit distance $\Delta T/L$ (°C/m),

expressed as Eq.(4.1).

$$\lambda_T = \frac{\Delta Q}{\Delta t} \cdot \frac{1}{A} \cdot \frac{L}{\Delta T} = \frac{q}{\Delta T / L} \tag{2.3}$$

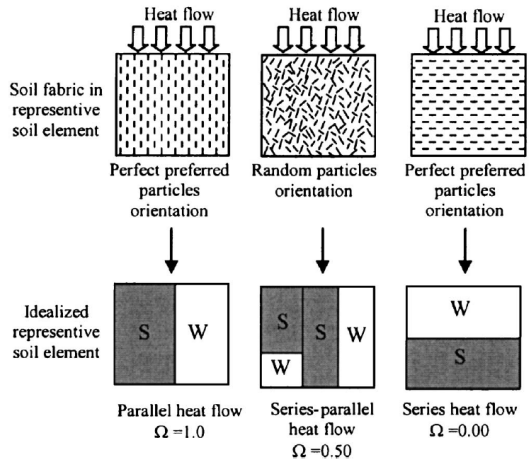

Figure 2.10: The physical interpretation of Ω and thermal anisotropy (Abuel-Naga, Bergado, and Bouazza 2008).

If considered as a continuous thermal medium, the thermal conductivity of soil is also related to other soil characteristics, such as mineralogical composition, dry density, porosity, the type of pore fluid, the degree of the saturation, water content, temperature and the geometrical arrangement of the soil particles ((Abuel-Naga, Bergado, and Bouazza 2008; Dao et al. 2014)). Thermal conductivity of typical soil particles varies from approximately 1.0 to 9.0 ($\mathrm{W{\cdot}m^{-1}K^{-1}}$), depending on mineralogy, whereas the values for water and air are 0.586 and 0.0257 ($\mathrm{W{\cdot}m^{-1}K^{-1}}$) at 20°C, respectively. Depending on the arrangement or orientation of the natural clay platelets or stacks compared to the heat flow in Fig. 2.10, the thermal conductivity can be calculated using the following equation (Abuel-Naga, Bergado, and Bouazza 2008),

$$\lambda_T = \frac{1-\Omega}{\frac{1-n}{\lambda_{Ts}} + \frac{n}{\lambda_{Tf}}} + \Omega[(1-n)\lambda_{Ts} + n\lambda_{Tf}] \tag{2.4}$$

where Ω is the parameter to describe relation between the orientation of the particles and the direction of the heat flow, as can be seen in Fig. 2.10, n is the porosity, λ_{Tf} and λ_{Ts} are the thermal conductivities for pore fluid and soil particles, respectively. Because of the disturbance caused by the construction of the geothermal structure, for example the installation of the geothermal piles, the arrangement of the soil particles around pile will most likely be different from undisturbed nature clay. In such a case, the anisotropy of the thermal conductivity should also be considered when using an anisotropic soil model.

Specific heat capacity C_p is defined as the number of heat units ΔQ (J) needed to raise the temperature of a body m (kg) by one degree ΔT (°C),

$$C_p = \frac{\Delta Q}{m \cdot \Delta T} = \frac{C_v}{\rho} \tag{2.5}$$

where C_p is the specific heat capacity per unit mass, and C_v is the specific heat capacity per unit volume. Similarly to the thermal conductivity, the heat capacity also depends both on the type of soil particles and the pore fluid, as well as the fraction between them. The volumetric thermal capacity C_v for a soil can be calculated by adding the heat capacities of various components, as expressed by Eq.(2.6), where V_s, V_w, V_a stands for the volume of solid, water and air, respectively. $C_{v;s}$, $C_{v;w}$, $C_{v;a}$ represents volumetric heat capacity of solid, water and air, respectively.

$$C_v = \frac{V_s C_{v;s} + V_w C_{v;w} + V_a C_{v;a}}{V_s + V_w + V_a} \tag{2.6}$$

For saturated soil, the thermal capacity and the thermal conductivity can be very different because of the differences in void ratio (Eq.(2.4) and Eq.(2.6)). This is most important for sensitive clay due to the large changes in void ratio. Typical thermal properties for water, soil particles and clay at 20°C are listed in Table. 2.5 (Tarnawski and Wagner 1991). temperature-dependent constitutive models can be verified by comparing

Table 2.5: Thermal properties for soil at 20°C (Tarnawski and Wagner 1991).

Properties	Density ρ	Conductivity λ_T	Capacity C_p
Unit	kg/m^3	$W/(m \cdot K)$	$J/(kg \cdot K)$
Mineral Particles	2350 to 2970	3	1.8-3$\times 10^3$
Water	1000	0.57	4.182$\times 10^3$
Clay	1600	1.2	2.1-3.5 $\times 10^3$

the numerical simulations with laboratory results (Hong et al. 2013; Laloui and Cekerevac 2008b; Modaressi and Laloui 1997; Savvidou and Britto 1995). Numerical simulations can also help to evaluate the capability of the constitutive model and the efficiency of the whole geo-thermal energy system at boundary value level. However, the numerical simulation that have been carried out until now focus more on the pile or energy performance of geothermal structures, for example boreholes (François, Laloui, and Laurent 2009), piles (Gashti et al. 2014; Gens, Vaunat, et al. 2007; Jeong et al. 2014; Pasten and Santamarina 2014; Vieira and Maranha 2016) or pile groups (Di Donna, Loria, et al. 2016; Jeong et al. 2014). Different finite element software are used for the multi-physics simulations, for example COMSOL (Gashti et al. 2014; Jeong et al. 2014), FLAC^{3D} (Suryatriyastuti et al. 2014) and Lagamine (Dupray et al. 2014). In all multi-physics modelling, the macroscopic equilibrium need to be satisfied. In a THM model, three equilibrium equations need to be satisfied: for water flow (Eq. 2.7), heat flow (Eq. 2.9) and stress field (Eq. 2.11). The

mass conservation equation for a saturated material can be written as:

$$\frac{\partial(\varepsilon_v \rho_w)}{\partial t} + \nabla(\rho_w \mathbf{u}) = 0 \tag{2.7}$$

where ε_v is the volumetric strain which includes the deformation of the soil skeleton and thermal expansion of water, ρ_w is the density of the fluid (water), t is time, ∇ is vector operator, $\nabla = \left(\frac{\partial}{\partial x}, \frac{\partial}{\partial y}, \frac{\partial}{\partial z}\right)$, and $\mathbf{u}$ is the water flow which can be written as:

$$\mathbf{u} = -\frac{K}{\mu}\nabla u \tag{2.8}$$

where K is the intrinsic permeability, μ is the dynamic viscosity of water and u is the water pressure. The equilibrium equation for heat storage and transfer can be written as:

$$\rho C_p \frac{\partial T}{\partial t} + \rho_w C_{p;w} \mathbf{u} \cdot \nabla T + \nabla \cdot \mathbf{q} = 0 \tag{2.9}$$

where C_p is the specific heat capacity of the clay, which can be obtained using Eq. 2.6, ρ is the density of the saturated clay, T is the temperature, $\mathbf{u}$ is the water flow in the clay (Eq. 2.8), and $\mathbf{q}$ is the heat flow (conduction) in the clay, which is written as:

$$\mathbf{q} = \lambda_T \nabla T \tag{2.10}$$

where λ_T is the thermal conductivity which can be calculated via Eq. 2.4. In the end, the mechanical balance Eq. 2.11 can be written as:

$$\nabla \cdot \boldsymbol{\sigma} + \mathbf{f}_v = 0 \tag{2.11}$$

where $\mathbf{f}_v$ is the body force per unit mass, $\boldsymbol{\sigma}$ represents the stresses, which include excess pore pressures. Thus, heat convection and conduction and storage is connected to the water flow and excess pore pressures. The pore pressures caused by the temperature change are accounted in the stress field in the clay.

2.3.2 Temperature-dependent constitutive models

The abundance of thermally-controlled laboratory and field tests performed have led to temperature-dependent constitutive models, e.g. (Abuel-Naga, Bergado, Bouazza, and Ramana 2007; Coccia and McCartney 2016b; Collins and Kelly 2002; Cui et al. 2000; Hueckel and Baldi 1990; Laloui and Cekerevac 2008a; Zhou and Ng 2015; Zymnis et al. 2018). Most of these tests and the resulting constitutive models focus on rate-independent stress-strain response of clays, often for large temperature amplitudes that are representative of nuclear waste barriers. A constitutive model for soil is needed for predicting the behaviour of clays under complex boundary conditions (including water, temperature and mechanical boundaries). Therefore, the temperature-dependent constitutive models for clays are proposed to describe the development of (elastic, plastic,

viscoplastic) strains under the change of temperature, by modifying the temperature-invariant elasto-plastic or viscoplastic models (Hong et al. 2013). To take into account the effect of temperature based on the temperature-invariant constitutive model, a new variable T is included in the formulation by making the mechanical properties or state variables temperature-dependent.

Similarly to the traditional constitutive models, the total strain in temperature-dependent constitutive models is composed of two parts: the elastic part which is reversible during unloading (mechanical loading and thermal loading), and a plastic part which is irreversible. Both elastic and plastic strains can be divided by the strain caused by either the thermal loads or mechanical loads as expressed with Eq.(2.12),

$$\dot{\varepsilon}^t_{ij} = \dot{\varepsilon}^e_{ij} + \dot{\varepsilon}^{ir}_{ij} = \dot{\varepsilon}^e_{Mij} + \dot{\varepsilon}^{ir}_{Mij} + \dot{\varepsilon}^e_{Tij} + \dot{\varepsilon}^{ir}_{Tij} \tag{2.12}$$

where $\dot{\varepsilon}_{ij}$ represent strain increment. Subscriptis T and M denote changes in temperature and mechanical load, respectively. Subscripts i and $j = 1, 2, 3$ are strain components in different directions. Superscripts e and ir stands for elastic and irreversible, respectively.

Thermally induced stresses (excess and negative pore pressures) and external stresses can together be called as thermo-mechanical loads. It is difficult to eliminate the change of pore pressure in clays upon temperature fluctuations, because of the low hydraulic conductivity. The expansion and the reorganization of soil structure caused solely by thermal loads can be classified as temperature-induced strain. These two components (thermal and mechanical strains), however, are difficult to separate.

Reversible strains are recoverable after withdrawing the applied mechanical or thermal loads. The expansion or contraction of soil particles under drained condition are assumed to be reversible as expressed in Eq.(2.13),

$$\dot{\varepsilon}^e_{Tij} = \alpha_T \dot{T} \tag{2.13}$$

where α is the thermal expansion coefficient of the clay that depends on the mineralogy and the dot represents an increment of the variable. If effective stress level is changed due to thermal loading, Eq.(2.14) need to be used to calculate the mechanical strain increment, where s_{ij} is the deviatoric stress and I_1 is the first stress invariant in principal stress space. G and K_B are the shear and bulk moduli, respectively.

$$\dot{\varepsilon}^e_{Mij} = \frac{\dot{s}_{ij}}{2G} + \frac{\dot{I}_1}{9K_B}\delta_{ij} \tag{2.14}$$

Most of temperature-dependent models for clays are developed based on elasto-plastic models by modifying the yield surfaces and the hardening law. There are less proposal for rate-dependent models than for rate-independent models. Therefore, we mainly discuss temperature-dependent elasto-plastic constitutive models here.

Yield surface In elasto-plastic models, irreversible strain develops when stress level

exceeds a threshold value, and the threshold values altogether are represented by a yield surface (called reference surface or Normal Compression surface in viscoplastic models) .

Irreversible strains contribute to the hardening, i.e., the expansion or movement of the yield surface (or reference surface in viscoplastic models). In temperature-dependent model, the shape and size of the yield surface depends on the mechanical load, the strain history and the temperature condition as written in Eq.(2.15).

$$f = f(p', q, \varepsilon^{ir}, T) = 0 \tag{2.15}$$

where p' is the mean effective stress, q is the deviator stress and ε represents the strain history and T is temperature. In the elasto-plastic model, to satisfy the consistency condition, $\dot{f} = 0$, Eq.(2.16) can be obtained.

$$\dot{f} = \frac{\partial f}{\partial \varepsilon^{ir}}\dot{\varepsilon}^{ir} + \frac{\partial f}{\partial T}\dot{T} + \frac{\partial f}{\partial p'}\dot{p'} + \frac{\partial f}{\partial q}\dot{q} = 0 \tag{2.16}$$

If no excess or negative pore pressures are generated under thermal loading, effective stress state remains constant, $\dot{q} = 0, \dot{p'} = 0$, and the equation yields

$$\frac{\partial f}{\partial \varepsilon^{ir}}\dot{\varepsilon}^{ir} + \frac{\partial f}{\partial T}\dot{T} = 0 \tag{2.17}$$

The flow rule prescribes the magnitude and direction of the irreversible strain increment as expressed in Eq.(2.18).

$$\dot{\varepsilon}^{ir}_{TMij} = \dot{\lambda}\frac{\partial g}{\partial \sigma'_{ij}} \tag{2.18}$$

where g is the potential surface. The plastic potential g can be defined separately (Robinet et al. 1996), or for simplicity it can be the same as the yield surface f. In most temperature-dependent models, an associated flow rule has been adopted ($g = f$).

The hardening law, which is describes the change in the size of the yield surface due to the irreversible strains, differs according to how researchers describe the evolution of the yield surface upon the development of strain. In most temperature-dependent constitutive models, the apparent preconsolidation pressure is modified from only irreversible strain-dependent to be irreversible strain- and temperature-dependent $p'_c = p'_c(\varepsilon^{ir}_v, T)$ (Hueckel and Pellegrini 1991). The increment of the preconsolidation pressure thus be written as Eq. 2.19.

$$\dot{p'_c} = \dot{p'_c}(\varepsilon^{ir}_v, T) = \frac{\partial p'_c}{\partial \varepsilon^{ir}_v}\dot{\varepsilon}^{ir}_v + \frac{\partial p'_c}{\partial T}\dot{T} \tag{2.19}$$

Some of the examples for the yield surfaces and the hardening laws of thermo-plastic models are listed in Table. 2.6. For definition of the various parameters, please refer to the original publication.

Table 2.6: Yield surfaces and hardening laws for temperature-dependent constitutive models for clays.

Hardening law	Yield surface	References
$p'_c = \quad 2(a\exp\frac{1}{\lambda-K_T}[e_1+(1+e_0)\varepsilon_v^{tp}]$ $+a_1\Delta T+a_2 sign(\Delta T)\Delta T^2)$	$f=(\frac{2p'}{p'_c(\varepsilon_v^{pt},\Delta T)})^2+\frac{4q^2}{[Mp'_c(\varepsilon_v^{tp},\Delta T)]^2}-1=0$	Hueckel and Pellegrini 1991
$p'_{cT}=p'_{c0}\exp(\beta_m\varepsilon^p_{mv})\exp(\beta_T\varepsilon^{ir}_{Tv})$	$f=q^2-M^2\gamma^2p'(bp'_c(T)-p')R^2(\Theta)$	Robinet et al. 1996
	$f=q-p'Fr\sin\varphi$	Modaressi and Laloui 1997
$p'_c=\frac{2p'_{c0}}{1+\beta}\exp\{\frac{1+e_0}{\lambda-\kappa_T}\varepsilon_v^{p1}(1-\alpha_0\Delta T)\}+A(\Delta T)$	$f=\left(\frac{p'}{p'_c(T)/2}-1\right)^2+\left(\frac{q}{Mp'_c{}^*(T)/2}\right)^2-1=0$	Hueckel, Pellegrini, and Del Olmo 1998
$\frac{dp'_{c0}}{p'_{c0}}=\frac{\alpha_0}{\alpha_p[\exp(\alpha_p\Delta T)-a]}d\varepsilon^p_{vpT}+\frac{v}{\lambda-\kappa}[d\varepsilon^p_{vp}$ $+d\varepsilon^p_{vpT}]+\{\frac{\alpha_0}{\alpha_p[\exp(\alpha_p\Delta T)-a]}+k\left[\frac{v}{\lambda-\kappa}\right]\}d\varepsilon^p_{vT}$	$f=q^2+p'(p'-p'_{cT})$	Cui et al. 2000; Graham et al. 2001
$p'_T=p'_{T0}\exp(\beta\varepsilon^p_v)\{1-\gamma\log[T/T_0]\}$	$f=p'-\sigma'_c(T_0)\exp\{\beta\varepsilon^p_v\}\{1-\gamma\log[T/T_0]\}$	Laloui and Cekerevac 2003; Laloui and Cekerevac 2008a
	$f^{LY}=p'-p_c$ and $f^{TY}=p'-p_T$	Abuel-Naga, Bergado, Bouazza, and Ramana 2007
$p'_T=p'_{T0}\exp(\beta\varepsilon^p_v)\left(\frac{\dot\varepsilon^{vp}_v}{\dot\varepsilon^{vp}_{v0}}\right)^{C_A}\{1-\gamma\log\frac{T}{T_0}\}$	$f=p'-\sigma'_c(T_0)\exp\{\beta\varepsilon^p_v\}\left(\frac{\dot\varepsilon^{vp}_v}{\dot\varepsilon^{vp}_{v0}}\right)^{C_A}\{1-\gamma\log[T/T_0]\}$	Laloui, Leroueil, et al. 2008
$\alpha=\alpha_c(T)\alpha_m\left[1.0-c_1\exp\left(-\frac{\varepsilon^p_s}{c_2}\right)\right]$ $p'_T=p'_{T0}\exp(\beta\varepsilon^p_v)\{1-\gamma\log[T/T_0]\}$	$f=\frac{\sigma'_m}{1-(\eta/\alpha(T))^n}-\sigma'_c(T)$	Liu and Xing 2009

$M = M_0 - g(T - T_0)$	$f_{iso} = p' - p'_c r_{iso}$ $f_{dev} = q - Mp\left(1 - b\frac{p'd}{p'_c}\right) r_{dev}$	Laloui and François 2009
$dp'_c = p'_c\left(\frac{\upsilon}{\lambda-\kappa} d\varepsilon_v^p\right)$ $\alpha(T) = \alpha(T_0) + c\left(\frac{T}{T_0} - 1\right)$	$f = \frac{M^2+(\eta-\alpha(T))^2}{M^2+\alpha(T)^2} p - p_c$	Abuel-Naga, Bergado, Bouazza, and Pender 2009
$dp'_{cT} = p'_{cT} \frac{\upsilon d\varepsilon_v^p}{\lambda-\kappa_T-\left[n\Delta e_T\left(\frac{M_T}{M_T-\eta}\right)\right]}$	$f = q - M_T p' \{\frac{\alpha^2(\beta-1)}{2\theta-1}\left[\left(\frac{p'_{cT}}{p'}\right)^{1/\Omega} - 1\right]\}^{0.5}$	Hamidi et al. 2014
$dp' = p'\left(\frac{\upsilon}{\lambda-\kappa} d\varepsilon_v^p - \beta dT\right)$ $r = \exp\left[\frac{(N_0-\Gamma_0)-(r_N-r_\Gamma)(T-T_0)}{\lambda-\kappa}\right]$	$f = \left(\frac{q}{Mp'}\right)^n + \frac{\ln[p'/p_0(T)]}{\ln r(T)}$	Zhou and Ng 2015
$p'_T = p'_{c0} \exp\left(\frac{\varepsilon_v^p}{(\lambda-\kappa)/\upsilon}\right) \theta \ln\left(\frac{T}{T_0}\right)$	$f = p' \cdot \frac{(M^2-\alpha^2)+(q/p'-\alpha)^2}{M^2-\alpha^2} - p'_T$	Wang et al. 2016

The symbols in the table are taken from the original papers and may conflict with the notations in this thesis.
For the definition of the symbols in this table, please refer to the original articles.

2.4 Proposed research

Because of the contradictory findings on the thermal dependency of soil parameters, systematic laboratory tests are needed to fully understand the thermo-mechanical response of soft sensitive clay. Based on the thermal properties of the soil and the basic understanding on the thermal response of soil, temperature-controlled laboratory test need to be designed and carried out. The response of the tested soil needs to be observed during both thermal and mechanical loading processes to obtain the temperature-dependent mechanical properties. To assess the long-term stability during the lifetime for the geothermal structures and sustainable utilization, in particular more laboratory tests on the creep behaviour of clays under static and cyclic thermal loading are needed. For sensitive soft clays in Canada and Scandinavia, the long-term behavior is important, especially for shallow geothermal systems.

In Sweden, most clays are either normally consolidated or slightly overconsolidated. The problems with creep are expected to be largest for these types of clays. In applications involving heat extraction and injection or storage in Nordic countries, the operating temperatures usually range from 0 to 30 °C. A systematic experimental evaluation of the long-term response of natural sensitive clays under slowly varying temperature in this range is needed. Furthermore, the impact of the initial structure of the clay on the material response needs to be quantified, as this potentially is affected the most. Thus, temperature-controlled laboratory tests also need to be carried out on reconstituted clays as a reference. In order to understand the results, the testing needs to be fully integrated with THM modelling, coupling heat, water flow and soil deformation.

3 Experimental and numerical methodology

This Chapter introduces a test setup to study the effects of combined thermal and mechanical loading history on the behaviour of natural sensitive clays in one-dimensional compression. After the introduction of design, realisation and calibration of the test setup, numerical methods for detailed analyses of the results will be discussed. Furthermore, the material tested will be extensively characterised for its mechanical and thermal properties.

3.1 Temperature-controlled oedometer test setup

Series of temperature-controlled oedometer tests are performed, in order to study the rate-dependency in natural clays under varying temperatures. This enables cost-effective testing for a large number of mechanical and thermal loading scenarios. Two types of thermal loading is investigated. For the first series, the rate-dependency (creep) is studied without generating excess pore pressures (slow cooling and heating). The second series (fast cooling and heating), on the other hand, studies the combined effect of generation and dissipation of excess pore pressures (thermal consolidation) and creep effects. For the slow thermal tests, the ambient temperature of the climate room is used to control the temperature. In the fast tests an additional water bath, water circulation system and regulated heat source are used. All the tests were conducted at the climatised geotechnical laboratory facilities of Chalmers University of Technology.

A sketch of the oedometer setup is presented in Fig. 3.1. The temperatures are measured locally by watertight thermo-couples from Roth+Co inserted in the water bath surrounding the oedometer rings (indicated as 'Water' in Fig. 3.1). These industrial sensors have a measurement accuracy of ± 0.3 °C. Five target temperatures were selected: 5 °C, 10 °C, 15 °C, 20 °C and 25 °C. There are minor differences between the target temperatures and the measured temperature in the oedometer cell due to a temperature gradient in the climate room.

A displacement transducer (Novotechnik Position Transducer TR-0010), a linear potentiometer with a full range of 10 mm, is placed on top of the filter stones for each sample. After calibration, the sensors have a repeatability of ± 0.002 mm, resulting in the corresponding accuracy in void ratio of 0.0003, anticipating the initial height of the sample as 18 mm and an initial void ratio of 2.

For oedometer tests with a closed bottom boundary, water pressures are measured with pressure sensors. NeMESYS pressure sensors with an acquisition precision of ± 0.5 kPa are used for the pore pressure measurements due to the ease of de-airing, their stability and the fast measurement response.

The data acquisition of the displacement and pore pressure transducers is performed using

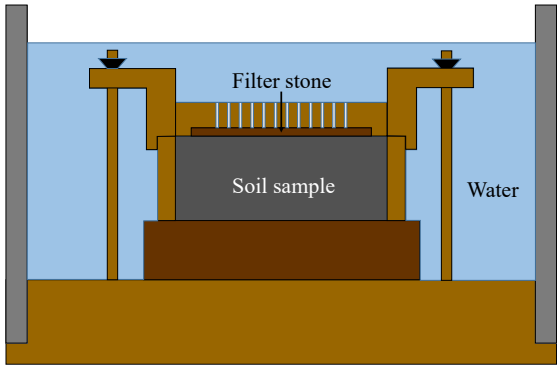

Figure 3.1: Boundary conditions in an oedometer test.

a MATEST 8 channels Cyber-Plus Evolution data logger. This system has a theoretical resolution of 24 bits, in practice 22 bits. The latter proves not to be a limitation to the acquisition of the test data reported here.

Two main methods are considered for heating the sample. In the first method, several cells are heated simultaneously by controlling the temperature of the climate room. In the second method, the samples are heated using an extra heater with PID (Proportional–Integral–Derivative) controlled water circulation system. The range in temperature change for these two methods is investigated in Fig. 3.2. The R in both Figures represents the heating rate (°C/hour). The heating and cooling rate achieved for the room temperature control is much smaller than the water circulation system. With the help of an additional heating source, the heating rate can reach 84 °C/hour.

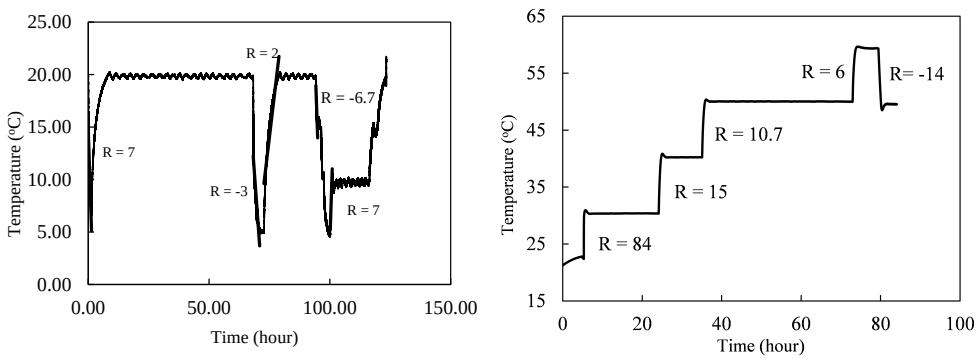

(a) Controlling temperature with the climate room. (b) Controlling temperature with water circulation system.

Figure 3.2: Temperature change with the different methods.

Depending on the heating or cooling rate, and the hydraulic conductivity of the clay, the

magnitude of the excess pore pressures generated during temperature change vary, see Fig. 3.3 for trial oedometer tests, in which the water pressures are measured on the closed bottom boundary. The effective stress changes due to these excess pore pressures reach up to 20% of the initial vertical effective stress for the highest heating rate. Similar behaviour is observed during cooling (Fig. 3.3(b)). As a result, both the stress and the strain history is affected by temperature. For the current study on the effect of temperature on creep in sensitive clays, with low hydraulic conductivity (10^{-9} to 10^{-10} m/s), the rate should be sufficiently low to prevent the generation of excess pore pressures, as shown in Fig. 3.4 with constant hydraulic conductivity of 5×10^{-10} m/s. The simulations done with COMSOL Multi-physics assume the clay to be elastic, Young's modulus $E = 500kPa$, Poisson's ratio $\nu = 0.25$. The magnitude of the pore pressures generated differ when heating the clay sample for one hour with different heating rates ranging from 1 °C/hour to 10 °C/hour as in Fig. 3.4.

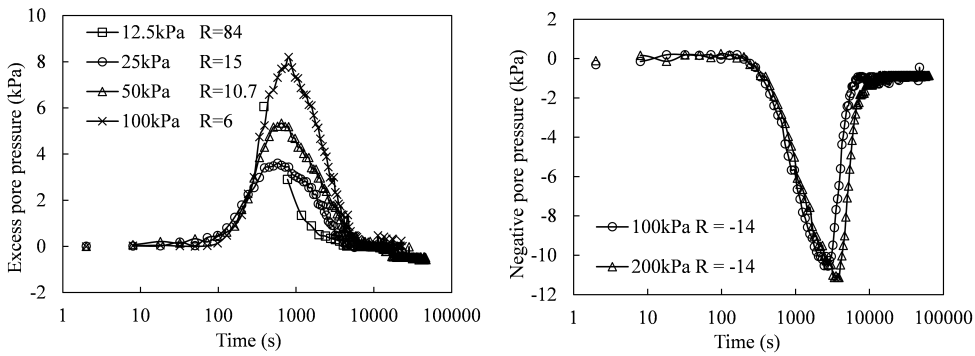

(a) Fast heating (b) Fast cooling

Figure 3.3: Pore pressures during fast heating and cooling.

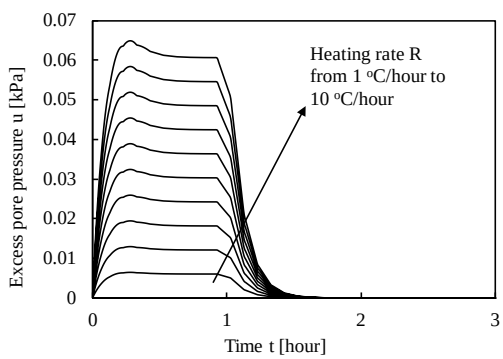

Figure 3.4: Simulated pore pressures generated under different heating rates.

The difference in the temperature response, the magnitude and the phase between the

ambient temperature of the air controlled by the room and the sample should be minimised. The entire oedometer test set-up is simulated with COMSOL using a coupled analysis as shown in Fig. 3.5(a) to study the potential delay, and the temperature gradient in the sample. The change in the ambient temperature is applied on the outside plastic wall of the water bath of the oedometer cell. The analyses show that with a heating rate of 6 °C/hour, the temperature difference between the plastic wall, water bath, brass ring and the sample is acceptably small as plotted in Fig. 3.5(b).

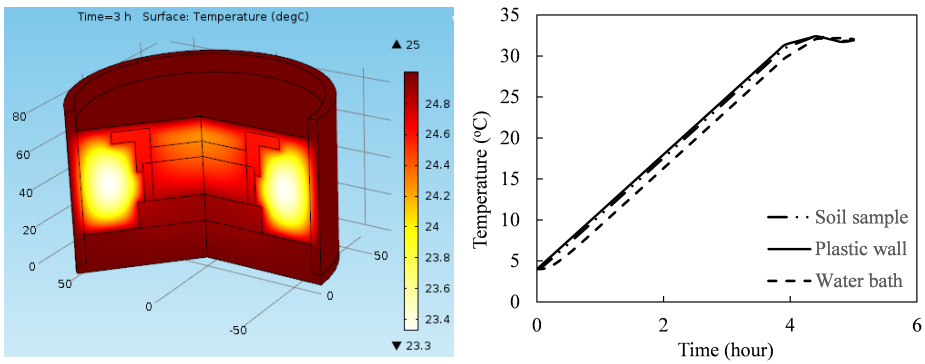

(a) Simulation in COMCOL

(b) Temperature in test setup

Figure 3.5: Temperature gradient within the oedometer test setup for slow heating.

3.1.1 Slow thermal loading system

For slow thermal loading, the temperature conditions for a large number of test specimens should be maintained in such a state that no excess pore pressures are generated. Consequently, to prevent thermal consolidation, the heating and cooling rates should be sufficiently low, so that the generation of excess pore pressures as shown in Fig. 3.3 can be avoided. As a result, controlling the room temperature is the most attractive method. All the 15 oedometer test cells are placed in the climate room as illustrated in Fig. 3.6. Cells 1, 2 and 3 are equipped with a water circulation system for fast application of thermal cycles in the second test series. Cells 4 to 15 are used for oedometer tests with slow heating and cooling ramps, of these Cells 5, 8, 11 and 14 are equipped with temperature transducers in the water bath.

Temperature

The whole loading system (sensors, loading frame, pistons, filter stones) will respond to temperature. These temperature effects are compensated for in the subsequent analyses using additional temperature measurements obtained for Cells 5, 8, 11 and 14 in the climate room (Fig. 3.6). The change of temperature in the water bath of the oedometer

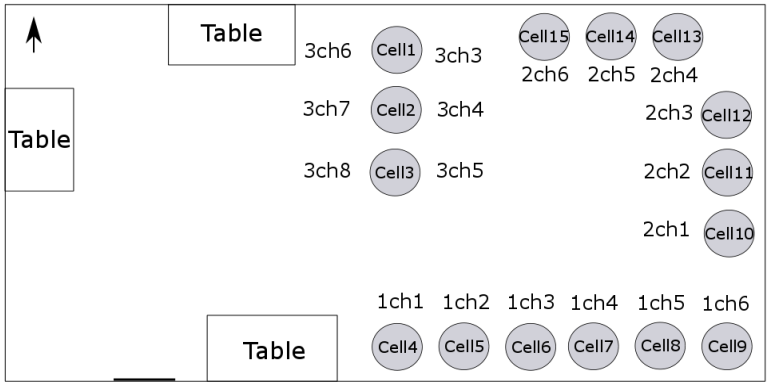

Figure 3.6: Oedometer test layout.

tests for initial slow cooling and heating tests is plotted in Fig. 3.7. The results indicate that the temperature is controlled within 0.3 °C, which falls within the precision of the temperature sensors, with a 2 hour period that corresponds to the temperature regulation system of the room, as shown in Fig. 3.7. A steady state temperature is reached after a period of 2 to 3 hours. After this period, the temperature is stable, with less than 0.5°C change over a 2 hours period (within the accuracy of the transducer), the remaining differences between the test cells correspond to a temperature gradient in the climate room itself.

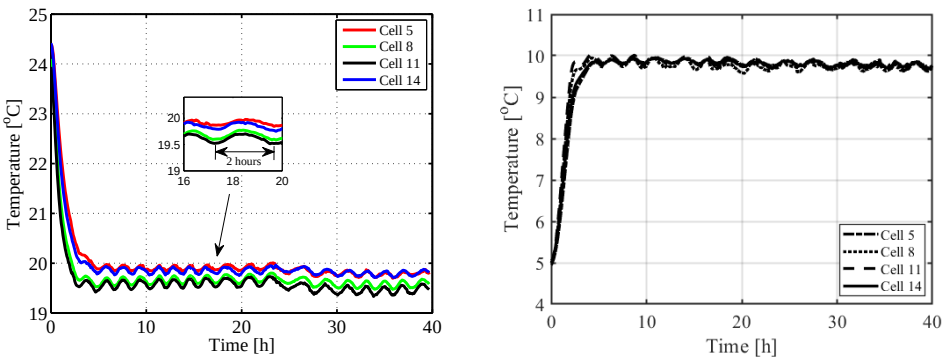

(a) Temperature in cooling

(b) Temperature in heating

Figure 3.7: Temperature evolution during cooling and heating.

3.1.2 Fast thermal loading system

Fast thermal cycles are required in order to study the creep behaviour of soft clay under cyclic thermal loading with varying loading periods. The latter also allows to further study the thermal consolidation process, and its effect on the rate-dependency. In the fast heating/cooling tests, an external heating source is used to heat up the water in the water tank as shown in Fig. 3.8. The oedometer cells for fast heating are Cell 1, 2 and 3 in Fig. 3.6.

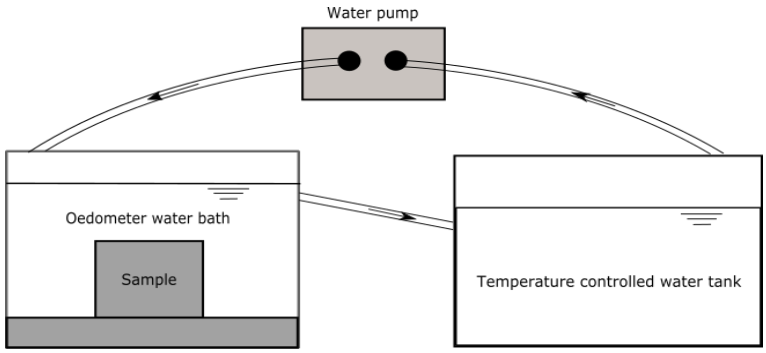

(a) Sketch of the fast heating system.

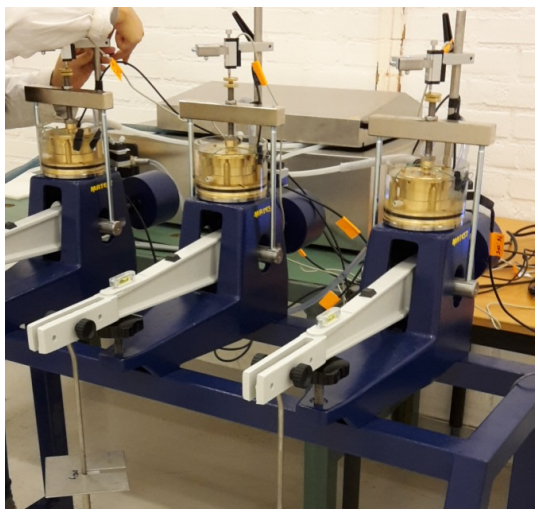

(b) Fast heating system with water circulation system.

Figure 3.8: Fast thermal loading system.

Cells 1, 2 & 3 were instrumented to measure the axial displacements and the pore pressures generated during heating and cooling. The bottom boundary is closed for drainage, as shown in Figs. 3.9(a) and 3.9(b) to facilitate the measurement of pore pressures with

an externally placed sensor(Fig. 3.9(c)). The temperature regulation in the water tank is realised using a simple heating element and a separate thermocouple. The element is switched on and off using a TTL signal from the data acquisition board (National Instruments USB-6001). The control software implements a PID loop implemented in Labview, i.e. when the measured temperature in the water bath is higher than the set point, the power of the heater is switched off, and vice versa. Fig. 3.10 shows the Labview implementation.

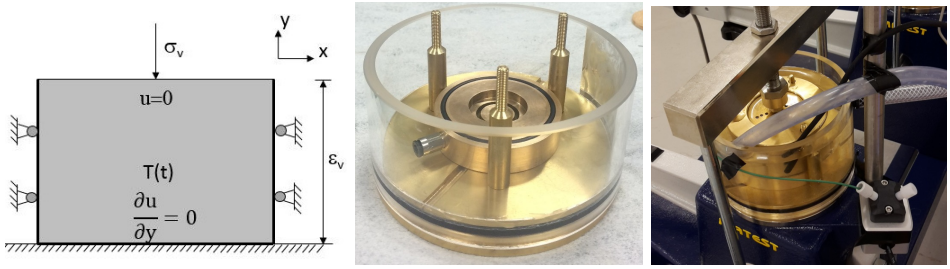

(a) (b) (c)

Figure 3.9: Fast thermal loading system with pore pressure measurements.

3.1.3 Calibration and verification

Even after careful selection of the materials and parts, all the mechanical components in the oedometer system, including loading frames, displacement sensors, pistons and filter stones, will deform upon temperature change. These thermal strains may affect the measurements and possibly create an additional load on the sample. The diameter of the brass oedometer ring will change with temperature. Equation 3.1, which is valid for constant volume deformations, is used to assess the effects of the temperature change in the ring on the change in measured axial displacements. The initial diameter D_0 of the brass ring confining the sample will change to the new diameter D', i.e. D_0 increases upon heating and D_0 decreases when cooled. Subsequently, the initial height of the sample h_0 will change to the new height h' after the temperature change.

$$\frac{h'}{h_0} = \left(\frac{D_0}{D'}\right)^2 \tag{3.1}$$

The system is more complex than just the oedometer ring, hence the complete test system is calibrated by conducting a dummy thermal oedometer test without samples. The brass rings are chosen as a trade-off between their thermal stability, low thermal expansion coefficient, reasonably low wall friction, corrosion resistance and costs. The sensitivity

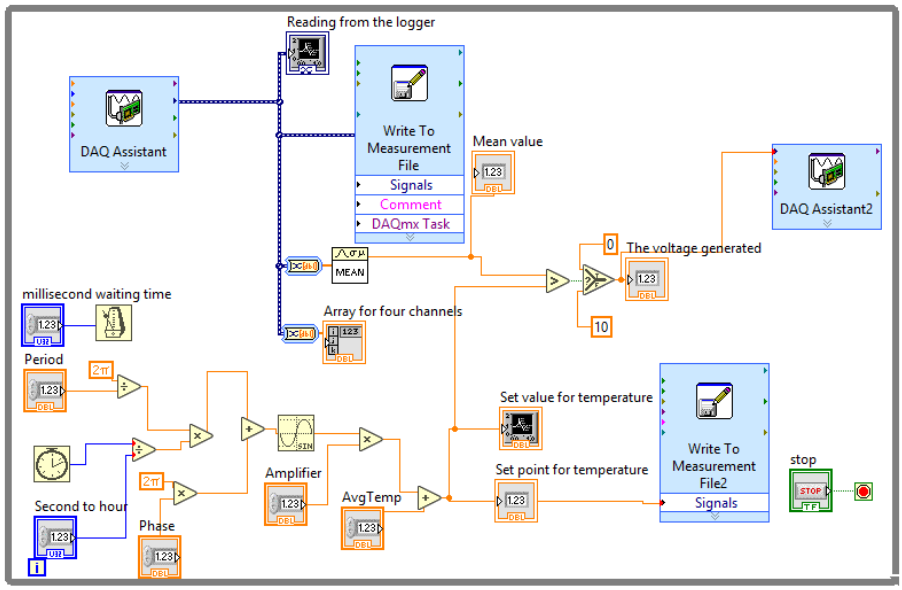

(a) Labview block diagram

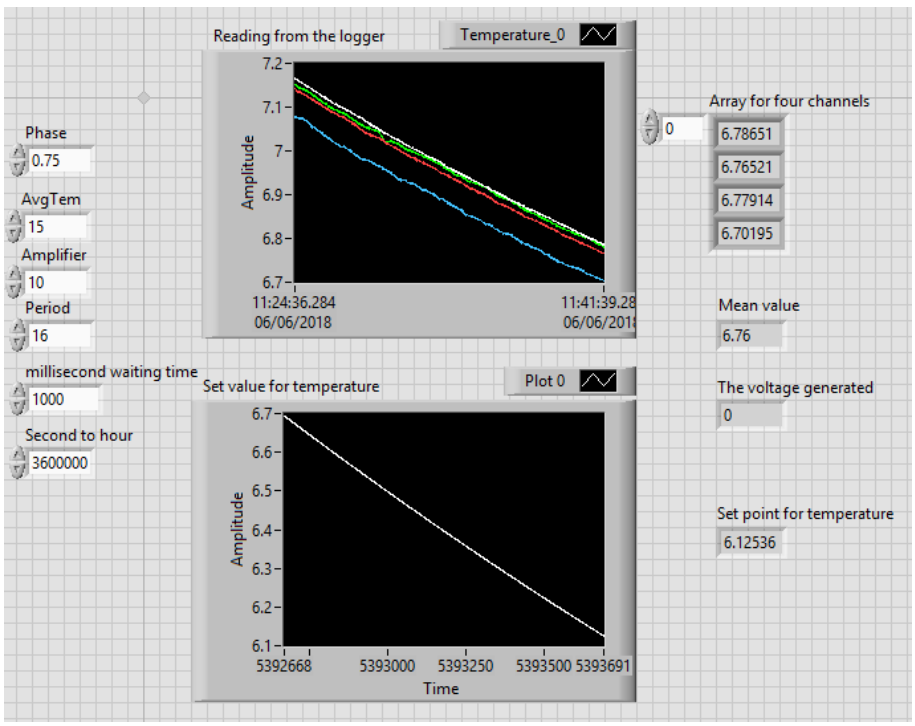

(b) Labview front panel

Figure 3.10: Temperature regulation controlled by Labview.

of the oedometer cells for temperature change is calibrated by measuring the combined effect using the measured vertical displacement as a proxy. This proved a more attainable method than measuring the change in size of the brass ring, which in the current design is constrained by other components of the oedometer cell. Furthermore, the temperature sensitivity of the sensor itself is directly incorporated in the calibration.

To account for the cell to cell variation seen in Fig. 3.11, all the cells are calibrated individually, as shown in Fig. 3.12 for the selected cells. The measured displacement after the stabilisation of the room temperature (around 4 hours) is shown in Fig. 3.11. The average displacement of the oedometer test system, as monitored by the vertical displacement transducer equates to ± 0.0008 mm/°C in a range of 5 °C. This increases to ± 0.016 mm for the full temperature range of interest (20 °C). These readings arguably are close to the linearity of the displacement transducer of ± 0.0075 mm. For an initial height of the test samples of 18 mm the change in void ratio caused by the thermal expansion of all elements in the system and the temperature-dependence of the sensor falls below 0.0007 and 0.003 for a temperature change of 5 °C and 20 °C (full range), respectively. This is rather insignificant (less than 5% for the extreme case) compared to the measured change in void ratio caused by the thermal and mechanical loading of intact samples. More calibration results are given in Appendix A. The calibration data is subsequently used to correct the measurements for the final test programme on the clay samples.

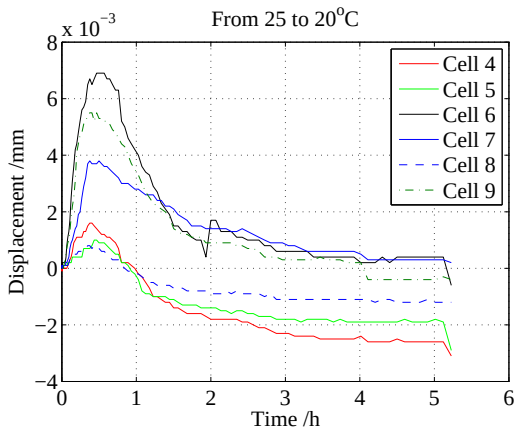

Figure 3.11: Displacement of the test cells.

Given the monitoring of the temperature-dependent creep is the main objective, pore pressures generated from thermal consolidation also can lead to additional undesired displacements in the clay samples during cooling and heating. These are additional effects to the measurement error discussed above. Therefore, a series of trial tests have been performed. The results of these trial tests are plotted in Fig. 3.13 for the excess pore pressures during a temperature decrement of 5°C, whereas Fig. 3.14 shows the excess pore pressure increment during a conventional mechanical loading increment prior to the the temperature decrement. The temperature decrement (25°C to 20°C), for which the

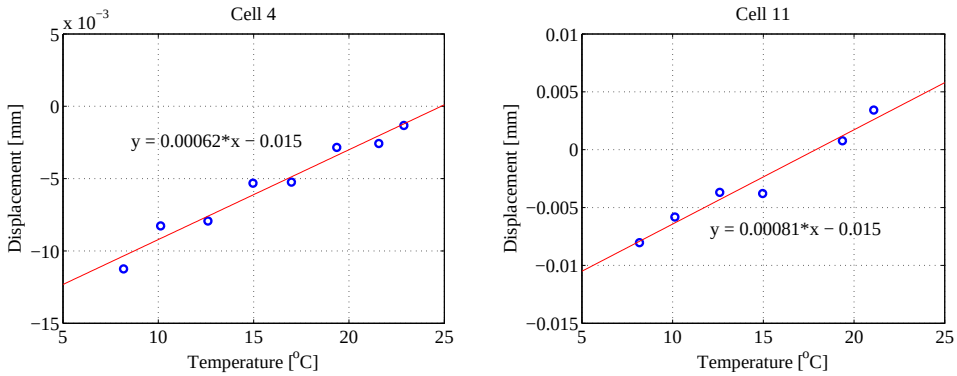

(a) Cell 4 (b) Cell 11

Figure 3.12: Sensitivity of the oedometer cells to the temperature change.

measured pore pressures are shown in Fig. 3.13(a), follows the mechanical loading step shown in Fig. 3.14(a) for Cell 1 (65 to 100 kPa) that has an intact sample from 6 meters depth and Cell 3 (100 to 150 kPa) with a sample from 9 meters depth. The pore pressures measured during the following temperature decrement (Fig. 3.13(b)) again is preceded with a mechanical loading step Fig. 3.14(b).

The excess pore pressures measured on the bottom of the clay samples under slow thermal loading (less than 3°C/hour) fall within the accuracy of the pore pressure sensor ±0.5 kPa for all data presented. This equates to ≈ 1% of the effective stress and, therefore, is unlikely to trigger additional displacements in the samples, especially for stress states below the apparent preconsolidation pressure. Furthermore, the sensitivity of the measurement system to detect changes in pore pressures is very good, considering that almost 90% of the mechanical load increment is recovered in the reading of the excess pore pressures (Figs. 3.14(a) & 3.14(b)).

After correction of the calibration data, the accuracy and repeatability of the system is considered sufficient to capture the changes in the creep rate as function of modest temperature change. Especially for the most critical load step, when the applied vertical stress passes the apparent preconsolidation pressure, the accuracy in the measured displacements of ±0.002 mm and the absence of pore pressures during thermal heating at less than 3°C/hour fulfills all the requirements.

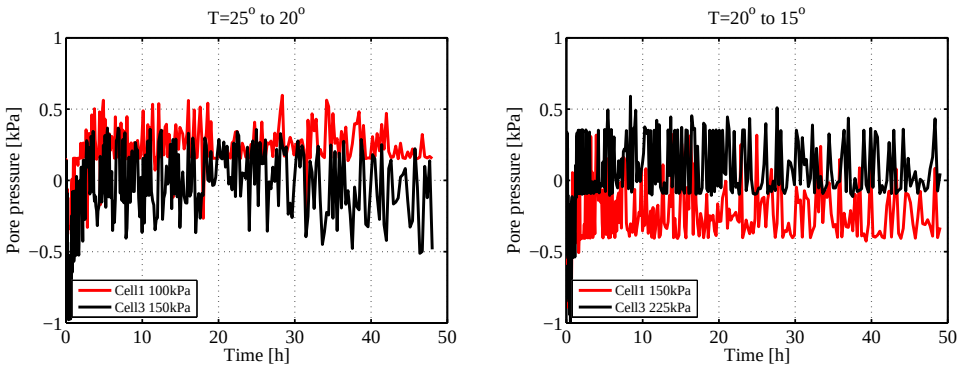

(a) Temperature decrement after first load step. (b) Temperature decrement after second load step.

Figure 3.13: Pore pressure evolution during temperature change.

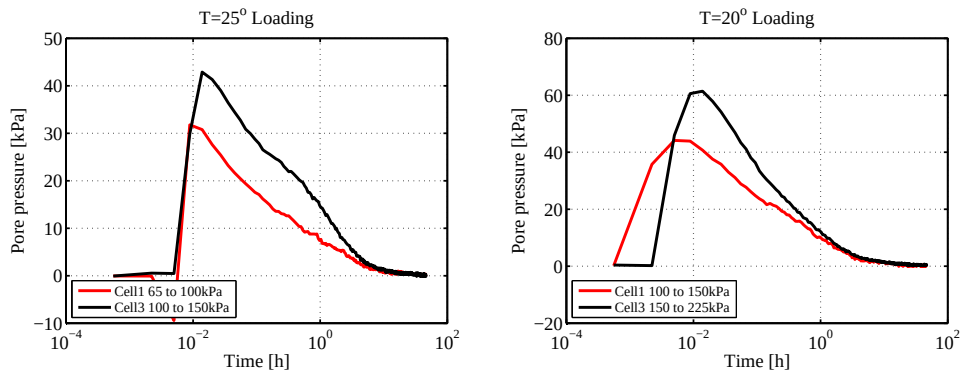

(a) First load step. (b) Second load step.

Figure 3.14: Pore pressure evolution under mechanical loading.

3.2 Material: Natural sensitive clay in Gothenburg area

3.2.1 Physical and mechanical properties of the clay

The tested natural sensitive clays are sampled from a test site for energy piles (Bergström 2017) in the Utby area of Gothenburg (Fig. 3.15). A rather homogeneous clay deposit is found from 6 to 10 meters depth. The clay consists of mainly non-expanding minerals, such as illite, chlorite, quartz, feldspar and calcite. The remaining minerals are micas, kaolinite, chlorite, heavy minerals and carbonates (Andersson-Sköld et al. 2005).

Clay samples from 6 m and 9 m depth were chosen for further testing. Although the samples have been selected with utmost care, still small variations remain, as the intact natural clay samples may contain small crushed shells or coarse grains. Remoulded samples are recreated from the intact sample material by reconstitution without adding water, and then re-consolidating to a similar in-situ stress levels as the intact samples. The basic properties for these two depths are summarised in Table. 3.1.

Table 3.1: Basic index properties of Utby clay.

Depth(m)	Initial void ratio e_0 (-)	Total density ρ(kg/m^3)	Water content w_w(%)	In-situ effective stress σ'_{v0}(kPa)	Preconsolidation pressure σ'_{pc}(kPa)
6 intact	1.977	1586	71.11	45	55
9 intact	2.142	1564	77.04	60	70
6 remoulded	1.497	1666	52.2	45	45
9 remoulded	1.392	1713	49.7	60	60

A wide range of laboratory tests that include incremental loading oedometer, CRS and triaxial tests on high quality block samples and tube samples at a reference temperature of 7 °C were performed to obtain the hydromechanical properties of the deposit (Karlsson et al. 2016). Additional 1D incremental loading oedometer tests at the reference temperature of 7 °C are performed on 50 mm diameter STII piston samples to complement the existing data and validate the new test setup. Both remoulded and intact samples from 6 meters and 9 meters depth, as listed in Table 3.1, are tested. The measured compression curves for all the reference tests are plotted in Fig. 3.16. The complete data set will subsequently be used for the calibration of the parameters for the constitutive model.

3.2.2 Thermal properties of Utby clay

In addition to the basic hydro-mechanical properties of the clay, additional thermal properties need to be measured experimentally. These are the thermal conductivity λ_T

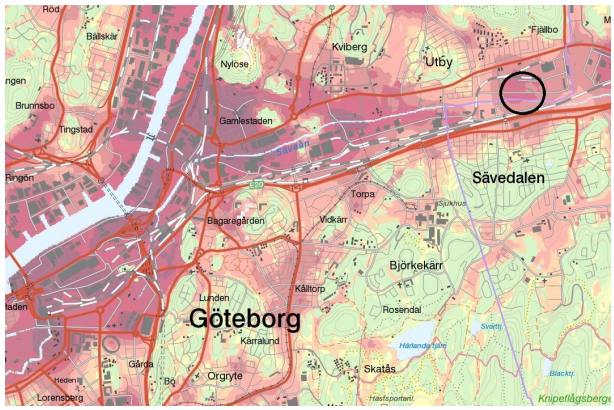

Figure 3.15: Utby test site located Northeast of Gothenburg from SGU Kartvisare.

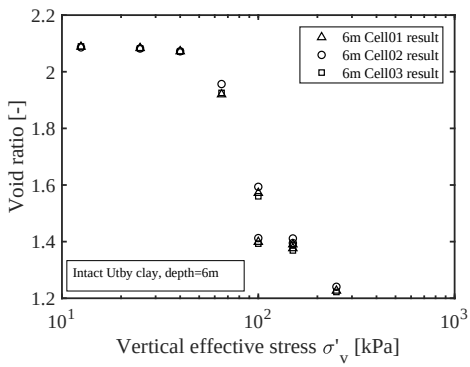

(a) Intact 6 m

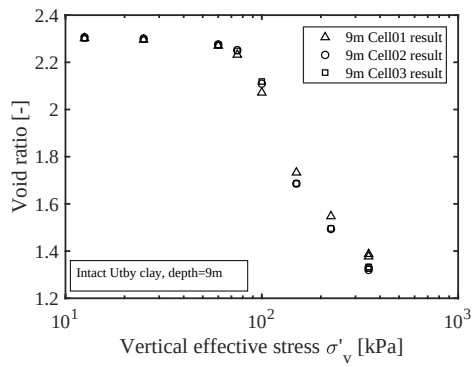

(b) Intact 9 m

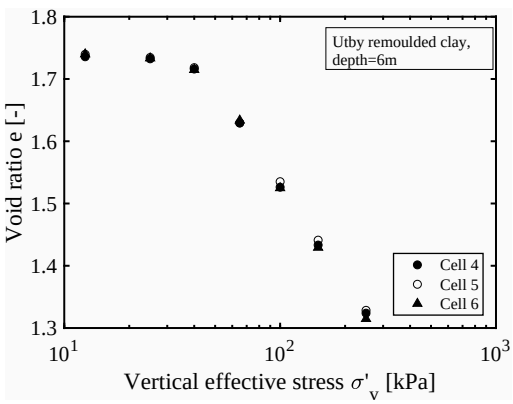

(c) Remoulded 6 m

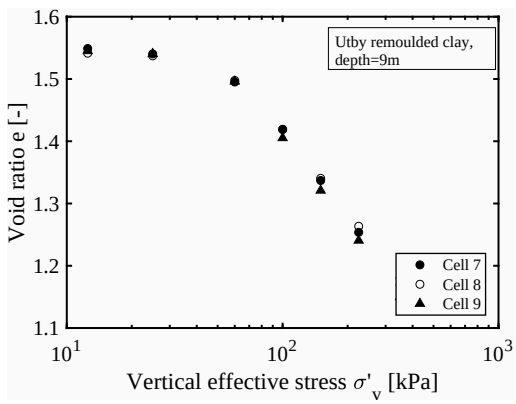

(d) Remoulded 9 m

Figure 3.16: Oedometer tests under a reference temperature of 7°C.

and the specific heat capacity C_v. Measurements of these properties are conducted before and after a test on intact samples, as well as an additional set is obtained for the remoulded samples. The thermal properties of the selected clay samples from both depths have been measured directly using a thermal needle probe, KD2 Pro Thermal Property Analyser. When using this device, however, heat is generated during the measuring process around the probe. Therefore, the thermal properties are only measured before the test on a discardable sample or after the test to prevent disturbance of the intact oedometer samples. Furthermore, the size of the probe (10 cm in length) prevents continuous monitoring of the thermal properties during the tests. The measured and estimated (using Eq. 2.4) basic thermal properties of the Utby clay samples are listed in Table. 3.2.

Table 3.2: Measured and (estimated) physical and thermal properties of Utby clay.

Sample	Void ratio e_0 [-]	Total density ρ [kg/m^3]	Heat conductivity λ_T [W/(m·K)]	Specific heat capacity C_p [J/(m^3·K)]
Intact 21°C 6 m	1.98	1586.08	1.125 (1.015)	3627 (3449)
Remoulded 21 °C 6 m	1.49	1666.53	1.178 (1.159)	3324 (3207)
Remoulded 6°C 6 m	1.39	1713.36	1.166 (1.188)	3230 (3269)

The intact samples have a higher void ratio (water content), hence lower heat conductivity and higher specific heat capacity, than the remoulded samples. In the estimation of thermal conductivity and heat capacity using Eq. 2.4 and 2.6, Ω is assumed to be 0.4 and the porosity n is derived from the measured void ratio of the clay samples. Furthermore, the thermal conductivity and the heat capacity for clay particles are assumed to be 3 W/(m·K) and 2000 J/(m^3·K), respectively. The estimated thermal properties are presented in brackets in Table 3.2. The measured thermal properties vary less in-between samples than the estimated thermal properties.

3.3 Multi-physics modelling in COMSOL

A multi-physics framework is adopted to simulate the laboratory tests in order to evaluate the capability of a thermally invariant constitutive model in capturing the clay behaviour (especially creep) under different combinations of thermal and mechanical loads. In this framework, an anisotropic rate-dependent constitutive model for soft clays (Creep-SCLAY1S) is coupled with water flow and heat transfer. The boundaries of the sample are set according to the laboratory conditions as shown in Fig. 3.9(a) and Fig. 3.1. The fluid inside and around the samples is assumed to be pure water, which is a conservative estimate. This basic modelling approach is used to design the test setup and the test programme and will further be evaluated after the experimental data is gathered. The expectation is that the creep deformations under thermal loading are underestimated using this modelling approach, and that the excess pore water pressures are not significantly affected.

In addition to the pore pressure changes caused by the volumetric strain in the clay, positive and negative excess pore pressures can be generated in the model during the heating and cooling process, due to the constrained expansion and/or contraction (ε_v in Eq. 2.13) resulting from the differences in thermal expansion of the water and the clay skeleton as discussed in Chapter 2.

Given the complex coupled processes in the temperature-controlled oedometer tests involving several materials (clay sample with water in the pores, contained in a brass ring and loaded with a brass cap with a porous stone), as shown in Fig. 3.1, the current analyses are performed on boundary value level with focus on the clay samples. This enables the application of the thermal boundaries conditions with ease, as the material surrounding the sample (brass and filter stone) react faster than the clay samples to the change of temperature.

An axisymmetric model with 74 high order triangular elements with an average size of 5 mm has been created using COMSOL Multiphysics (Fig. 3.1). The sample is 18 mm in height with a radius of 25 mm, with top and bottom drainage. The side boundaries restrict horizontal displacements, whilst at the bottom the vertical displacements are fixed.

In order to realise the multi-physics simulations, a representative constitutive model is needed. The Creep-SCLAY1S model is used to simulate the rate-dependent behaviour of the soft sensitive clay considered here. The model includes features such as volumetric hardening, creep, evolution of anisotropy and degradation of natural bonding (Gras et al. 2017; Gras et al. 2018). Here the COMSOL implementation strategy of Olsson 2013 is used by writing the differential equations of the constitutive model in an user-defined model.

The effective stress a clay sample is subjected to is expressed by Eq. 3.2, where σ'_{ij} is the tensor form of the stress state, δ_{ij} is the Kronecker delta, $i, j = 1, 2, 3$ and the mean effective stress $p' = (\sigma'_{11} + \sigma'_{22} + \sigma'_{33})/3$:

$$\sigma' = \sigma'_{ij} = \begin{bmatrix} \sigma'_{11} & \sigma'_{12} & \sigma'_{13} \\ \sigma'_{21} & \sigma'_{22} & \sigma'_{23} \\ \sigma'_{31} & \sigma'_{32} & \sigma'_{33} \end{bmatrix} \tag{3.2}$$

The strain increment corresponding to a stress increment can be expressed by Eq. 3.3. The volumetric and shear strain increment are $\dot{\varepsilon}_v$ and $\dot{\varepsilon}_d$, respectively.

$$\dot{\varepsilon} = \dot{\varepsilon}_{ij} = \begin{bmatrix} \dot{\varepsilon}_{11} & \dot{\varepsilon}_{12} & \dot{\varepsilon}_{13} \\ \dot{\varepsilon}_{21} & \dot{\varepsilon}_{22} & \dot{\varepsilon}_{23} \\ \dot{\varepsilon}_{31} & \dot{\varepsilon}_{32} & \dot{\varepsilon}_{33} \end{bmatrix} \tag{3.3}$$

The incremental strain is decomposed into an elastic part and a viscoplastic part:

$$\dot{\varepsilon}_{ij} = \dot{\varepsilon}^e_{ij} + \dot{\varepsilon}^{vp}_{ij} \tag{3.4}$$

Following the approach for the Creep-SCLAY1S model, the elastic strain is decomposed into elastic volumetric strain and shear strain, as a result the total elastic strain is rewritten into Eq. 3.5 where G is the shear modulus and K the bulk modulus which is stress dependent, $K = p'/\kappa^*$. Finally, p' is the mean effective stress and deviatoric stress is defined as $s_{ij} = \sigma'_{ij} - p'\delta_{ij}$.

$$\dot{\varepsilon}^e_{ij} = \frac{1}{2G}\dot{s}_{ij} + \frac{1}{3K}\dot{p'}\delta_{ij} \tag{3.5}$$

Reference surface and flow rule

In the following, for the sake of simplification, invariants are used. Note that invariants can only be used in triaxial stress space for vertical samples(Wheeler et al. 2003), as generally the orientation of the principle stresses and fabric do not need to coincide.

The viscoplastic strain is obtained from the flow rule, the volumetric hardening laws and the rotational hardening law defined in the constitutive model. An associated flow rule is used, so that the viscoplastic strain increment $\dot{\varepsilon}^{vp}_{ij}$ (or $\dot{\varepsilon}^{ir}_{ij}$) can be calculated using Eq. 3.6, after the determination of the reference surface f_{ref} (also called Normal Compression Surface) and the current stress surface. p'^{eq} and p'^{eq}_{ref} relate to the size of the current loading surface and the reference surface (Gras et al. 2018; Grimstad 2009; Olsson 2013; Sivasithamparam et al. 2015; Yin et al. 2011). The reference surface f_{ref} is similar to the original S-CLAY1 model by Wheeler et al. 2003 (see Fig. 3.17), which takes both the inherent and strain induced anisotropy into account.

$$\dot{\varepsilon}^{vp}_{ij} = \dot{\Lambda}\left(\frac{p'^{eq}}{p'^{eq}_{ref}}\right)^{\beta}\frac{\partial f_{ref}}{\partial \sigma'_{ij}} \tag{3.6}$$

where $\dot{\Lambda}$ is the viscoplastic multiplier, β is the visco-plastic exponent defined as $\beta = (\lambda^*_i - \kappa^*)/\mu^*_i$. λ^*_i is as the slope of the intrinsic compression line $\lambda^*_i = \Delta\varepsilon/\Delta \ln p'$, and κ^* is the slope of the swelling part of the curve. $\mu^*_i = \Delta\varepsilon/\Delta \ln t$ is the intrinsic creep index obtained from the remoulded sample. The current stress state is expressed by point (p', q) in the $p' - q$ figure as illustrated in Fig. 3.17, where $q = 2/3(s_{ij} \cdot s_{ij})^{1/2}$. The equivalent stress p'^{eq} for the current stress state of (p', q) can be calculated using Eq. 3.7. Thus, the reference surface or normal consolidation surface f_{ref} is a solid ellipse in Fig. 3.17, see Eq. 3.8. In this Equation, the shape of the loading surface depends on the current anisotropy α, which represents the inclination of the reference surface, and the model parameter M which represents the inclination of the critical state and is Lode angle θ dependent. The ratio between the current stress surface f and the reference surface f_{ref} dictates the strain rate. The size of the reference surface p'^{eq}_{ref} is related to the apparent preconsolidation pressure of the soil.

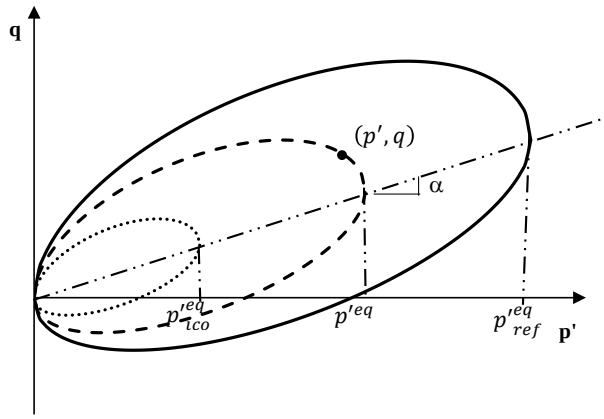

Figure 3.17: Stress state and reference surface.

$$p'^{eq} = p' \frac{(M^2 - \alpha^2) + (q/p' - \alpha)^2}{M^2 - \alpha^2} \tag{3.7}$$

$$f_{ref} = p' \frac{(M^2 - \alpha^2) + (q/p' - \alpha)^2}{M^2 - \alpha^2} - p'^{eq}_{ref} = 0 \tag{3.8}$$

Anisotropy and rotation law

Assuming that the elastic strains are negligible compared to the viscoplastic strains, volumetric visco-plastic strain ε_v^{vp} (Eq. 3.9) and deviatoric visco-plastic strain ε_d^{vp} (Eq. 3.10) will develop as a function of time according to Eq. 3.11, where $\eta = q/p'$ is the stress ratio.

$$\dot{\varepsilon}_v^{vp} = \dot{\Lambda} \left(\frac{p'^{eq}}{p'^{eq}_{ref}} \right)^{\beta} \frac{\partial f_{ref}}{\partial p'} \tag{3.9}$$

$$\dot{\varepsilon}_d^{vp} = \dot{\Lambda} \left(\frac{p'^{eq}}{p'^{eq}_{ref}} \right)^{\beta} \frac{\partial f_{ref}}{\partial q} \tag{3.10}$$

$$\frac{\dot{\varepsilon}_d^{vp}}{\dot{\varepsilon}_v^{vp}} = \frac{\partial f}{\partial q} \Big/ \frac{\partial f}{\partial p'} = \frac{2(\eta - \alpha)}{M^2 - \eta^2} \tag{3.11}$$

The evolution of α, the inclination of the reference surface, depends on the volumetric and

deviatoric strain rates $\dot{\varepsilon}_v^{vp}$ and $\dot{\varepsilon}_d^{vp}$, and is controlled by two additional model parameters ω and ω_d which are the absolute rate of rotation and the relative rate of rotation, respectively.

$$\dot{\alpha_d} = \omega \left[\left(\frac{3\eta}{4} - \alpha \right) \langle \dot{\varepsilon}_v^{vp} \rangle + \omega_d \left(\frac{\eta}{3} - \alpha \right) \dot{\varepsilon}_d^{vp} \right] \tag{3.12}$$

The initial inclination of the reference surface α_0 is obtained assuming the K_0 condition of the clay: $\dot{\varepsilon}_2 = \dot{\varepsilon}_3 = 0$. $\dot{\varepsilon}_v = \dot{\varepsilon}_1 + \dot{\varepsilon}_2 + \dot{\varepsilon}_3$, $\dot{\varepsilon}_d = 2/3 * (\dot{\varepsilon}_1 - \dot{\varepsilon}_3)$. When assuming that the elastic strains are negligible compared with the viscoplastic strains, Eq. 3.11 becomes Eq. 3.13 in one-dimensional compression.

$$\frac{\partial f}{\partial q} / \frac{\partial f}{\partial p'} = \frac{\dot{\varepsilon}_d^{vp}}{\dot{\varepsilon}_v^{vp}} = \frac{2}{3} \tag{3.13}$$

In one-dimensional compression, the stress ratio $\eta = \eta_{K0} = 3(1 - K_0)/(1 + 2K_0)$. The initial value for the inclination of the reference surface becomes Eq. 3.14 after combining Eqs. 3.11 with Eq. 3.13, where M_c is the inclination of Critical State line in compression tests.

$$\alpha_{K0} = \frac{3\eta_{K0} - M_c^2 + \eta_{K0}}{3} \tag{3.14}$$

If the clay sample is continuously loaded in under a K_0 stress path, $\alpha = \alpha_{K0}$ keeps constant and $\dot{\alpha} = 0$. Eq. 3.15 can be derived by combining Eqs. 3.12 & 3.11:

$$\omega_d = \frac{3(4M_c^2 - 4\eta_{K0}^2 - 3\eta_{K0})}{8(\eta_{K0}^2 + 2\eta_{K0} - M_c^2)} \tag{3.15}$$

Hardening and degradation of the bonds

The hardening law in Creep-SCLAY1S is temperature-independent. The change in the apparent preconsolidation pressure increases as function of viscoplastic volumetric strain as expressed in Eq. 3.16, where λ_i^* and κ^* are the modified intrinsic compression index and modified swelling index, respectively.

$$\dot{p'}_{ref}^{eq} = \frac{p_{ref}'^{eq}}{\lambda_i^* - \kappa^*} \dot{\varepsilon}_v^{vp} \tag{3.16}$$

For natural soft clays, initially a higher stiffness is observed which is associated to weak bonding between the particles. These initial bonds are significant in sensitive soft clays and degrade upon loading (Karstunen et al. 2005) with irrecoverable deformation. The concept of an intrinsic reference surface (Gens and Nova 1993) is used to describe this mechanism, the size of which is linked to the size the reference surface via structure

parameter χ that describes the amount of bonding (Eq. 3.17):

$$p'^{eq}_{ref} = (1+\chi)p'^{eq}_{ic0} \tag{3.17}$$

The evolution law for the amount of bonding χ is given by Eq. 3.18 and relates to the developed (viscoplastic) strains:

$$\dot{\chi} = -\chi\xi\left(|\dot{\varepsilon}^{vp}_{v}| + \xi_d\dot{\varepsilon}^{vp}_{d}\right) \tag{3.18}$$

where χ is the current amount of bonding, ξ and ξ_d are the absolute rate of rotation and relative rate of rotation, respectively. At large stress levels the natural bonding of the clay is fully destroyed.

Using the data obtained from the high quality block samples, the initial amount of bonding χ_0 for the tested intact clay varies between 25 and 35 (Karlsson et al. 2016). In contrast, in the current tests some sample disturbance from the STII piston sampler is present. The reference oedometer tests (Fig. 3.16) under the constant temperature of 7 °C are used to derive the destructuration parameters. Following Kutter and Sathialingam (1992), the general equation of a change in the viscoplastic strain can be written as Eq. 3.19 for the 1D condition.

$$\dot{\varepsilon}^{vp}_{vK0} = \frac{\mu^*_i}{\tau}\left(\frac{\sigma'_v}{\sigma'_{pc}}\right)^{(\lambda^*_i-\kappa)/\mu^*_i} \tag{3.19}$$

where τ is the reference time which depends on the duration of the loading increments used for defining the apparent preconsolidation pressure σ'_{pc}. For the reference test in this work τ is 1 day. By combining the viscoplastic volumetric strain rate obtained from Eq. 3.19 with Eq. 3.9, a viscoplastic multiplier can be defined as Eq. 3.20:

$$\dot{\Lambda} = \frac{\mu^*_i}{\tau}\frac{M^2_c - \alpha^2_{K0}}{M^2_c - \eta^2_{K0}} \tag{3.20}$$

Thus, the viscoplastic strain increment can be calculated with Eq. 3.21.

$$\dot{\varepsilon}^{vp}_{ij} = \frac{\mu^*_i}{\tau}\frac{M^2_c - \alpha^2_{K0}}{M^2_c - \eta^2_{K0}}\left(\frac{p'^{eq}}{p'^{eq}_{ref}}\right)^{(\lambda^*_i-\kappa)/\mu^*_i}\frac{\partial f}{\partial \sigma'_{ij}} \tag{3.21}$$

3.4 Test programme

Below a certain depth, the temperature in the clay deposit is independent of the ambient air temperature, usually corresponding to the average air temperature, which is about 7.8°C in the Gothenburg area. Previous reference tests were carried out in a temperature-controlled laboratory at 7°C. In this study, a temperature range from from 5 to 25 °C

was selected to correspond to the temperature of interest for energy structures in Sweden.

3.4.1 Static heating and cooling oedometer tests

The tests in this work are planned assuming that the samples from a given depth can be considered as identical. As opposed to the traditional oedometer test, where a single sample is sequentially loaded with different loads, in this research multiple samples are loaded simultaneously at different stress levels. The samples are fresh, i.e. tested within two weeks after sampling, and rather impermeable, so re-saturation is not deemed necessary. The water used around the sample is tap water to reduce the influence on pore water chemistry.

A compression curve is constructed from six independent oedometer tests, each loaded to a different stress state. This requires close to identical clay samples. The natural clay samples from the same tube have slight variations in void ratio. The six oedometer specimens are cut from the same piston sample, which is 50 mm in diameter and 150 mm in height. The potential variation between the six oedometer samples is similar to the variation within a triaxial sample. Hence, the differences are sufficiently small to consider samples from the same depth as equal, i.e. all samples start from a comparable void ratio after re-loading to the in-situ stress state.

With this premise, the test programme described in Table 3.3 is designed. Normally 24 hour load increments are deemed more than sufficient to study the creep rate. Given the low hydraulic conductivity of the sensitive clays studied, for which the degree of consolidation U_v reaches 90% after 13 hours in trial tests, the duration of each step is increased to 48 hours to ensure pure creep after the mechanical and thermal loading increments. This allows to study the creep of the sensitive clay samples under both thermal and mechanical variations with sufficient accuracy.

A total of 12 oedometer cells are used in parallel, six for each depth. For each depth, six stress levels are selected, representing three stress states below the apparent preconsolidation pressure σ'_{pc}, and three above the apparent preconsolidation pressure σ'_{pc}: $\sigma'_1 < \sigma'_2 < \sigma'_3 < \sigma'_{pc} < \sigma'_4 < \sigma'_5 < \sigma'_6$. The last stress level is about three times the apparent preconsolidation pressure $\sigma'_6 \approx 3\sigma'_{pc}$, and consequently at this stress level the natural structure of the clay would be expected to be destroyed to a large extent. The six stress states for the samples from 6 m depth are: 12.5 kPa, 25 kPa, 40 kPa, 65 kPa 100 kPa and 150 kPa, and for 9 m depth these are: 12.5 kPa, 25 kPa, 60 kPa, 100 kPa, 150 kPa and 225 kPa. The temperatures T_1 to T_5 start from 25 °C (5 °C) to 5 °C (25 °C) with 5 °C cooling decrements (heating increments), respectively, as listed in Table 3.4. In each step, the clay samples are allowed to deform for 48 hours, until the next mechanical or thermal loading step is applied.

All samples are first loaded to the estimated in-situ vertical effective stress level σ'_{v0}, as reported in Table 3.1 under the temperature of T_1, before starting the loading procedure

(Table 3.3). Each step has six components as listed in Table 3.5. In Step 1, six samples are loaded separately to six different stress levels from σ_1 to σ_6 which are specified as S_{11}, S_{12}, S_{13}, S_{14}, S_{15} and S_{16} (Table 3.5). Subsequently, the vertical effective stress vs. void ratio response in Fig. 3.18(a) under temperature of T_1 can be plotted by combining the results of the six individual tests. In Step 2, each sample is loaded to the next stress level resulting in six additional points, S_{21}, S_{22}, S_{23}, S_{24}, S_{25} and S_{26}, for an additional compression curve shown in Fig. 3.18(b). These six stress states can be combined to construct another compression curve, on the basis of the consistent $e - \log t$ curves for each cell. After Step 2, the mechanical loads are maintained, and only the temperature is changed from T_1 to T_2, which is Step 3. After 48 hours, each cell is loaded again to the next stress level in Step 4.

In the following steps, each mechanical loading step is followed by a temperature change or vice versa. Table 3.3 shows that after 10 steps for both heating and cooling tests, five compression curves with five temperature levels for a tested depth can be plotted. For each cell, a full loading path that consists of 10 steps (including both thermal and mechanical loading) can be plotted, for example S_{11} to S_{101} for Cell 1 (Fig. 3.18(c)) and S_{12} to S_{102} for Cell 2 (Fig. 3.18(d)). In addition, the steps S_{24}, S_{43}, S_{62}, S_{81} can be used to compare the void ratio change when samples are loaded from σ_4 to σ_5 under T_1, T_2, T_3 and T_4, respectively, as plotted in Fig. 3.18(e). The steps S_{34}, S_{53}, S_{72}, S_{91} can be used to compare the void ratio change when samples are subjected to the same load increment $\sigma' = \sigma_5$, but are thermally loaded to different temperatures (T_1 to T_2, T_2 to T_3, T_3 to T_4 and T_4 to T_5) as plotted in Fig. 3.18(f).

Hence, by following this test programme, compression curves at different temperatures can be obtained, together with temperature differentiated void ratio-time curves ($e - \log t$) which can be used to investigate the effect of temperature on creep rate. The data evaluation is discussed in the following Section.

3.4.2 Oedometer tests with quasi-static thermal loading

In real geothermal systems, the energy in the clay is extracted (in winter) and stored (in summer) seasonally. To study the impact of these systems on the surrounding clay for the life-time of the geothermal structure, hundreds of thermal cycles are required. As opposed to field tests, element level laboratory tests offer favourable scaling and control. Tens of cycles can be realised within a few weeks, offering a 25-fold speed-up in test time compared to the complementary field test (Bergström 2017). In addition, the field tests are complicated by the non-constant temperature variations in the shallow subsurface due to (daily and) yearly cycles, as shown in Fig. 3.19.

To study the clay behaviour during and after cyclic thermal loading, the temperature itself needs to be regulated to correspond to a geothermal system, which in turn is affected by the outside temperature variations. The average constant temperature of the clay at depth is equal to the average yearly ambient air temperature.

Table 3.3: Test procedure for oedometer cooling tests for the clay from one depth.

Step	Temperature	Time /h	O_1	O_2	O_3	O_4	O_5	O_6
1	T_1	48	σ_1	σ_2	σ_3	σ_4	σ_5	σ_6
2	T_1	48	σ_2	σ_3	σ_4	σ_5	σ_6	σ_1
3	T_2	48	σ_2	σ_3	σ_4	σ_5	σ_6	σ_1
4	T_2	48	σ_3	σ_4	σ_5	σ_6	σ_1	σ_2
5	T_3	48	σ_3	σ_4	σ_5	σ_6	σ_1	σ_2
6	T_3	48	σ_4	σ_5	σ_6	σ_1	σ_2	σ_3
7	T_4	48	σ_4	σ_5	σ_6	σ_1	σ_2	σ_3
8	T_4	48	σ_5	σ_6	σ_1	σ_2	σ_3	σ_4
9	T_5	48	σ_5	σ_6	σ_1	σ_2	σ_3	σ_4
10	T_5	48	σ_6	σ_1	σ_2	σ_3	σ_4	σ_5
	In total	20 days						

Note: O_1 represents the first oedometer cell, σ_1 represents the first vertical stress state and T_1 is the first target temperature in the test.

Table 3.4: Applied temperatures in heating and cooling tests.

Temperature	T_1	T_2	T_3	T_4	T_5	
In cooling tests (°C)	25	20	15	10	5	
In heating tests (°C)	5	10	15	20	25	
Stress	σ_1	σ_2	σ_3	σ_4	σ_5	σ_6
6 meters (kPa)	12.5	25	40	65	100	150
9 meters (kPa)	12.5	25	60	100	150	225
Cell number	O_1	O_2	O_3	O_4	O_5	O_6
6 meters (°C)	Cell 04	Cell 05	Cell 06	Cell 07	Cell 08	Cell 09
9 meters (°C)	Cell 10	Cell 11	Cell 12	Cell 13	Cell 14	Cell 15

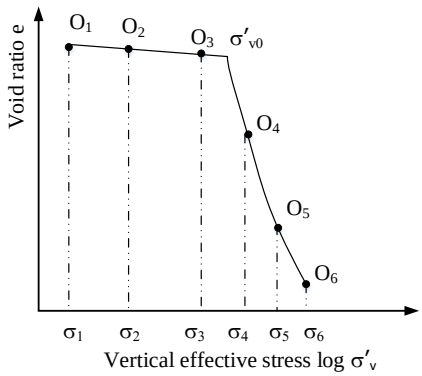

(a) Step1

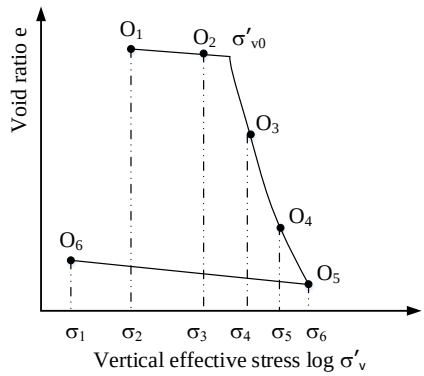

(b) Step2

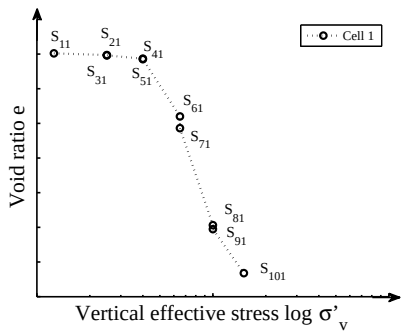

(c) Cell1

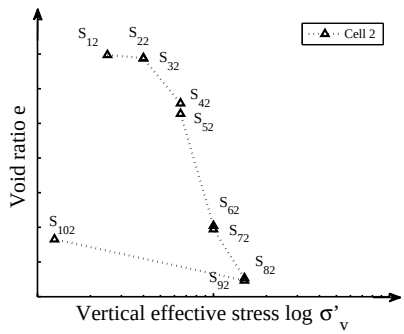

(d) Cell2

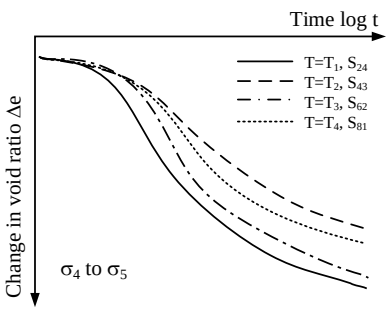

(e) Mechanical loading

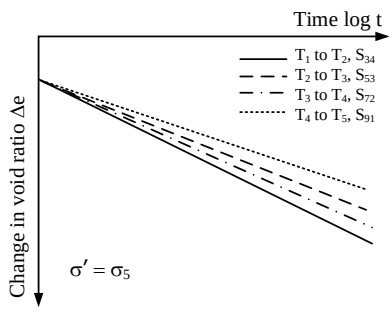

(f) Thermal loading

Figure 3.18: Test analyses for for slow heating and cooling tests.

Table 3.5: Plan for data analysis after a group of tests.

Step	Temperature	Time/h	O_1	O_2	O_3	O_4	O_5	O_6
1	T_1	48	S_{11}	S_{12}	S_{13}	S_{14}	S_{15}	S_{16}
2	T_1	48	S_{21}	S_{22}	S_{23}	S_{24}	S_{25}	S_{26}
3	T_2	48	S_{31}	S_{32}	S_{33}	S_{34}	S_{35}	S_{36}
4	T_2	48	S_{41}	S_{42}	S_{43}	S_{44}	S_{45}	S_{46}
5	T_3	48	S_{51}	S_{52}	S_{53}	S_{54}	S_{55}	S_{56}
6	T_3	48	S_{61}	S_{62}	S_{63}	S_{64}	S_{65}	S_{66}
7	T_4	48	S_{71}	S_{72}	S_{73}	S_{74}	S_{75}	S_{76}
8	T_4	48	S_{81}	S_{82}	S_{83}	S_{84}	S_{85}	S_{86}
9	T_5	48	S_{91}	S_{92}	S_{93}	S_{94}	S_{95}	S_{96}
10	T_5	48	S_{101}	S_{102}	S_{103}	S_{104}	S_{105}	S_{106}
	In total	20 days						

Note: S_{11} is the first step for the first oedometer cell

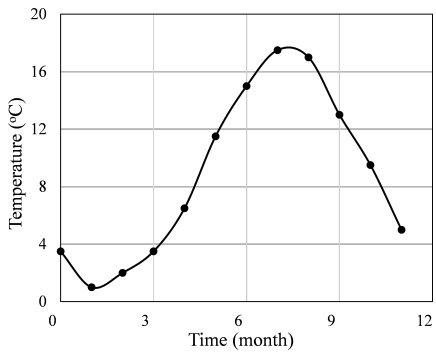

Figure 3.19: Average temperature for each month in a year in Gothenburg area (www.worldweatheronline.com).

The temperature in Fig. 3.19 is represented by a sinusoidal function Eq.(3.22) with a scaled time-period, where t_p is the period for one full cycle in hours, A is the amplitude of the periodic temperature, t is time in seconds, ω_0 is the initial phase that depends on the starting point of the simulation, and T_{avg} is the average annual temperature. The largest time-period is conservatively chosen to have a similar heating rate (3.8 °C/hour) compared to the static thermal tests in Section. 3.4.1. To have a better match with the field test, the time-period is gradually reduced to correspond to the excess pore pressures measured in the field.

$$T = A_T sin(\frac{2\pi}{t_p}\frac{t}{3600} + \omega_0) + T_{avg} \tag{3.22}$$

The testing programme is presented in Table 3.6. In addition to different time-periods T_p and temperature amplitude A, samples from the two depths are tested at relevant stress levels: σ_3 is close to the in-situ effective stress σ'_{v0}, σ_4 just above the apparent preconsolidation pressure and σ_5 represents a stress state where the clay is largely remoulded. The subscript is consistent to the loading steps of the static test series.

After 40 thermal cycles under constant external stress level (σ_3, σ_4 and σ_5 for Cell 1, Cell 2 and Cell 3, respectively), the samples will be subsequently loaded to the next stress level (σ_3 to σ_4, σ_4 to σ_5 and σ_5 to σ_6) before the tests are terminated. This last step allows to evaluate the change in mechanical properties due to thermal cycles.

Table 3.6: Cyclic loading process for samples from one depth.

Period (h)	Initial	Amplitude (°C)	Number	Vertical stress (kPa)		
T_P	temperature (°C) T_0	A	of cycles	Cell 1	Cell 2	Cell 3
4	15	10	10	σ_3	σ_4	σ_5
8	15	10	10	σ_3	σ_4	σ_5
12	15	10	10	σ_3	σ_4	σ_5
16	15	10	10	σ_3	σ_4	σ_5

As discussed in this Chapter, static and quasi-static heating and cooling systems were developed for temperature-controlled oedometer tests. These oedometer tests will be used to systematically study the influence of temperature on the rate-dependent behaviour of natural and remoulded soft clay from the Utby test site.

4 Oedometer tests with static thermal loading[1]

In this Chapter, the evolution of the creep rate $C_{\alpha e}$ under temperature change is analysed using the data from the quasi-static temperature-controlled oedometer tests that follow the experimental plan outlined in Table 3.3. In addition to the creep rate, the permeability K, as well as the modified compression λ^* and swelling indices κ^* are derived. In the following, the representative results are evaluated in detail with the help of numerical analyses.

4.1 Experimental results

During oedometer tests, the vertical stresses at a given time applied to the samples are pre-defined. Quantities such as temperature, vertical displacement and pore pressures are measured directly during the entire test. The hydro-mechanical parameters of the tested clays, for example the modified compression and swelling indices, the creep rate and the permeability, are evaluated from the measurement data.

4.1.1 Measured displacements and strains

A basic vertical strain-time curve can be obtained by selecting the appropriate test data, using the information from Table 3.3, under each mechanical loading step. For example for Step 2 of the cooling tests, the temperature is 25 °C and six oedometer cells were loaded simultaneously with six different stress levels according to the in-situ stress and the estimated apparent preconsolidation pressures of the corresponding depths (i.e. Table 3.3). The time-vertical strain plots for intact clay sampled from a depth of both 6 and 9 meters are shown in Fig. 4.1, assuming compression as negative. As expected, the increase in the axial strain is the largest for the load step of 100 kPa, which is not the highest stress level applied in the test, but at a stress level a step or two after the apparent preconsolidation pressure (see Table. 3.1). For the sample at 6 m depth (Fig. 4.1(a)), the acceleration of creep already starts at the load of 65 kPa, and shows no slowing-down.

After the application of constant mechanical loads using dead weights, samples are allowed to consolidate and creep for 48 hours before the thermal loading decrement (increment). In this step the room temperature is adjusted with 5°C decrement (increment) in the cooling (heating) tests. The axial strain is continuously monitored during these 5°C decrement or increment. Hence, the loading is due to temperature change alone. For example, Step 3 in the cooling tests, with the temperature in the climate room regulated

[1]Part of this Chapter is published in (Li et al. 2018)

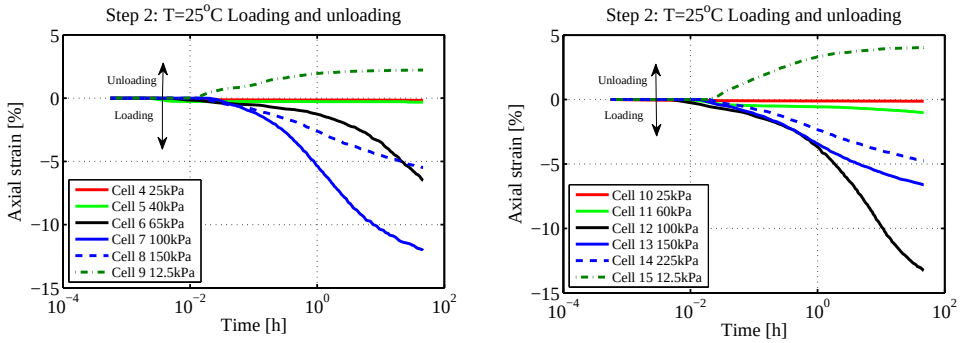

(a) depth=6 m (b) depth=9 m

Figure 4.1: Development of strain under mechanical loading.

from 25°C to 20°C, is plotted in Fig. 4.2. The time-axis in these figures is plotted as a continuation from the previous mechanical load steps plotted in Fig. 4.1, in logarithmic scale. Similarly to the mechanical loading tests presented in Fig. 4.1, the increments in the axial strains under cooling are highest for the samples under the load steps just above the apparent preconsolidation pressures, around 100 kPa. There is no tendency for a gradually decreasing creep rate during the 48 hours, in which the temperature is decreased from 25°C to 20°C over a period of 3-4 hours. As discussed in Chapter 3, even though the strain are small, the strain magnitudes are above the detection threshold. The results suggest that both mechanical loading and temperature change trigger creep deformations in soft natural clays. Due to the complex and somewhat competing mechanisms involved, the results need further interpretation using numerical modelling (Section 4.2).

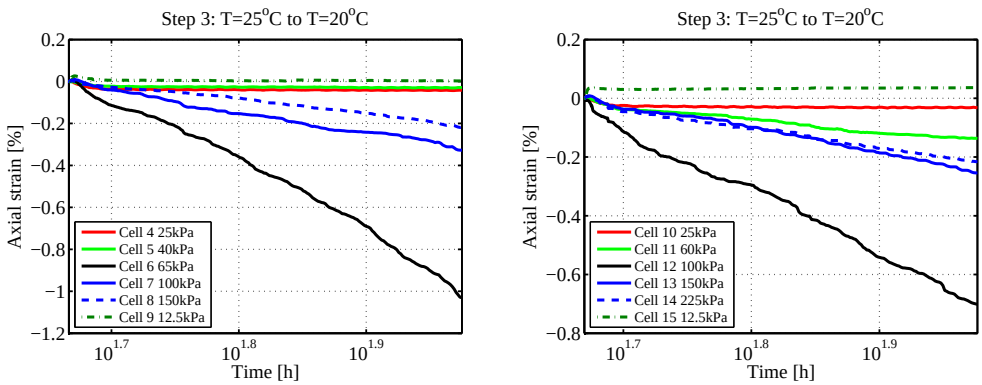

(a) depth=6 m (b) depth=9 m

Figure 4.2: Strain development during cooling.

In the following, the behaviour of sensitive clays under combined thermal and mechanical

loading is analysed. The basis of the interpretation of the results is that test results on different samples can be combined. Figure 4.3 shows the time-void ratio curves of six simultaneous oedometer tests on independent clay samples from the same depth, the depth of 9 meters at different load steps (stress levels in Step 2 from the heating test). The consistency between the independent samples enables the further analyses, such as studying the temperature dependency of other mechanical parameters that require the combination of the data of multiple cells (Section 3.4.1).

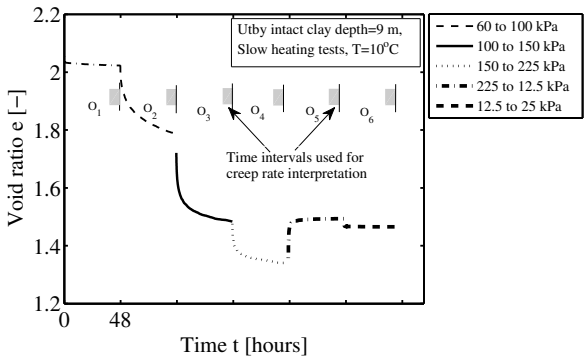

Figure 4.3: The evaluation of compression curves.

In addition to the mechanical loading steps, there are four thermal loading steps in the test procedure. In these steps the temperature of the room is changed from one temperature to the next target temperature. The latter process takes less than four hours. Figure 4.4 shows the change in the void ratio at certain stress level for different thermal loading steps. Based on Figs. 4.4(b) and 4.4(d), it can be concluded for clay samples from both depths that the rates of change of the void ratio increase at a stress level of 100 kPa upon heating. This change is not as clear when the samples are subjected to cooling, as can be seen in Figs. 4.4(a) and 4.4(c). Thus, for normally consolidated natural clays, heating leads to softening of the clay (i.e. in the decrease in the apparent preconsolidation pressure), and the subsequent hardening tries to compensate for this softening. Unloading and reloading are also included in the test programme. Thermal dilation is observed in steps S_{36}, S_{55}, S_{74} and S_{93} (see Table 3.5), when the samples are unloaded from the highest stress level to 12.5 kPa. As a result, the over-consolidation ratio (OCR) increases to 12 and 18, respectively, for samples from 6 m and 9 m depth. In contrast, no thermal dilation upon heating is observed for the intact samples in step S_{56}, S_{75} and S_{94}, when the value of OCR is 6 and 9, respectively, for samples from 6 m or 9 m depth.

Step 5, where the paths of the heating and cooling tests meet, is further analysed to study the effect of the structure on creep rate upon heating and cooling, as function of the stress state. In this step both heating and cooling samples are thermally loaded to the same target temperature 15 °C with the same stress history, but then respectively heated from 10 °C to 15 °C and cooled from 20 °C to 15 °C. It means that after three hours of temperature change in 15 °C, the apparent preconsolidation pressure σ'_{pc} of the samples

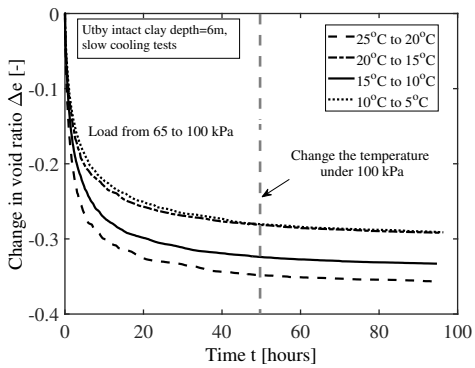

(a) depth=6 m cooling

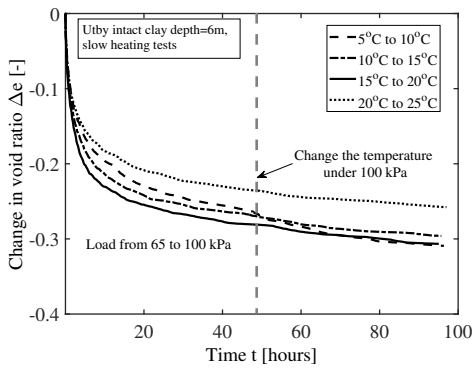

(b) depth=6 m heating

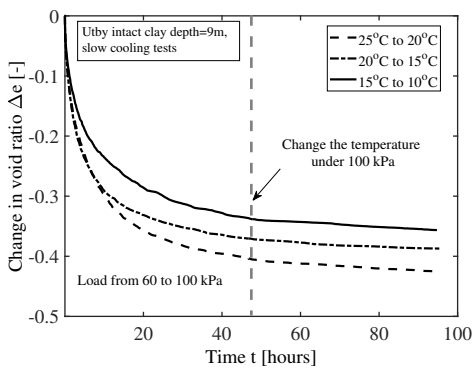

(c) depth=9 m cooling

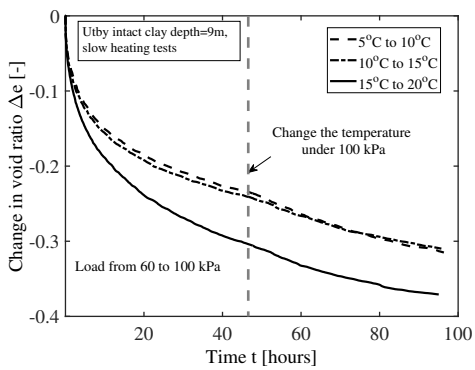

(d) depth=9 m heating

Figure 4.4: Difference in heating and cooling.

is expected to reach a similar level σ'^{15}_{pc}. The deformation during the temperature change for both of the conditions is plotted in Fig. 4.5, for both intact and remoulded samples. Even under the same stress state and with the same stress history, the deformation differs greatly between heating and cooling, as shown in Figs. 4.5(a) and 4.5(c). This is a reasonable response when the accelerated deformations (thus hardening), partly compensate for the thermal softening during heating, and vice versa under cooling. This difference also indicates that the compressibility of natural sensitive clays under certain effective stress and temperature depends on the stress history, as well as the temperature history, and not just solely the current stress and temperature level. In contrast, for samples without much natural structure left (remoulded samples or samples exposed to large stress levels) the temperature effects are rather insignificant, as seen in Figs. 4.5(b) and 4.5(d). It appears that the influence of the temperature on the emerging creep rate strongly depends on the presence of the apparent bonding in the natural sensitive clays.

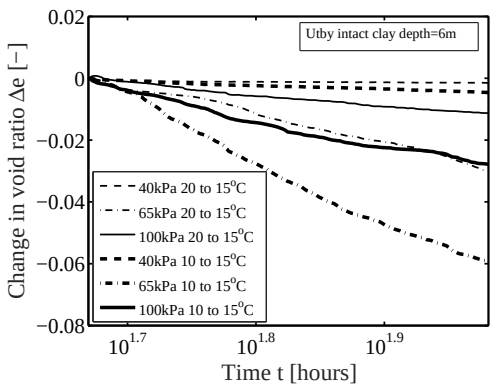

(a) depth=6 m Intact

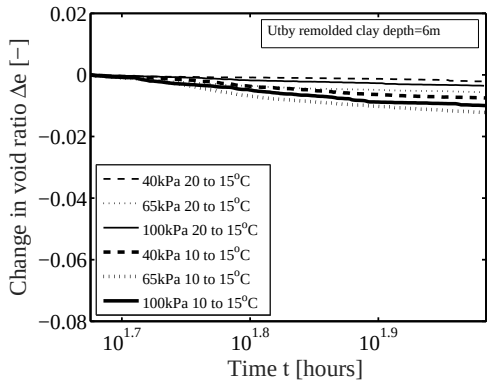

(b) depth=6 m Remoulded

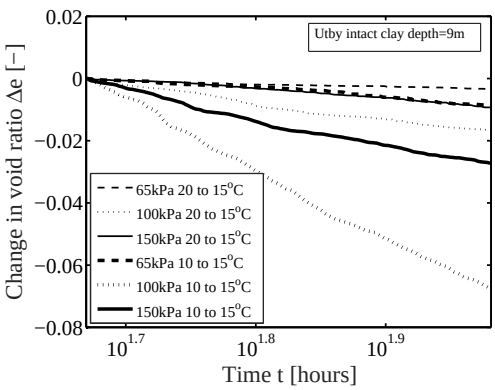

(c) depth=9 m Intact

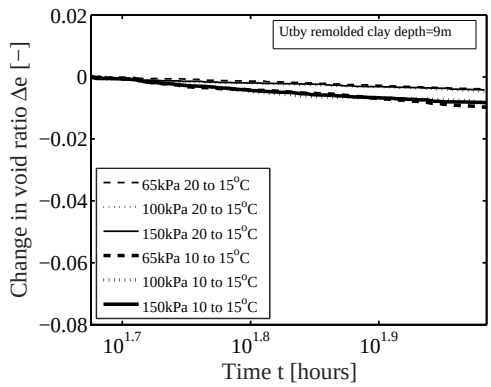

(d) depth=9 m Remoulded

Figure 4.5: Strain development during mechanical loading.

4.1.2 Modified compression λ^* and swelling index κ^*

With the assumption that all the samples from the same depth are comparable, the modified compression index and swelling index, as well as the creep rate, the hydraulic conductivity and the apparent preconsolidation pressure can be determined as a function of effective stress levels and temperatures, by combining the experimental results from parallel samples.

A compression curve is constructed from six different samples for each load step. In each test group (either heating or cooling), three groups of data at two different temperatures (Steps 1, 2 and 4 in Table 3.3) are used form the compression curves, which cross over the apparent preconsolidation pressure. For intact samples from 6 m depth, the compression curves for separate samples under five target temperatures fall well into one, as shown in Fig. 4.6 for the slow cooling tests. These results show that only after the apparent preconsolidation pressure, the compression curves start to diverge for different temperatures. This is especially true at stress levels beyond the apparent preconsolidation pressure σ'_{pc}. Unfortunately, there is not enough data around the apparent preconsolidation pressure to estimate the value accurately.

The compression curves for four different temperatures (5 °C and 10 °C in heating, 25 °C and 20 °C in cooling) passing through the apparent preconsolidation pressure are plotted in Fig. 4.7 for both natural and remoulded samples. A consistent temperature dependency is observed for the intact samples, in contrast to the reconstituted ones. The difference in the accumulated thermal deformation is larger for samples from 9 meters depth (Fig. 4.7(b)) than for samples from 6 meters depth (Fig. 4.7(a)), because of the larger void ratio in samples from 9 meters. The differences between the compression curves for the intact samples reduce with increasing stress level. The compression curve for the intact samples starts to approach the curve for the remoulded samples at large stress levels. However, even at the highest stress level applied, which is around three times the apparent preconsolidation pressure σ'_{pc} ($\sigma'_6 \approx 3\sigma'_{pc}$), the apparent bonding in the intact clay samples is not fully destroyed, as shown with the trend lines in Fig. 4.7(b).

When it comes to compression, in this thesis the modified compression and swelling indices λ^* and κ^* are defined with Eq.4.1 and Eq.4.2.

$$\lambda^* = \frac{\Delta\varepsilon}{\Delta \ln \sigma'_v} \quad \text{(in virgin compression part)} \tag{4.1}$$

$$\kappa^* = \frac{\Delta\varepsilon}{\Delta \ln \sigma'_v} \text{ (in swelling part)} \tag{4.2}$$

For each step, the values of the modified compression index λ^* and modified swelling

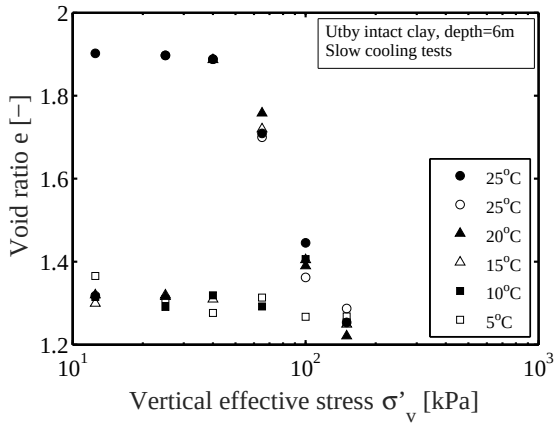

Figure 4.6: The evaluation of compression curves at different temperature.

index κ^* depend on the selected effective stress interval as shown in Fig. 4.8. For intact clays, the modified compression index is largest for the load steps that pass through the apparent preconsolidation pressure labelled as λ_2^* in Fig. 4.8(a) and λ_1^* in Fig. 4.8(b). In intact natural clays, a common explanation for this behaviour is that the bonds between the clay particles gradually degrade after the yield (Karstunen et al. 2005). The modified swelling index is obtained from the unloading-reloading curves (κ_2^* in Fig. 4.8(a)). Only in the absence of the unloading-reloading loop, the initial loading curves before the apparent preconsolidation pressure (κ_1^* in Fig. 4.8(a)) are utilised. The unloading-reloading curves after the highest stress level involving multiple points are averaged with one modified swelling index value, see κ^* in Fig. 4.8(b), because of the uncertainties in the unloading curves resulting from the construction of these curves using data from different samples (unloading from different void ratio).

From all the data gathered in the mechanical Steps 1, 2, 4, 6, 8 and 10 from both heating and cooling test programmes, up to five groups of modifies compression λ^* and swelling indices κ^* can be derived, corresponding to 5 different temperatures, as shown in Figs. 4.9 & 4.10. The modified compression index of the remoulded samples is relatively constant at 0.08 over the tested temperature range of 5°C to 25°C. In contrast, the scatter for the λ^* values of the intact samples makes it impossible to draw conclusions. The origin of the scatter arises from the few and varying number of data points for each temperature level available for the determination of λ^* (Fig. 4.8). Furthermore, the testing programme resulted in a slightly different mechanical loading history for each temperature level, which leads to additional scatter in the results for the intact samples, which are more sensitive.

The range of the evaluated modified swelling indices κ^* falls around the values for the reference tests on intact and remoulded samples that follow the standard test procedure on a single sample at the constant temperature of 7°C. The magnitude of the scatter is ±50% and is larger than ±20%, commonly obtained for the clays tested in the geotechnical

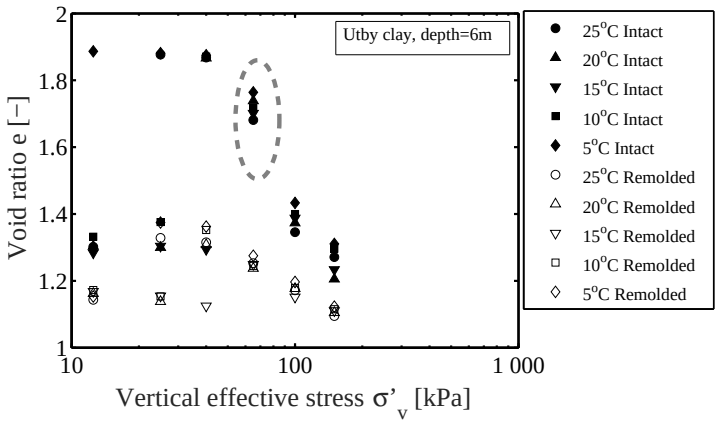

(a) Depth = 6 m

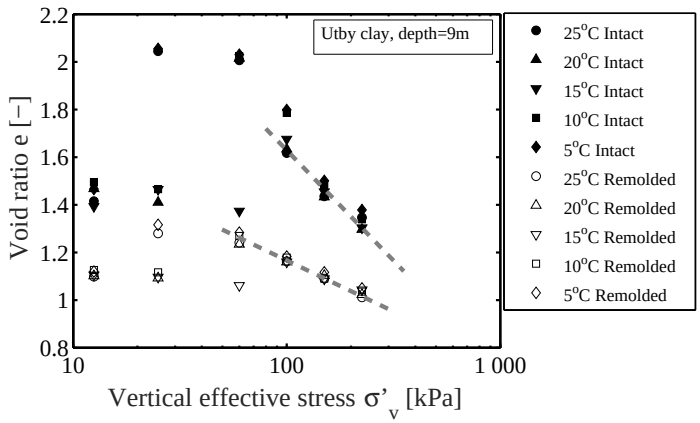

(b) Depth = 9 m

Figure 4.7: Compression curves under different target temperatures.

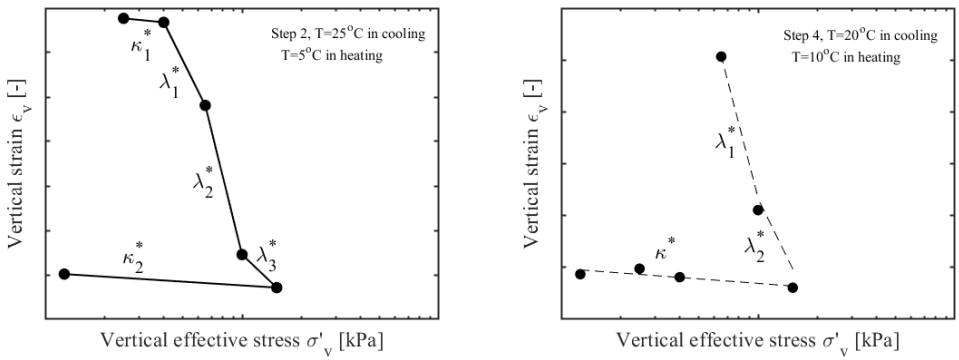

(a) Depth = 6 m (b) Depth = 9 m

Figure 4.8: Definition of the modified compression and swelling index.

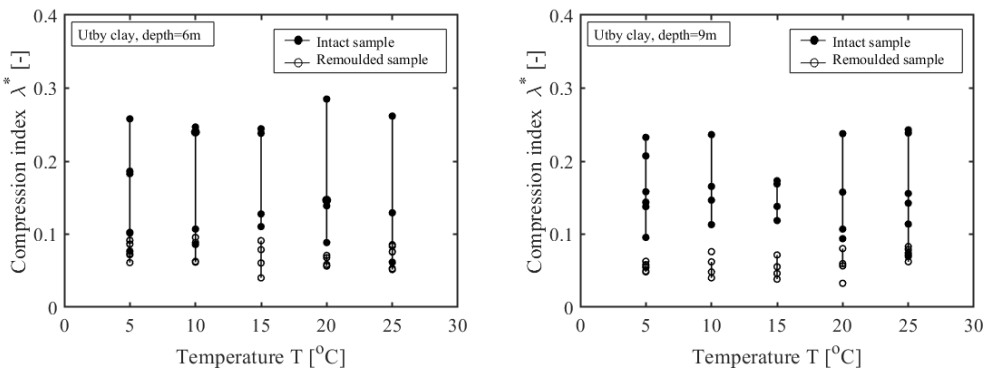

(a) Depth = 6 m (b) Depth = 9 m

Figure 4.9: Changes in the modified compression index with temperature.

laboratory at Chalmers. This can be expected because of the complex and rather unusual testing protocol used, and the challenging geological conditions in the test site.

In this context, for further analyses, λ^* and κ^* are treated as temperature-invariant, which is consistent with previous studies (Abuel-Naga, Bergado, and Lim 2007; N. Tanaka et al. 1997).

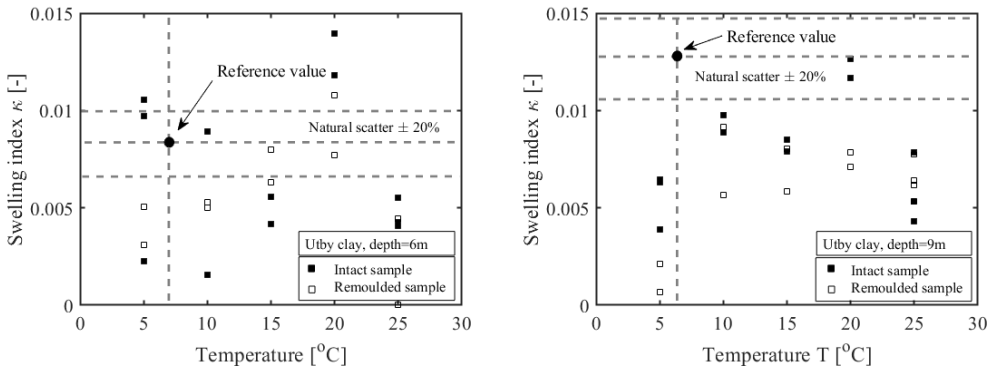

(a) Depth = 6 m (b) Depth = 9 m

Figure 4.10: Changes in the modified swelling index with temperature.

4.1.3 Hydraulic conductivity

The hydraulic conductivity k (m/s) reflects the impedance to fluid (water) flow through a porous material (Bear 1972). In clays this is related to the micro-structure of the clay. In addition, the hydraulic conductivity varies with the dynamic viscosity μ (Pa·s) of water, which is temperature-dependent (Korson et al. 1969). The dynamic viscosity of water μ decreases with increasing temperature. Hence, the hydraulic conductivity of clays might increase with heating, because the water flows more freely through the porous network with a lower dynamic viscosity. The density of water also decreases when heated above 4 °C.

At small strain magnitudes, assuming elasticity theory, the hydraulic conductivity for clays can be derived from the consolidation coefficient, evaluated from the time-void ratio curve ($e - \log t$) using the log time (Casagrande) method. The hydraulic conductivity under the same stress state is plotted in Fig. 4.11. There is no obvious trend for the changes in hydraulic conductivity as a function of temperature. The values are very small and void ratio -dependant.

On the other hand, the intrinsic permeability K (m^2) is only related to the geometry and surface properties of the clay particles. Therefore, the evolution of permeability K is

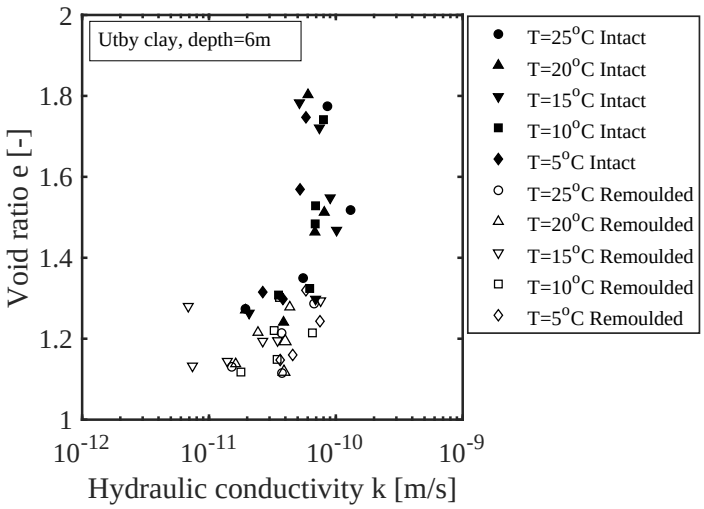

(a) Depth = 6 m

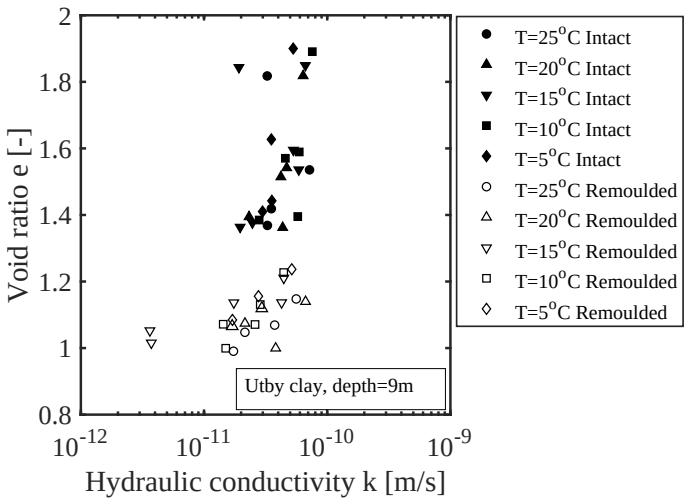

(b) Depth = 9 m

Figure 4.11: Variation of the hydraulic conductivity with temperature.

a better measure than hydraulic conductivity k to investigate the effect of temperature change on the connected pore system, as a proxy for the clay structure.

The intrinsic permeability K is calculated from the hydraulic conductivity k, the density of the pore water ρ (kg/m^3), the dynamic viscosity μ (Pa·s) of the pore water and the gravitational acceleration g_0 (m/s^2) as expressed in Eq.(4.3).

$$K = k\frac{\mu(T)}{\rho(T)g_0} \tag{4.3}$$

The density and the dynamic viscosity of water are adjusted with temperature in the calculations for intrinsic permeability K. Fig. 4.12 shows the intrinsic permeability of the intact and the remoulded samples from both depths at five temperature levels, derived from the mechanical loads step at a constant temperature. Based on Figure 4.12, just like the hydraulic conductivity, the intrinsic permeability has a stronger relation with the void ratio than the temperature for both the intact and the remoulded samples. This is consistent with previous tests on Boom clay, which is a much stiffer non-sensitive clay (Sultan et al. 2002). Clearly, the intrinsic permeability K that characterises the connected pore space where the free pore water passes through has not been influenced by the modest temperature changes (5 °C to 25 °C) investigated. The size of large macro-structural level pores between the aggregates depend more on the mechanical load (Delage and Lefebvre 1984) than the thermal load.

4.1.4 Creep rate $C_{\alpha e}$

To investigate the effect of temperature on creep rate, the value of $C_{\alpha e}$ needs to be evaluated from both mechanical and thermal loading steps. The creep rate is determined using 40 points in the tail of each consolidation curve, see Figs. 4.13(a) & 4.13(b).

The evolution of the creep rate represents the most direct effect of micro-structural changes under constant effective stress. Figure 4.14 shows the evaluated creep rate $C_{\alpha e}$ for the intact and remoulded samples, respectively, from the depths of 6 m and 9 m. The results show that the creep rate, and its susceptibility to temperature, is the highest for the intact samples at load levels around the apparent preconsolidation pressure, consistent with previous experiments on natural samples (Karlsson et al. 2016; Leroueil, Kabbaj, et al. 1985). In contrast, the semi-logarithmic creep rate is rather stable for normally consolidated remoulded samples, even though around the apparent preconsolidation pressure, which is the same as the in-situ vertical effective stress for the remoulded samples, there is a marginal increase. Consequently, there is no significant increase in creep rate due to a change in temperature for the remoulded samples. A similar trend is observed for the intact samples at high stress levels where the clay structure has

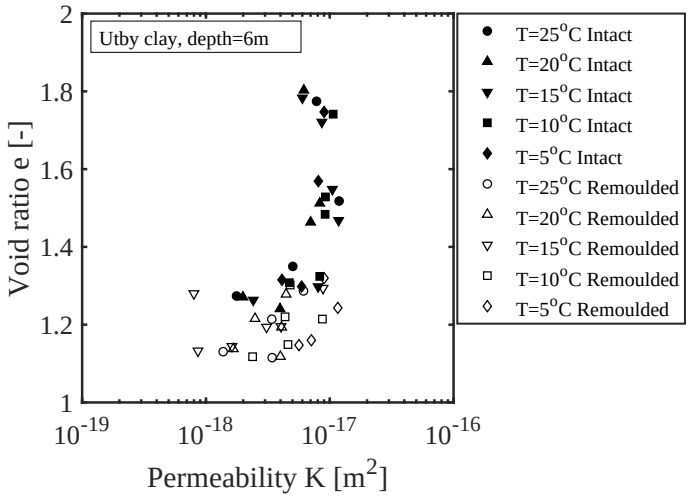

(a) Depth = 6 m

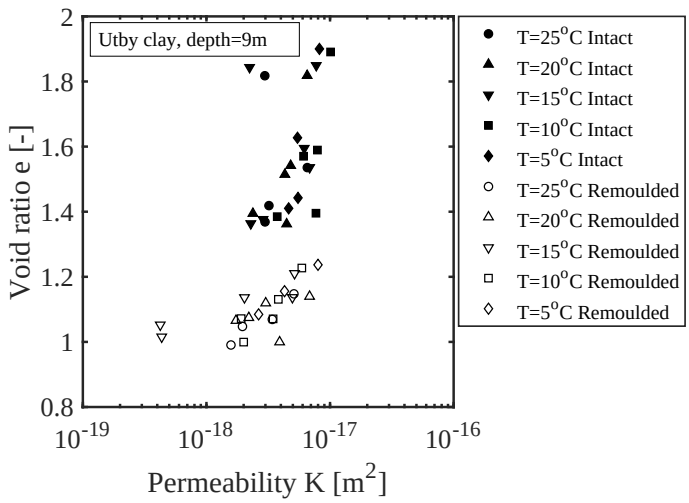

(b) Depth = 9 m

Figure 4.12: Variation of the intrinsic permeability with temperature.

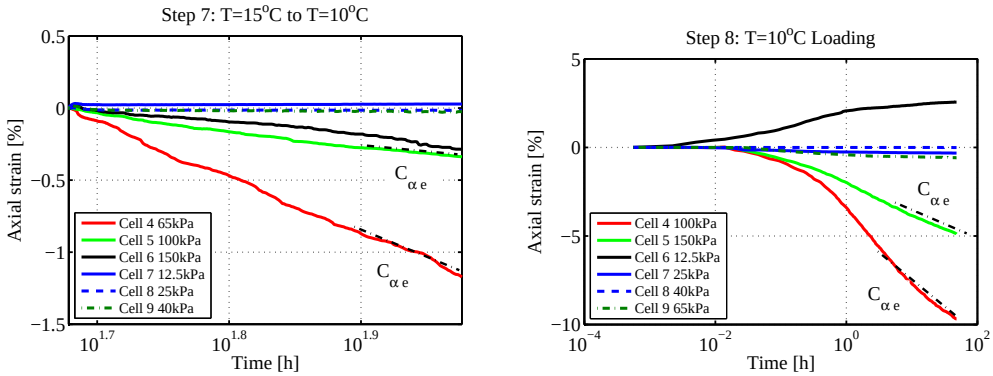

(a) Depth = 6 m (b) Depth = 9 m

Figure 4.13: Changes in creep rate with stress level under certain temperature.

already been significantly degraded.

In addition to the mechanical loading steps, there are four thermal loading steps in the test procedure. In these steps the temperature of the room is changed from one temperature to the next target temperature. The latter process takes less than four hours. Figure 4.4 shows the change in the void ratio under certain stress level for different thermal loading steps. Based on Figs. 4.4(b) and 4.4(d), it can be concluded for clay samples from both depths that the rates of void ratio change at a stress level of 100 kPa increase upon heating. This change is not as clear when the samples are subjected to cooling, as can be seen in Figs. 4.4(a) and 4.4(c). Thus, for normally consolidated natural clays, heating leads to softening of the clay (decrease in the apparent preconsolidation pressure), and the subsequent hardening tries to compensate for this softening. Unloading and reloading are also included in the test programme. As already discussed, thermal dilation is observed, when the samples are unloaded from the highest stress level to 12.5 kPa.

After the samples respond to the temperature change by deformation, they reach a new state under which the creep continues under the same effective stresses at the new temperature. The creep rate after a mechanical loading increment (solid black symbols in Fig. 4.15) is evaluated at the end of consolidation (before the light grey dashed lines in Fig. 4.4). After that the next temperature increment is applied sufficiently slowly to maintain drained conditions. Subsequently, the thermal creep rate (solid grey symbols in Fig. 4.15) is evaluated at the end of this thermal load increment. The long arrows indicate the thermal loading directions. The creep rate after the thermal loading increment is deduced from the last part of thermal loading step (from 83 to 96 hours in the time-void ratio curve in Fig. 4.4). The evaluated values for the creep rate $C_{\alpha e}$ vary considerably, i.e. >50%, for the stress level just beyond the apparent preconsolidation pressure σ'_{pc} (shown as triangles in the Figure), even with only 5 °C change in temperature.

Based on Figures 4.15(a) and 4.15(c), the creep rates in the incremental heating tests are

higher than those in the decremental cooling tests, and the creep rate tends to increase upon heating and decrease under cooling. It appears that for most stress levels the creep rate peaks between 10 °C and 15 °C before reducing at 20 °C and 25 °C. This is not an artefact of the measurement system, as the calibration indicates a linear dependency between the temperature and the strains in the system. In addition, the temperature control was stable during the test as shown in Fig. 3.7. Furthermore, this peak in the creep rate is more apparent for the samples retrieved from 9 meters depth than those from 6 meters. The latter is probably due to the larger void ratio of the deep samples. Based on the sample quality metric proposed by Lunne et al. (1997), the $\Delta e/e_0$ ratios during re-consolidation for intact clays from both 6 and 9 meters are around 5%, indicating equal amount of sample disturbance. The differences in the void ratios between the two depths are hence most likely of geological origin.

The results in Fig. 4.15 are lumped into one graph with the upper part showing the heating data and the bottom part the cooling data for each series. The changes in the creep rate around apparent preconsolidation pressure upon heating and cooling are observed over the whole studied temperature range for intact samples. In contrast, the changes in creep rates are not so obvious for the remoulded samples and the intact samples under high stress levels, as shown in Figs. 4.15(b) and 4.15(d). An explanation for the differences observed is that in the remoulded samples the sizes of the pores between the aggregates differ considerably from the intact samples, and most of the bonds are no longer present, as can be inferred from the differences in the water content between intact samples ($w > w_L$ – Table 3.1) and the remoulded samples ($w \approx w_L$). It is namely impossible to reconstitute the samples to the natural void ratio of the intact samples for sensitive clays.

When the clay samples are subjected to the same mechanical loads, the variation in creep rate under different temperatures is likely to be caused by the change in the bonds between the aggregates, or even internal irreversible changes in the aggregates, for example the change in the distance between the stacks (Brochard et al. 2017; Hansen et al. 2012) and their orientation (Jaradat et al. 2017). According to Hansen et al. (2012), heating can increase the free charges within clay stacks in a suspension, hence relating to very low effective stress levels. If creep is a process during which micro-structural water is transferred to the large voids between the aggregates, as described by Navarro and Alonso (2001), heating can also accelerate this process by changing the equilibrium in the charges and the chemical potential.

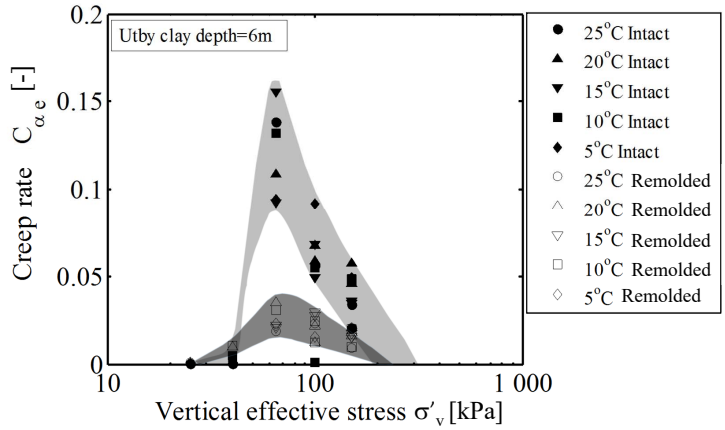

(a) Depth = 6 m

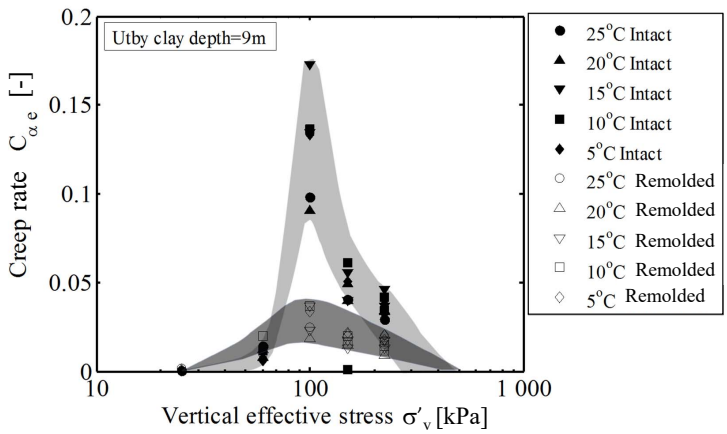

(b) Depth = 9 m

Figure 4.14: Changes in creep rate as function of stress level at given temperature.

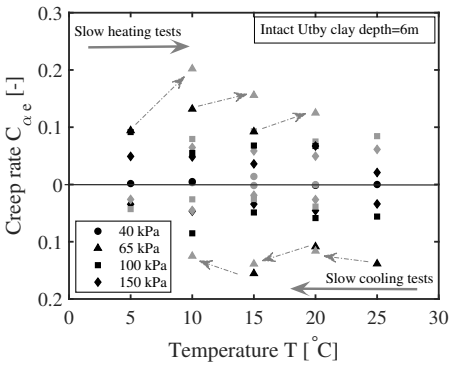

(a) Depth = 6 m Intact

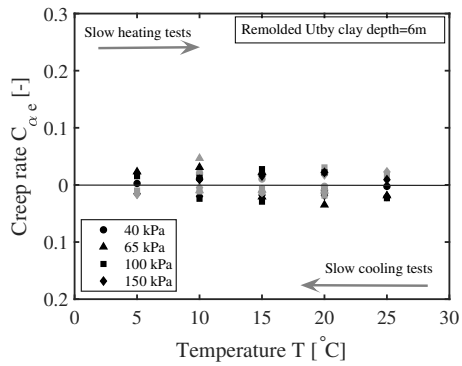

(b) Depth = 6 m Remoulded

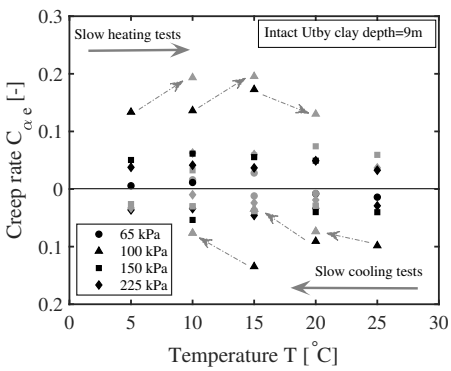

(c) Depth = 9 m Intact

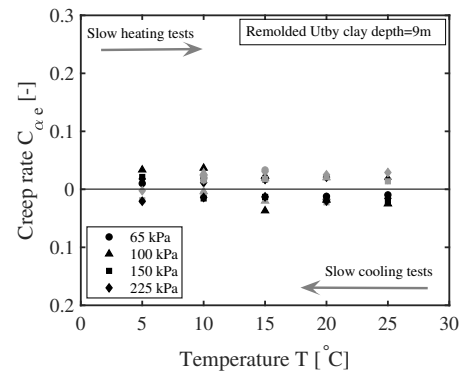

(d) Depth = 9 m Remoulded

Figure 4.15: Changes in creep rate as function of temperature at given stress level.

Apparent preconsolidation pressures σ'_{pc}

The number of data points resulting from the loading procedure is not sufficiently accurate for the evaluation of apparent preconsolidation pressure σ'_{pc}. Thus, the apparent preconsolidation pressures obtained from CRS tests on the samples from the same test site conducted by Karlsson et al. (2016) are utilised in the numerical analyses.

4.2 Numerical analyses of experimental results

Further numerical analysis is required to separate the effects of thermal loading and mechanical loading that are present in the data set presented in Section 4.1. This allows to quantify the magnitude of the change in creep rate as function of thermal loading. The multi-physics framework combined with the Creep-SCLAY1S model presented in Section 3.3 is used. Although the model is temperature-independent, the effective stress -dependent creep should be able to adequately capture the measured response, given the temperature changes are modest, provided a fully coupled THM (Thermo-Hydro-Mechanical) formulation is used. In the following, a fully-coupled boundary value level THM model is used to capture the change in effective stress due to the generation and dissipation of excess pore pressures caused by the combination of mechanical loading and temperature changes.

4.2.1 Model parameter calibration

The Creep-SCLAY1S requires values for a number of model parameters, as well as initial values for three state variables. These need to be derived from, and calibrated against, oedometer and triaxial tests. An independent set of experiments on clay samples retrieved from the depths of 6 and 9 meters has been modelled on the boundary value level, in order to calibrate the the derived model parameter set. The experimental data from the tests performed on samples at 7 °C reference temperature are used for the model calibration, with the results plotted in Fig. 4.16 together with the model simulations demonstrating a good match for this particular stress path.

The modified intrinsic compression index $\lambda_i^* = \Delta\varepsilon/\Delta \ln \sigma$, is obtained from the virgin compression parts of stress-strain curves of remoulded samples by curve fitting. The modified swelling index κ is obtained from the unloading parts of reference tests on intact samples $\kappa^* = \Delta\varepsilon/\Delta \ln \sigma$.

The model parameters for the anisotropy α_{K0}, ω and ω_d are evaluated and derived from using the estimated slope of the critical state line in compression M_c of the clay samples from the same site where the test samples were sampled, following guidance in Gras et al. (2017) and Gras et al. (2018). The value of M_c =1.4 was derived from a

set of anisotropically consolidated undrained triaxial tests in compression and extension by Karlsson et al. (2016). The latter (i.e. triaxial extension tests) are useful for the calibration of ω value, but as during oedometer tests no significant evolution of anisotropy is expected, the simulations are insensitive for the value chosen.

Because of the sample disturbance during sampling and transportation varies between the samples used for the thermal testing series and the reference tests, the initial amount of bonding χ_0 is obtained together with the structural parameters ξ_d and ξ by curve fitting the compression curves of the intact samples.

The parameter related to rate-dependency μ_i^* is obtained from final part of time-displacement curves for the remoulded samples as $\mu_i^* = \Delta\varepsilon / \ln t$, and the reference time τ is assumed as 1 day, corresponding to the duration of the load increment (1 day) used in deriving the values for the apparent preconsolidation pressure σ'_{pc} in Table 4.1 in the reference tests.

The final set of model parameters obtained from by the calibration is presented in Table 4.1. The initial void ratio e_0 is only included to be able to plot the changes in void ratio for in the simulations (so it is strictly speaking not a model parameter). The mineralogy of the clay from these two depths is largely similar, which is reflected in the almost identical intrinsic parameters at the two depths (6 m and 9 m).

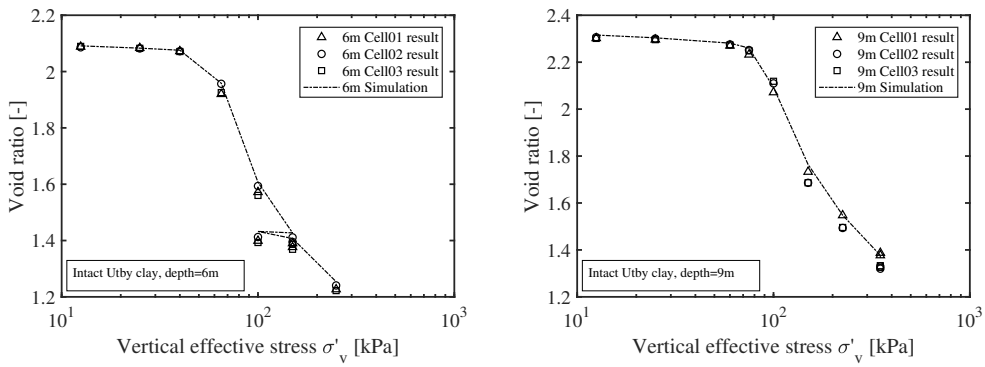

(a) Depth = 6 m

(b) Depth = 9 m

Figure 4.16: Parameters calibration for Creep-SCLAY1S.

The numerical framework used for the simulations has been introduced in Section 3.3. In order to simulate the mixed mechanical and thermal loading paths for both intact and remoulded samples, hydraulic and thermal properties are needed. The thermal properties, including the thermal conductivity λ_T, the specific heat capacity C_v for both intact and remoulded samples and the thermal properties of the pore water are summarised in Table. 4.2. The Young's modulus is needed in COMSOL analyses to create the initial stress state, and is hence not related to the constitutive model, unlike the Poisson's ratio. The

Table 4.1: Creep-SCLAY1S parameters for Utby clay.

Depth[m]	e_0	λ_i^*	κ^*	μ_i^*	σ'_{pc} [kPa]	σ'_{vo} [kPa]
6 (Intact)	1.95	0.0862	0.0083	0.004	54	45
6 (Remoulded)	1.49	0.0862	0.0083	0.004	45	45
9 (Intact)	2.15	0.08	0.013	0.004	70	60
9 (Remoulded)	1.37	0.08	0.013	0.004	60	60
Depth[m]	α_0	ω	ω_d	χ_0	ξ_d	ξ
6 (Intact)	0.5	40	0.9	6	12	0.42
6 (Remoulded)	0.5	40	0.9	0	-	-
9 (Intact)	0.5	40	0.9	14	11	0.36
9 (Remoulded)	0.5	40	0.9	0	-	-

Table 4.2: Additional parameters for the model simulations.

Parameter	Symbol	6 m	9 m	Units
Density	ρ	1589	1565	kg/m^3
Porosity	n	0.66	0.68	-
Young's modulus	E	5×10^5	5×10^5	Pa
Poisson's ratio	ν	0.25	0.25	-
Permeability	k	5×10^{-18}	5×10^{-18}	m^2
Dynamic viscosity	μ	1×10^{-9}	1×10^{-9}	Pa·s
Thermal conductivity	λ_T	1.12	1.12	W/(m·K)
Heat capacity	C_p	3300	3300	J/(kg·K)
Thermal expansion	α_T	3.2×10^{-5}	3.2×10^{-5}	1/K

porosity is used in combination with the intrinsic permeability to account for the changes in hydraulic conductivity during the analyses.

4.2.2 Modelling overview

The results from six oedometer cells with a combination of mechanical and thermal loading, are selected out of a total of 48 tests for further comparison. For reliable comparisons, all of these started at a similar void ratio. Three tests for both intact and remoulded samples from each depth are simulated for heating and cooling paths: paths O_1, O_2, and O_3 in Fig. 4.17 correspond to Column O_1, O_2, and O_3 in Table. 4.3. The loading steps vary for the two depths considered according to the initial in-situ stress levels, and the initialisation of the apparent preconsolidation pressures.

The samples are first loaded to the in-situ vertical effective stress level, and subsequently loaded using the individual load steps as shown in Table 4.3. The temperature in the heating and cooling tests, and the stress levels for different cells is visualised in Fig. 4.17. For each loading path, the clay samples are loaded beyond their respective apparent preconsolidation pressures at different temperatures. In loading path O_1, for example, for both static heating and cooling tests, the samples are loaded beyond the apparent preconsolidation pressure at T_3, which is 15 °C. For loading path O_2 and O_3, the samples are loaded under T_2 and T_1, respectively. The difference of T_2 and T_1 between static heating and cooling tests are 10 °C and 20 °C, respectively.

A total of 24 simulations have been performed, 12 for remoulded samples and 12 for intact samples. The simulation results are divided into three groups:

- Mixed loading conditions for remoulded samples
- Mixed loading conditions for intact samples
- Thermal loading under constant mechanical load

Due to the similarity of the experimental and numerical results, only one data set for the remoulded samples consolidated to the original in-situ stress state is elaborated.

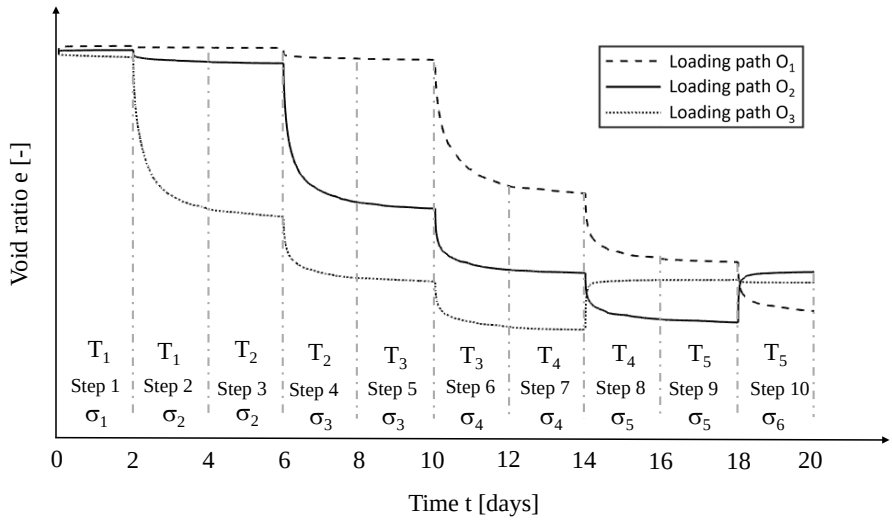

Figure 4.17: Different loading paths selected for numerical simulations.

Table 4.3: Selected tests for numerical simulations.

Step	Temperature (°C)			Load steps 6m (kPa)			Load steps 9m (kPa)		
	In heating	T	In cooling	O_1 Cell 04	O_2 Cell 05	O_3 Cell 06	O_1 Cell 10	O_2 Cell 11	O_3 Cell 12
1	5	T_1	25	12.5	25	40	12.5	25	60
2	5	T_1	25	25	40	65	25	60	100
3	10	T_2	20	25	40	65	25	60	100
4	10	T_2	20	40	65	100	60	100	150
5	15	T_3	15	40	65	100	60	100	150
6	15	T_3	15	65	100	150	100	150	225
7	20	T_4	10	65	100	150	100	150	225
8	20	T_4	10	100	150	12.5	150	225	12.5
9	25	T_5	5	100	150	12.5	150	225	12.5
10	25	T_5	5	150	12.5	25	225	12.5	25

4.2.3 Mixed loading conditions for remoulded samples

The structure in the remoulded clay samples differs from the intact samples. As demonstrated in Section 4.1, the (thermal) softening is less pronounced. The simulations of remoulded samples from two different depths with loading path O_1 are compared with experimental results (△ for heating and ◯ for cooling) in Figs. 4.18 & 4.19.

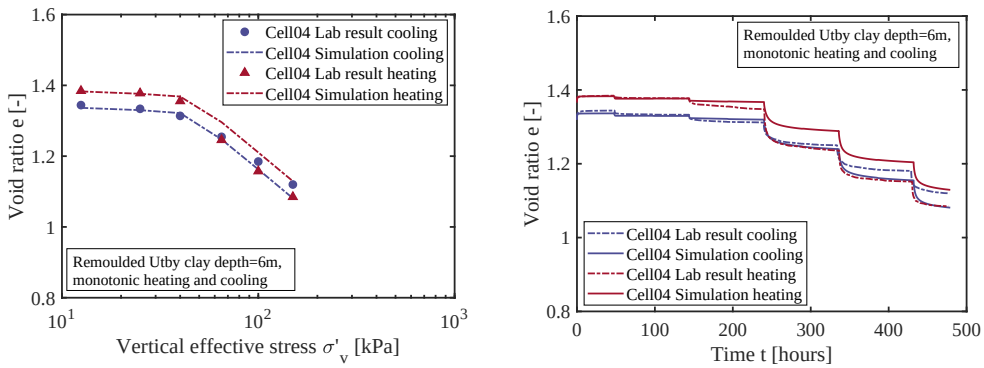

(a) Compression curve (b) Consolidaiton curve

Figure 4.18: Remoulded sample from the depth of 6 m, loading path O_1.

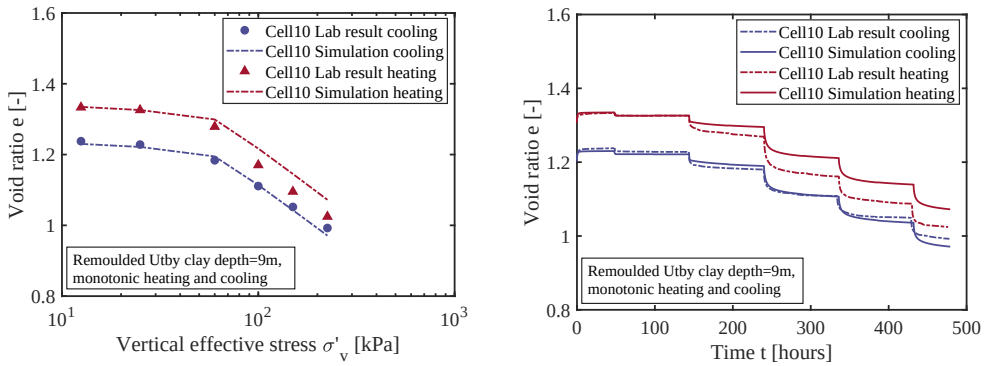

(a) Compression curve (b) Cosoliation curve

Figure 4.19: Remoulded sample from the depth of 9 m, loading path O_1.

The multi-physics simulations with the temperature-invariant creep model (creep-SCLAY1S) captures the general response of the remoulded clays rather well, both for the compression curves (Figs. 4.18(a) & 4.19(a)) and the time-void ratio curves (Figs. 4.18(b) & 4.19(b)). The compression curves are plotted with the data points collected from the end of the mechanical load, before changing the temperature to the next target temperature. As

a result, the loading step is still influenced by the temperature change and mechanical loading of the previous steps.

The match of the simulations with experimental data is somewhat better for the static cooling tests than the static heating tests. Due to the sample preparation procedure, where one series of samples has been consolidated one month longer than the other (hence experiencing more creep), the cooling tests are performed on the samples with smaller initial void ratio. Differences remaining between match with experiment and simulations for the static heating and cooling tests are perhaps attributed to the differences in preparation time.

4.2.4 Mixed loading conditions for intact samples

The structure in the intact clay samples make them more sensitive to mechanical loading and temperature change (Section 4.1). The simulations of intact samples from 6 meter depth for loading path O_1, O_2 and O_3 are compared with experimental results ($\triangle$ for heating and $\bigcirc$ for cooling) in Figs. 4.20, 4.21 & 4.22. In the simulations for the samples from 6 meters, the initial amount of bonding is assumed to be $\chi_0 = 6$, which reflects a moderately sensitive natural clay.

Similarly to the simulation results for the remoulded samples, the multi-physics simulations with the temperature-invariant creep model already captures the general behaviour satisfactorily, both for the compression curves (Figs. 4.20(a), 4.21(a) & 4.22(a)) and the time-void ratio curves (Figs. 4.20(b), 4.21(b) & 4.22(b)).

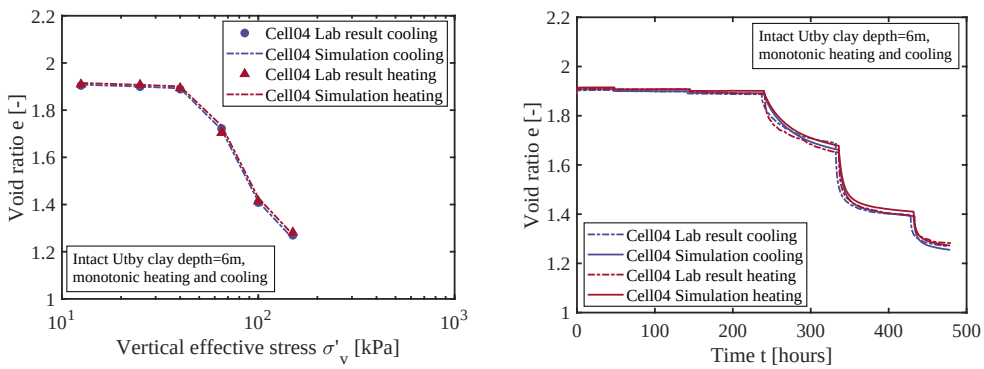

(a) Compression curve

(b) Cosoliation curve

Figure 4.20: Intact sample from the depth of 6 m Cell 04, loading path O_1.

However, for loading path O_2, where the samples are loaded beyond the apparent pre-consolidation pressure under T_2 (20°C in static cooling and 10 °C in static heating), the differences between static heating and cooling start to appear. The change in the void

ratio with an identical load increment is larger under higher temperature as shown in Fig. 4.21(a). This difference remains when the clay samples are thermally loaded from 20°C to 15°C in static cooling tests, and from 10°C to 15°C in static cooling tests.

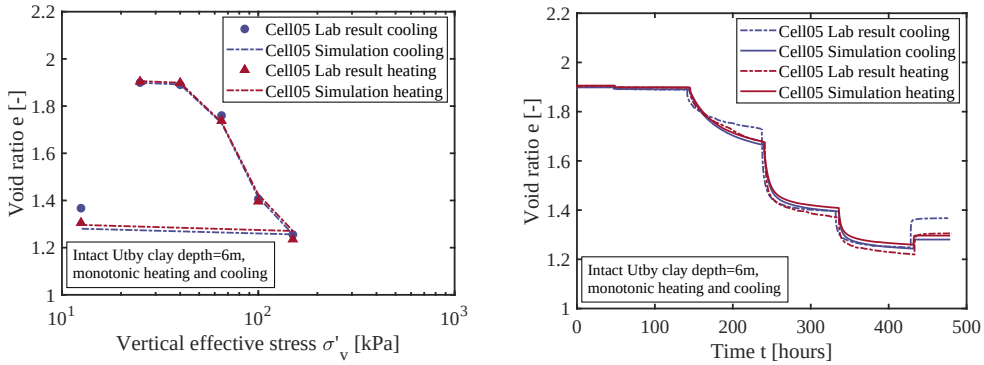

(a) Compression curve

(b) Cosoliation curve

Figure 4.21: Intact sample from the depth of 6m Cell05, loading path O_2.

For loading O_3, the samples are mechanically loaded under temperatures T_1 (25°C in static cooling and 5 °C in static heating). The differences between the simulation and the data is most pronounced for loading path O_3 as shown in Fig. 4.22.

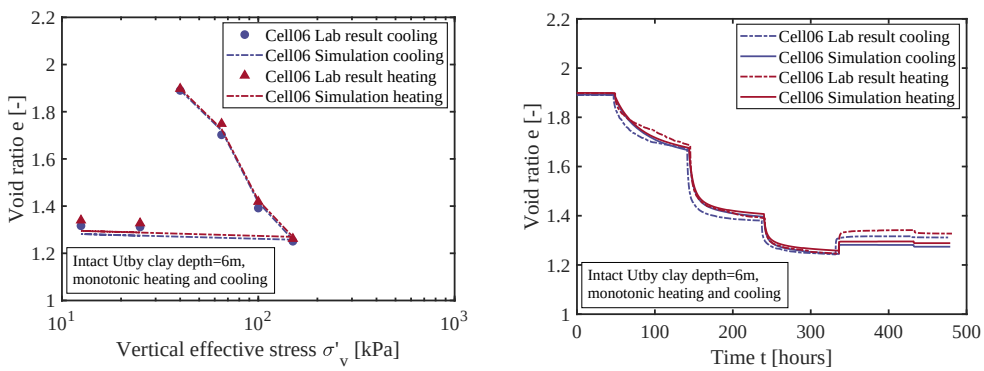

(a) Compression curve

(b) Cosoliation curve

Figure 4.22: Intact sample from the depth of 6 m Cell 06, loading path O_3.

Similarly to the simulations on intact samples from a depth of 6 meters, the samples from 9 meters are simulated for loading paths O_1, O_2 and O_3. The results of the numerical simulations are compared with the experimental results (△ for heating and ◯ for cooling) in Figs. 4.23, 4.24 & 4.25. For the samples from 9 meters, the initial structure parameter

is $\chi_0 = 14$, which reflects larger sensitivity than the clay from 6 meters depth. The larger sensitivity leads to increased differences between the simulations and experimental data compared to the results for 6 meters depth.

Nonetheless, the multi-physics simulations with the temperature-invariant creep model reproduce the general behaviour surprisingly well as a function of the load applied, Figs. 4.23(a), 4.24(a) & 4.25(a)) and the time (Figs. 4.23(b), 4.24(b) & 4.25(b)).

For loading path O_2, where the samples are loaded beyond the apparent preconsolidation pressure under T_2 (20°C in static cooling and 10 °C in static heating), the differences between the static heating and cooling are even more pronounced than for the samples from 6 m (Fig. 4.21(a), due to the larger initial sensitivity (structure parameter $\chi_{0;9m} = 14$ instead of $\chi_{0;6m} = 6$). Loading path O_3, where the samples are mechanically loaded under temperatures T_1 (25°C in static cooling and 5 °C in static heating), similar increases in the discrepancies between the simulation and data are shown in Fig. 4.25.

Overall, the simulation results for loading path O_1 are closest to the experimental data of all the simulations, regardless of the amount of initial structure ($\chi_{0;9m} = 14$, $\chi_{0;6m} = 6$ and $\chi_{0;remoulded} = 0$). This indicates that the multi-physics modelling with temperature-invariant creep model is best suited for conditions where the effects of structure, and its temperature sensitivity, is minor.

A closer study of the behaviour of the intact clay samples from the 9 meters depth, which are most sensitive, in loading paths O_2 and O_3 reveal that the model inaccuracies are largest when the load steps pass the respective apparent preconsolidation pressures, as shown in compression curves(Fig. 4.23(a), 4.24(a) & 4.25(a)). This is corroborated by the time-void ratio plots (Fig. 4.23(b), 4.24(b) & 4.25(b)). The intact clay samples for both heating and cooling tests have a similar void ratio ($e_0 \approx 2$) at the start of the test. The only difference between the static heating and cooling tests is that the actual temperature at which the mechanical load step passes the apparent preconsolidation pressure is different. The changes in the void ratio developed during this step is larger for the cooling tests than the heating tests.

The difference in the change of void ratio between cooling and heating paths seems to be temperature-dependent. For example, when the difference in temperature increases from 0 °C (Fig. 4.23(a)) to 10 °C (Fig. 4.24(a)) and finally to 20 °C (Fig. 4.25(a)), the difference in the change in the void ratio increases proportionally. An increment in temperature causes decrement in stiffness. The latter most probably is linked to a reduction in the apparent preconsolidation pressure. This confirms the prior observations that the apparent preconsolidation pressure is changing as a function of temperature.

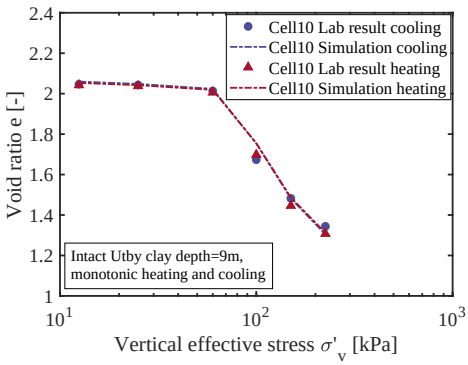

(a) Compression curve

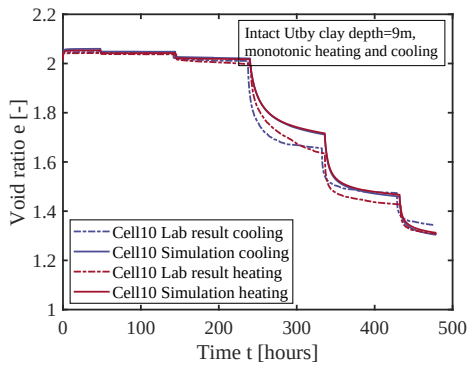

(b) Cosoliation curve

Figure 4.23: Intact sample from the depth of 9 m Cell 10, loading path O_1.

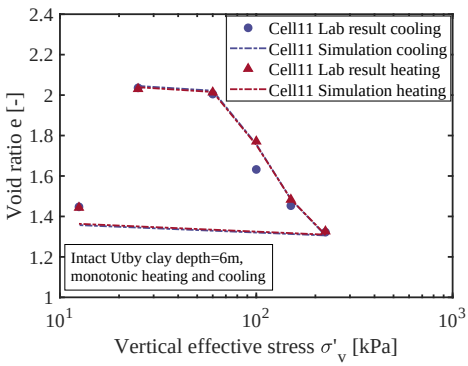

(a) Compression curve

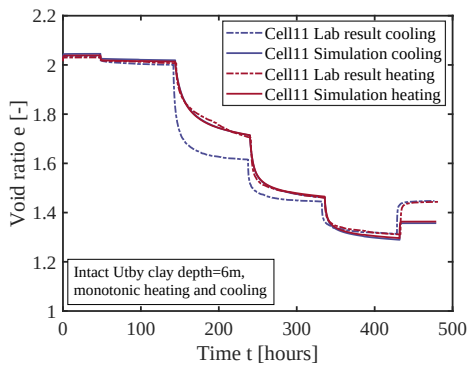

(b) Cosoliation curve

Figure 4.24: Intact sample from the depth of 9 m Cell 11, loading path O_2.

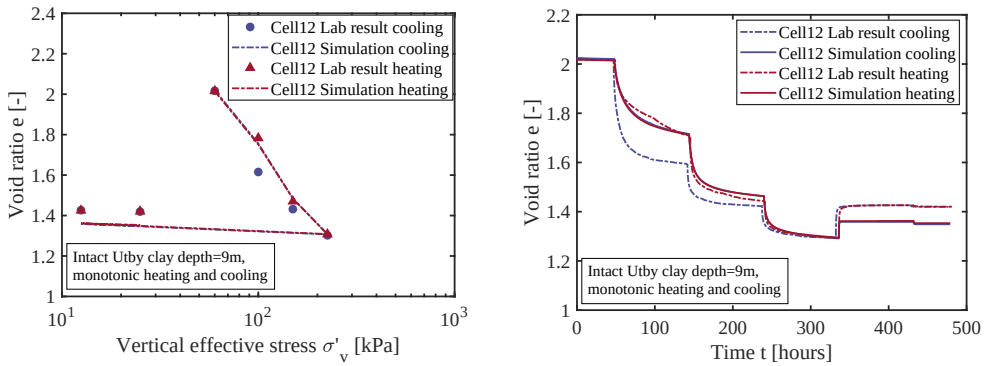

(a) Compression curve

(b) Cosoliation curve

Figure 4.25: Intact sample from the depth of 9 m Cell 12, loading path O_3.

4.2.5 Thermal loading under constant mechanical load

As observed in the mixed thermo-mechanical loading scenarios, the largest temperature sensitivity of the clays is around the apparent preconsolidation pressure. A special case that the experimental programme allows to investigate, is the clay behaviour during thermal loading under constant mechanical load, this is the condition for which the inaccuracies of the multi-physics numerical simulation with temperature-invariant creep model is the largest.

Differences occur when the samples are subjected to identical stress histories, and subsequently loaded with different temperature increments. The simulations are performed for experimental data for both heating and cooling paths. The time-void ratio curves for the results on the intact and remoulded clay samples from 6 and 9 meters depth are plotted in Figs. 4.26 & 4.27. The performance of the model is evaluated for the following cases: (i) the effect of the initial structure on the temperature sensitivity, (ii) the difference in heating and cooling paths (15 °C to 20 °C and 15 °C to 10 °C).

In these Figures, the change in void ratio is corrected with the initial void ratio of the corresponding step. The change in void ratio Δe upon temperature change shows clearly that in the laboratory tests from an identical temperature, heating a sample leads to larger change in void ratio than cooling the sample, for a moderate temperature change of ≈ 5°C. The temperature-invariant model is unable to capture this behaviour , as shown in Figure 4.26(a), 4.27(a), 4.26(b) & 4.26(b). As discussed previously, these discrepancies are of most concern for temperature change around the apparent preconsolidation pressure for samples with natural structure. Therefore, in the next Chapter a new version of the Creep-SCLAY1S model is developed, with a temperature- and structure-dependent apparent preconsolidation pressure. This potentially will improve the modelling of rate- and temperature-dependent response of natural sensitive clays.

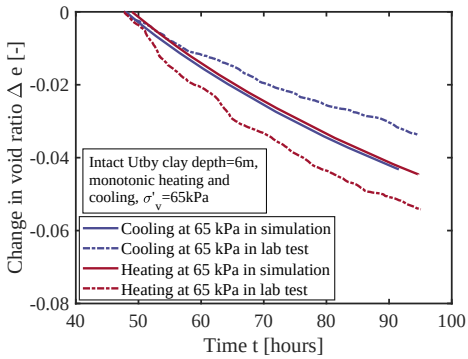

(a) Intact samples

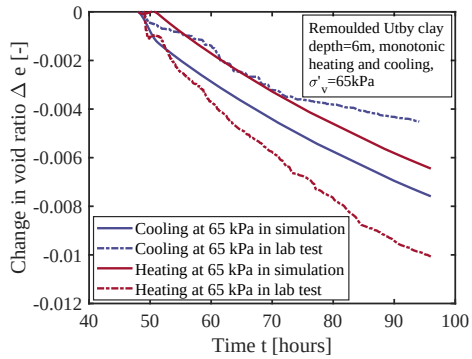

(b) Remoulded samples

Figure 4.26: Change in void ratio under thermal load steps for samples from a depth of 6 m.

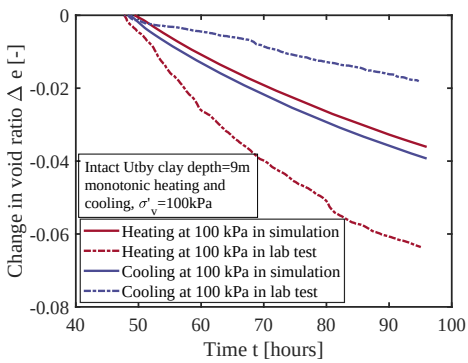

(a) Intact samples

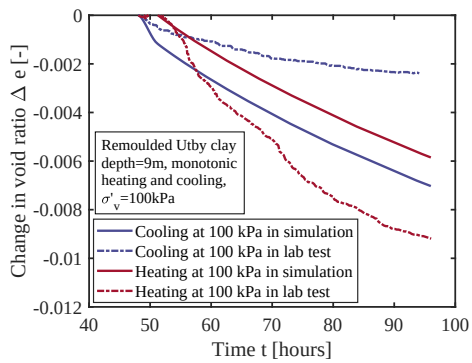

(b) Remoulded samples

Figure 4.27: Change in void ratio under thermal load steps for samples from a depth of 9 m.

5 Thermal modelling of sensitive clays

In this Chapter, the creep model Creep-SCLAY1S introduced in Section 3.3 is modified based on the laboratory tests and supplementary numerical simulations, to account for the thermal effects on the sensitive clay presented in Chapter 4. The main new mechanism observed in the test data that needs to be added to the constitutive model is the bonding-dependent thermal softening and hardening of the natural sensitive clay.

5.1 Thermal dependency of apparent preconsolidation pressure

The test procedure used multiple samples that are tested simultaneously in a comprehensive loading scheme. As a result, the reliable evaluation of the apparent preconsolidation pressure as a function of temperature loading history, as required in the model development, is complex. This apparent preconsolidation pressure, however, can be evaluated with high precision by introducing a non-linear fit from the constitutive model. This is far from trivial, as in these back-analyses the data is fitted with fully coupled multi-physics analyses at boundary value level (similar to Section 4.2).

There are two steps in the back-analyses: firstly the temperature-invariant model is fitted to the experimental data by changing the apparent preconsolidation pressure, and secondly the model is refined to include temperature effects.

The experimental data is replotted in Figure 5.1 by combining the time-void ratio curves of equal mechanical loading steps (σ_3 to σ_4) under different temperatures. The steps are chosen in such way that the stress levels on the samples exceed their respective apparent preconsolidation pressures, so that the magnitude of the apparent preconsolidation pressure under different temperatures can be evaluated. Under the same increment of mechanical load, the change in void ratio differs at different temperatures. In Fig. 5.1, the bolder the lines, the higher is the temperature for the presented void ratio-time curves. For an equal load increment, a larger void ratio decrement is observed at higher ambient temperature. This trend is not as evident for the clay samples from 6 meters depth (Fig. 5.1(a)), yet is in agreement with previous findings for sensitive clay (Moritz 1995).

As discussed in Chapter 4, the initial amount of natural bonding has a significant effect on the emerging creep rate. The clay samples from 6 meters depth ($\chi_0 = 6$) have a lower degree of initial natural bonding than the samples retrieved from the depth of 9 meters ($\chi_0 = 14$). The material response in the loading steps with largest temperature-dependency (Fig. 4.26 and Fig. 4.27), could be fitted with relatively ease using the temperature-invariant model (Section 3.3) by changing the apparent preconsolidation pressure.

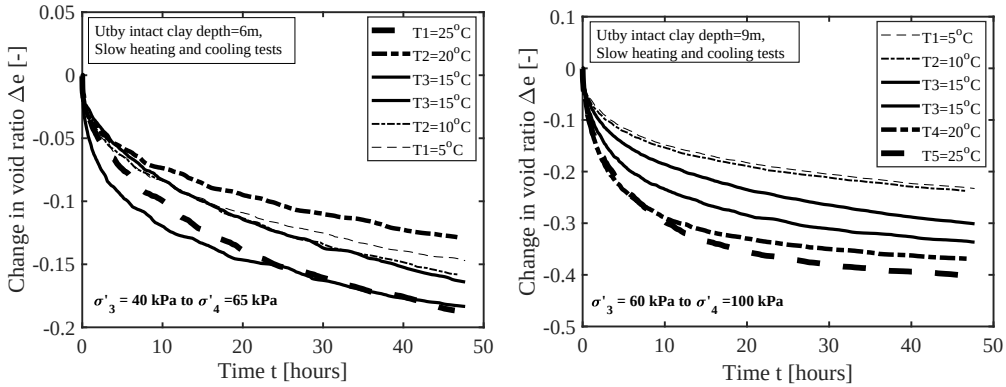

(a) Depth = 6 m (b) Depth = 9 m

Figure 5.1: Change in void ratio when loading beyond the apparent preconsolidation pressure.

A temperature isotach is a convenient way to describe the effect of temperature on the apparent preconsolidation pressure. Figure 5.2 sketches the idealised mechanism of the temperature isotachs for normal compression by plotting the the mean effective stress against volumetric strain. In this generalisation, the modified compression and swelling index are considered to be temperature-independent, which is reasonable assumption for the test data obtained in this work.

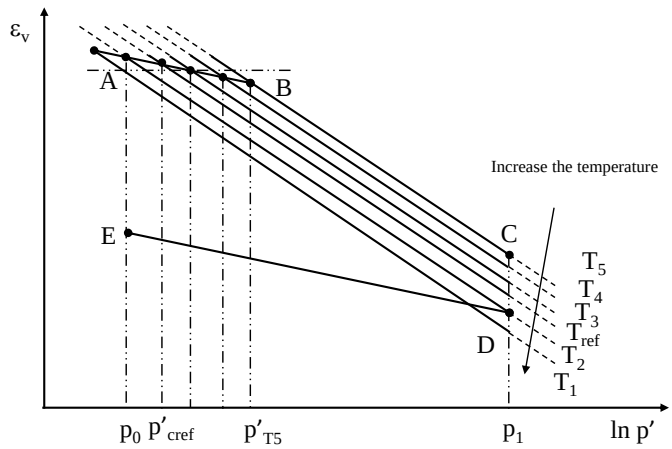

Figure 5.2: Sketch for isotropic compression under different temperatures.

A clay sample is subjected to a stress level p'_0, which is smaller than the apparent preconsolidation pressure at reference temperature p'_{cref} corresponding to the reference temperature T_{ref} ($T_{ref} = 7°C$ in this work), i.e., point A in Fig. 5.2. On the other

hand, if the temperature in the sample is initially lower than T_{ref}, for example T_5, a smaller change in void ratio change is expected for a load step with equal magnitude ($\Delta p' = p'_1 - p'_0$), and the compression line will reach to Point C instead of Point D. The increment in volumetric strain $\Delta\varepsilon_v$ to reach Point C can be expressed as Eq. 5.1.

$$\Delta\varepsilon_v = \varepsilon_{v;C} - \varepsilon_{v;A} = \kappa^* \ln\left(\frac{p'_{T5}}{p'_0}\right) + \lambda^* \ln\left(\frac{p'_1}{p'_{T5}}\right) \tag{5.1}$$

The increment in volumetric strain can be decomposed into a temperature-independent part and temperature-dependent part (Eqs. 5.2 and 5.3):

$$\Delta\varepsilon_v = \kappa^* \ln\left(\frac{p'_{T5}}{p'_0}\right) + \lambda^* \ln\left(\frac{p'_1}{p'_{T5}}\right) = \kappa^* \ln\left(\frac{p'_{T5}}{p'_0}\frac{p'_1}{p'_{T5}}\frac{p'_{T5}}{p'_1}\right) + \lambda^* \ln\left(\frac{p'_1}{p'_{T5}}\right) \tag{5.2}$$

$$\Delta\varepsilon_v = \kappa^* \ln\left(\frac{p'_1}{p'_0}\right) + (\lambda^* - \kappa^*) \ln\left(\frac{p'_1}{p'_{T5}}\right) \tag{5.3}$$

In Eq. 5.3, with constant p'_0 and p'_1, the only parameter that is temperature-dependent is the apparent preconsolidation pressure. For this example, the original preconsolidation pressure p'_{Tref} at reference temperature T_{ref}, changed to the new apparent preconsolidation pressure at T_5 which here is denoted with p'_{T5}.

In conclusion, the observed differences in the change in void ratio at different ambient temperatures as plotted in Fig.5.1 relate only to the apparent preconsolidation pressure under different temperatures. Therefore, the temperature-invariant constitutive model is fitted to the experimental data available at different temperatures by changing the apparent preconsolidation pressure. The results of these extensive back-analyses are summarised in Fig. 5.3, where the normalised temperature T/T_{ref} is plotted against the normalised apparent preconsolidation pressure p'_T/p'_{Tref}. The reference apparent preconsolidation pressure corresponds p'_{Tref} to a reference temperature T_{ref} of 7 °C. The data is divided into three data sets representing different degrees of initial bonding.

Using the back-analysed data, the following function for the temperature-dependency of the apparent preconsolidation pressure is proposed (Eq. 5.4):

$$\frac{p'_T}{p'_{Tref}} = \left(\frac{T}{T_{ref}}\right)^{-\beta_T} \tag{5.4}$$

where the β_T is the only additional model parameter required that can readily be evaluated from the experimental data. For a proper fit of β_T, a minimum of 3 incremental loading oedometer tests need to be performed at different temperatures, spanning the temperature range of interest. In Eq. 5.4 p'_T decreases upon heating, thus $\beta_T > 0$. It is impossible

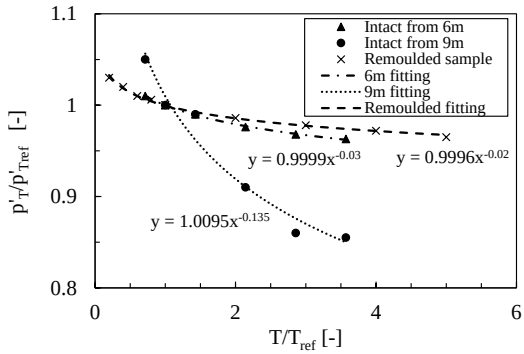

Figure 5.3: Temperature dependency of the apparent preconsolidation pressure for samples with different amounts of bonding.

to fit a unique β_T for all data sets, which have different degree of initial bonding. As a result, the amount of initial bonding in the model represented by parameter χ_0, needs to be explicitly considered. The temperature-dependency β_T increases with increasing amount of bonding χ_0. This effect is illustrated by plotting the initial amount of bonding χ_0 against β_T in Fig. 5.4. Therefore a new relation $\beta_T(\chi)$ is proposed to include state parameter χ in the definition of β_T. A linear and a exponential function are the most suitable functions that relate β_T and χ_0 (Eq. 5.5 & 5.6), because of the limitation in the data set (only three points $\chi_0 = 0, 6, \text{and} 14$).

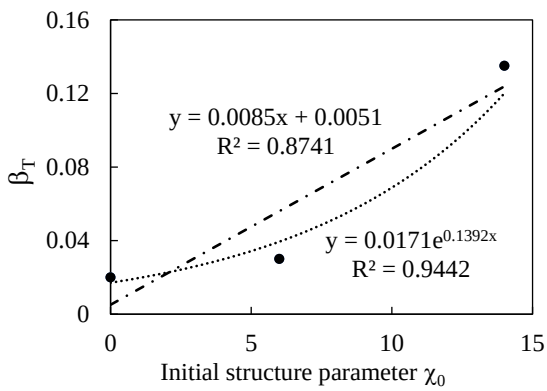

Figure 5.4: Determination of parameters a and b for thermal dependency.

$$\beta_T = ae^{b\chi} \tag{5.5}$$

$$\beta_T = a\chi + b \tag{5.6}$$

where a and b are the model parameters that are required by the linear and the exponential relation. The value for parameters a and b are obtained from the curve fitting, as shown in Fig. 5.4. Thus, Eqs. 5.5 & 5.6 can be explicitly expressed with Eqs. 5.7 & 5.8.

$$\beta_T = ae^{b\chi} = 0.0171e^{0.1393\chi_0} \tag{5.7}$$

$$\beta_T = a\chi + b = 0.0085\chi + 0.0051 \tag{5.8}$$

The two alternatives (Eq. 5.7 and Eq. 5.8) are further tested for a range of χ-values and plotted in Fig. 5.5. The largest value tested is χ =40, which represents a reasonable upper bound for the sensitive clay considered here. For the range of χ tested, the linear equation (Eq. 5.8) provides the most realistic extrapolation, i.e. at large value of χ, the material is not completely softened by a mild increase in temperature. Furthermore, at a temperature lower than the reference temperature, the apparent preconsolidation pressure is not increasing to infinity, as predicted by the exponental relationship.

Therefore, Eq. 5.4 and Eq. 5.7 are combined to Eq. 5.9, and subsequently used in the proposed modification of the temperature-invariant model.

$$\frac{p'_T}{p'_{Tref}} = \left(\frac{T}{T_{ref}}\right)^{-(a\chi+b)} \tag{5.9}$$

5.2 Creep-SCLAY1ST for thermal modelling of sensitive clays

The elastic strains under combined thermo-mechanical loads is composed of two parts: an elastic mechanical (volumetric and shear) strain and a thermal expansion of the clay particles (in drained condition). The total elastic strain can be calculated using Eq. 5.10, where α_T is the thermal expansion coefficient for clay minerals.

$$\dot{\varepsilon}^e_{TMij} = \frac{1}{2G}\dot{s}_{ij} + \frac{1}{3K}\dot{p}\delta_{ij} + \alpha_T\dot{T}\delta_{ij} \tag{5.10}$$

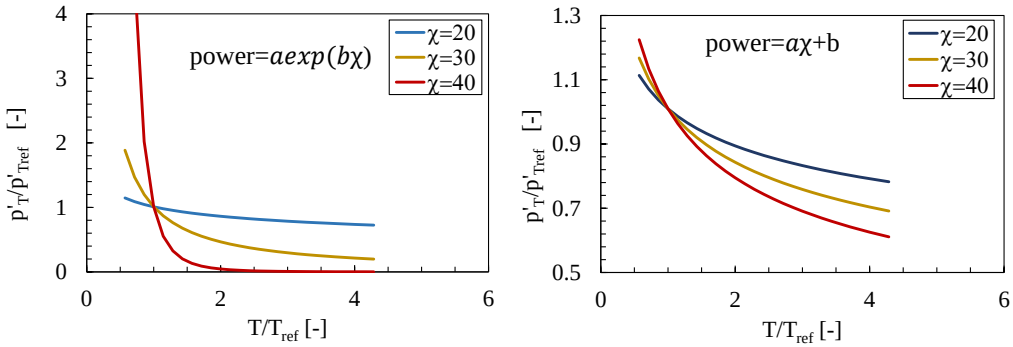

(a) Prediction1 (b) Prediction2

Figure 5.5: Predictions with the two power relationships as a function of the amount of bonding.

When calculating the viscoplastic strain of clay, the relative position of the current stress state from the reference surface need to be evaluated as described in Section 3.3. The current stress state can be expressed by one point (p', q) in the $p' - q$ figure as illustrated in Fig. 5.6. The equivalent stress p'^{eq} can be calculated using Eq. 3.7, and the current stress surface (labelled as p'^{eq} in Fig. 5.6) can be expressed with Eq. 3.8 as discussed in Section 3.3. In addition, the original reference surface (labelled as p'^{eq}_{Tref} in Fig. 5.6) changes with the temperature, based on the the ratio between the current temperature and the reference temperature T/T_{ref}, to a new reference surface labelled as p'^{eq}_{T} using Eq. 5.9.

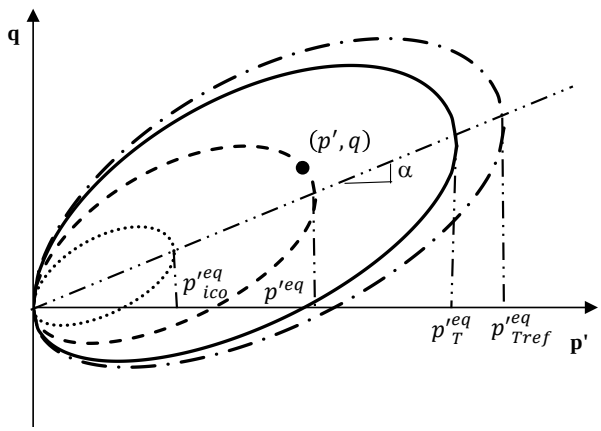

Figure 5.6: Stress state and reference surface

Assuming an associated flow rule, the viscoplastic strain increment $\dot{\varepsilon}^{vp}_{ij}$ can be calculated

using Eq. 5.11 after the determination of the new reference surface f_{Tref}.

$$\dot{\epsilon}_{ij}^{vp} = \dot{\Lambda} \left(\frac{p'^{eq}}{p_T'^{eq}} \right)^{\beta} \frac{\partial f_T}{\partial \sigma'_{ij}} \tag{5.11}$$

For clays with natural bonding, there are existing bonds at a reference temperature to make the clay stiffer in its natural state when compared to the recostituted state at a given reference temperature. The reference surface with structure under a reference temperature can be expressed as Eq. 5.12.

$$p_{Tref}'^{eq} = (1 + \chi) p_{ic0}'^{eq} \tag{5.12}$$

If the temperature T differs from the reference temperature T_{ref}, and the effective stresses are kept constant under thermal loading, the apparent preconsolidation pressure is affected by the difference between the reference temperature and the current temperature, as expressed in Eq. 5.4. Thus, the equivalent apparent preconsolidation pressure under a temperature that is different from the reference temperature is expressed with Eq. 5.13.

$$\frac{p_T'^{eq}}{p_{Tref}'^{eq}} = \left(\frac{T}{T_{ref}} \right)^{-(a\chi + b)} \tag{5.13}$$

which induces an increment of strain $\dot{\epsilon}_{ij}^{vp}$, as shown in Eq. 5.14.

$$\dot{\epsilon}_{ij}^{vp} = \dot{\Lambda} \left(\frac{p'^{eq}}{p_{Tref}'^{eq}} \right)^{\beta} \left(\frac{T}{T_{ref}} \right)^{\beta(a\chi + b)} \frac{\partial f_{ref}}{\partial \sigma'_{ij}} \tag{5.14}$$

Not only does the apparent preconsolidation pressure develop with the viscoplastic strains, the structure parameter χ and the fabric tensor α (controlling the inclination of the reference surfaces). α also change upon the hardening of the clay, as described in Eqs. 3.12 and 3.18. The determination of the parameters for rotational hardening and the degradation of bonding are discussed in Section 3.3.

The isotropic hardening of the clay depends both on the temperature change and the volumetric strain, as expressed with Eq. 5.15.

$$\dot{p}_T'^{eq} = \frac{\partial p_T'^{eq}}{\partial \varepsilon_v^{vp}} \dot{\varepsilon}_v^{vp} + \frac{\partial p_T'^{eq}}{\partial T} \dot{T} \tag{5.15}$$

The apparent preconsolidation pressure changes upon thermal loading. Under temperature

decrement, the apparent preconsolidation pressure increases

$$\dot{p}_T'^{eq} = p_T'^{eq}\left(\frac{\dot{\varepsilon}_v^{vp}}{\lambda_i^* - \kappa^*}\right) - (a\chi + b)p_T'^{eq}\left(\frac{T}{T_{ref}}\right)^{-(a\chi+b)}\left(\frac{\dot{T}}{T}\right) > 0 \tag{5.16}$$

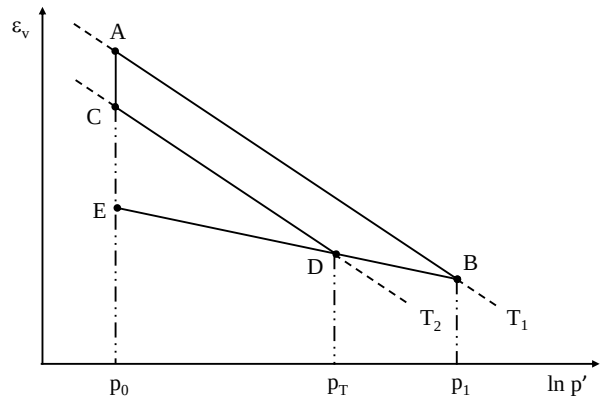

Figure 5.7: Sketch for isotropic compression.

At Point A, the clay sample is assumed to be normally consolidated, and consequently loaded to Point B in Fig. 5.7. At Point B, the clay sample is heated from T_1 to T_2 ($T_2 > T_1$), consequently the apparent preconsolidation pressure reduces from p_1 to p_T. The current stress state, however, still stays at p_1. Thus, a viscoplastic strain develops to make the reference surface larger than the current stress surface. In this case, the apparent preconsolidation pressure depends both on temperature and the developing strains, as expressed in Eq. 5.17.

For normally consolidated clays subjected to heating, the apparent preconsolidation pressure decreases, and the clay develops volumetric viscoplastic strain to compensate for the decrement in the apparent preconsolidation pressure to maintain the reference surface $p_{Tref}'^{eq}$ beyond the loading surface p'^{eq}. Thus, the equivalent stress expands following the hardening law in Eq. 5.17 together with mechanical hardening $(\lambda_i^* - \kappa^*)\Delta \ln p' = \Delta\varepsilon_v^{vp}$, as sketched in Fig. 5.7.

$$\dot{p}_T'^{eq} = p_T'^{eq}\left(\frac{\dot{\varepsilon}_v^{vp}}{\lambda_i^* - \kappa^*}\right) - (a\chi + b)p_T'^{eq}\left(\frac{T}{T_{ref}}\right)^{-(a\chi+b)}\left(\frac{\dot{T}}{T}\right) < 0 \tag{5.17}$$

If the temperature is equal to the reference temperature, the viscoplastic multiplier

becomes Eq. 5.18, which is the same as Eq. 3.20.

$$\dot{\Lambda} = \frac{\mu_i^*}{\tau} \frac{M_c^2 - \alpha_{K0}^2}{M_c^2 - \eta_{K0}^2} \tag{5.18}$$

Therefore, the viscoplastic strain increment under combined thermo-mechanical loading can be expressed as Eq. 5.19.

$$\dot{\epsilon}_{ij}^{vp} = \frac{\mu_i^*}{\tau} \frac{M_c^2 - \alpha_{K0}^2}{M_c^2 - \eta_{K0}^2} \left(\frac{p'^{eq}}{p_{Tref}'^{eq}} \right)^{(\lambda_i^* - \kappa^*)/\mu_i^*} \left(\frac{T}{T_{ref}} \right)^{(a\chi+b)(\lambda_i^* - \kappa^*)/\mu_i^*} \frac{\partial f}{\partial \sigma_{ij}'} \tag{5.19}$$

5.3 Verification of Creep-SCLAY1ST

The modified model is applied to simulate the static heating and cooling tests. The ability of this model in capturing the temperature-dependent mechanical behaviour is verified by the simulations of constant rate of strain (CRS) and undrained triaxial loading paths.

The intrinsic mechanical parameters, such as the modified intrinsic compression index λ_i^* and the modified intrinsic creep index μ_i^*, are based on the laboratory tests on remoulded samples from the corresponding depths. These values are assumed to be constant during the test procedure, and hence temperature-independent, even though the modified intrinsic compression index λ_i^* in the heating paths appears to be slightly higher than in cooling paths. The parameters used in the simulations are listed in Table 4.1. The results are presented in the following sections.

5.3.1 Simulation of oedometer tests

Validation against static tests

The oedometer tests selected for simulations with Creep-SCLAY1ST are identical with the tests simulated in Chapter 4.

Remoulded samples

The simulations with Creep-SCLAY1ST on remoulded samples of clay from two different depths with mechanical loading path O_1 are compared with the experimental results ($\triangle$ for heating and $\bigcirc$ for cooling) in Figs. 5.8 & 5.9. Compared with the simulations with the temperature-invariant model (Figs. 4.18 & 4.19), the difference is rather small. The

influence of temperature is rather insignificant for remoulded clays.

As reported in Chapter 4, the static tests cooling are performed on the remoulded samples with a smaller initial void ratio than the static heating tests, i.e. the samples in the static cooling tests have less compression after the apparent preconsolidation pressure.

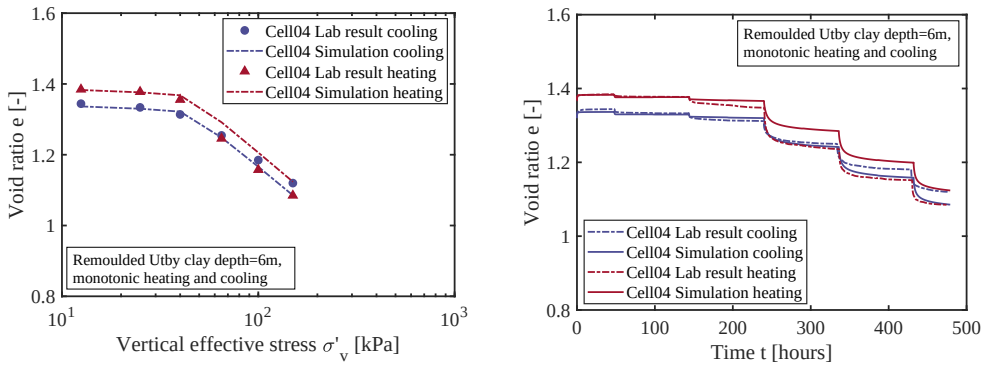

(a) Stress strain for Cell04

(b) Time displacement for Cell 04

Figure 5.8: Results on sample remoulded from 6 meter Cell 04 with Creep-SCLAY1ST.

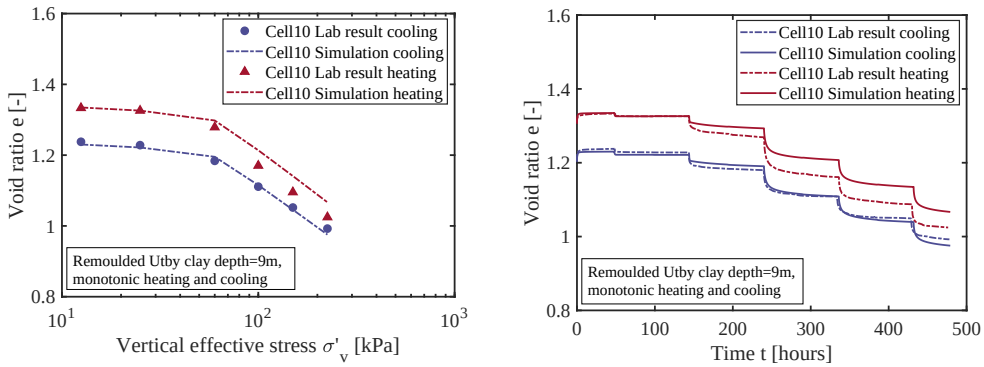

(a) Stress strain for Cell10

(b) Time displacement for Cell 10

Figure 5.9: Results on remoulded sample from 9 meter Cell 10 with Creep-SCLAY1ST.

There is one step for loading path O_1 where the samples are subjected to identical stress histories, and subsequently loaded with different temperature increments (15 °C to 20 °C in heating and 15 °C to 10 °C in cooling). Compared to Figs. 4.26(b) & 4.27(b), where deformation is higher in cooling than in heating, Creep-SCLAY1ST is capable of capturing the trend of deformation as plotted in Fig. 5.10. In the simulations, heating leads to larger deformation than cooling in a remoulded sample under the same effective

stress state.

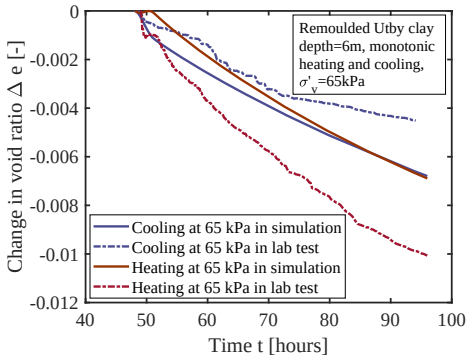

(a) Depth = 6 m

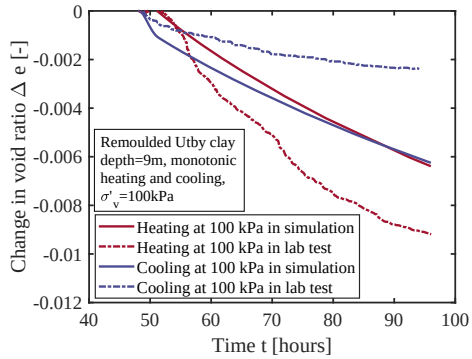

(b) Depth = 9 m

Figure 5.10: Change in void ratio under thermal loading at a stress level just after the apparent preconsolidation pressure.

Intact samples from 6 meters $\chi_0 = 6$

The simulations using the temperature-dependent constitutive model on intact samples from 6 meter with loading paths O_1, O_2 & O_3 are compared with experimental results ($\triangle$ for heating and $\bigcirc$ for cooling) in Figs. 5.11, 5.12 & 5.13.

The multi-physics simulations with Creep-SCLAY1ST capture the general mechanical behaviour satisfactorily both for the compression curves (Figs. 5.11(a), 5.12(a) & 5.13(a)) and the time-void ratio curves (Figs. 5.11(b), 5.12(b) & 5.13(b)).

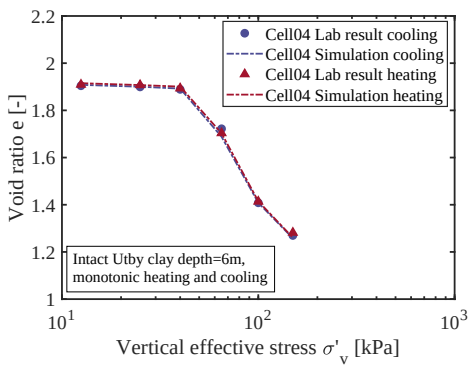

(a) Stress strain for Cell 04

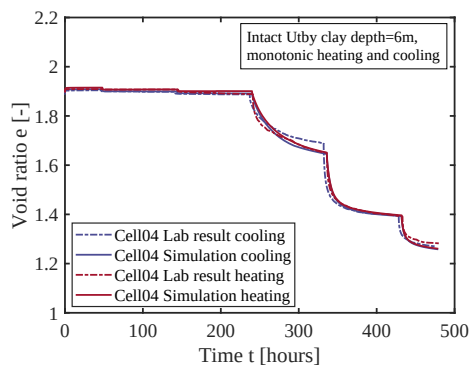

(b) Time displacement for Cell 04

Figure 5.11: Results on intact sample from 6 meter Cell04 with Creep-SCLAY1ST.

For loading path O_2, where the samples are loaded beyond the apparent preconsolidation pressure under T_2 (20°C in static cooling and 10 °C in static heating), the differences between the static tests are captured well. For a clay sample with a smaller initial degree of bonding, the differences in the simulations with the temperature-dependent (Fig. 5.12) and temperature-invariant model (Fig. 4.21) are small.

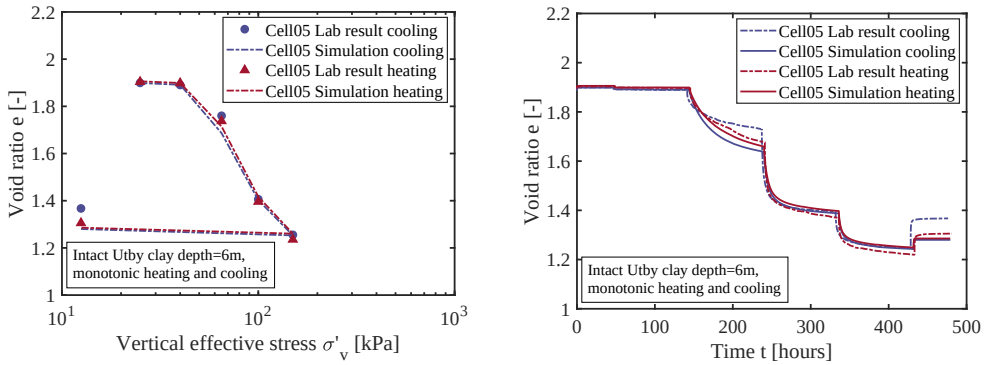

(a) Stress strain for Cell 05

(b) Time displacement for Cell 05

Figure 5.12: Results on intact sample from 6 meter Cell 05 with Creep-SCLAY1ST.

For loading path O_3, the samples are mechanically loaded under temperatures T_1 (25°C in static cooling and 5 °C in static heating), the difference between the heating and cooling tests is more pronounced than for loading path O_2 and is better captured by the temperature-dependent model (Fig. 5.13) than the temperature-invariant model (Fig. 4.22).

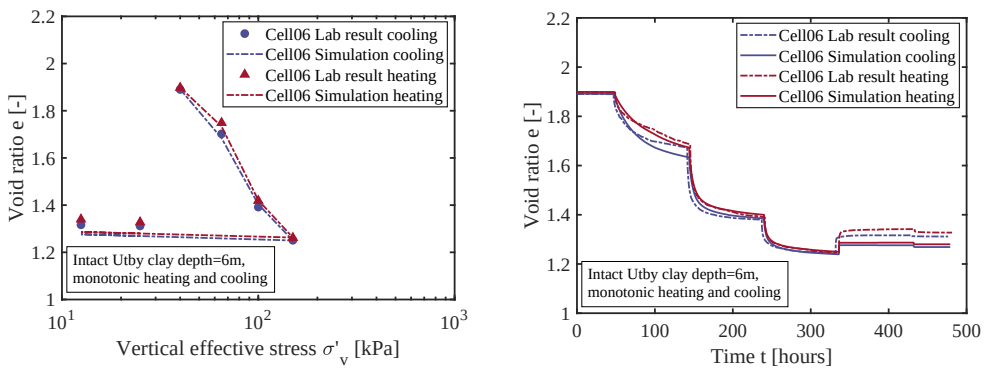

(a) Stress strain for Cell 06

(b) Time displacement for Cell 06

Figure 5.13: Results on intact sample from 6 meter Cell 06 with Creep-SCLAY1ST.

Intact samples from 9 meters $\chi_0 = 14$

The samples with higher sensitivity from a depth of 9 meters, with an initial structure parameter $\chi_0 = 14$, are simulated for loading paths O_1, O_2 & O_3. The mechanical behaviour is captured better by the temperature-dependent model (Fig. 5.14, 5.15 & 5.16) than the temperature-invariant model (Figs. 4.23, 4.24 & 4.25).

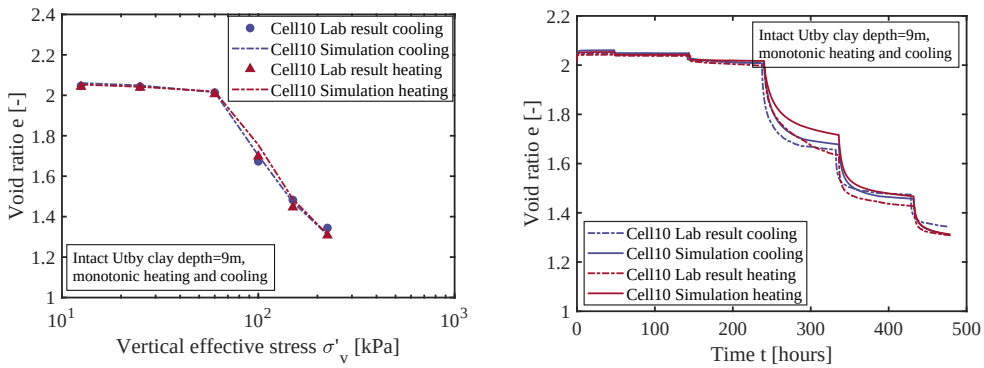

(a) Stress strain for Cell 10

(b) Time displacement for Cell 10

Figure 5.14: Results on intact sample from 9 meter Cell 10 with Creep-SCLAY1ST.

For loading path O_2, where the samples are loaded beyond the apparent preconsolidation pressure under T_2 (20°C in static cooling and 10 °C in static heating), the differences between the static heating and cooling are notable. These differences between cooling and heating paths are reproduced with high accuracy by the temperature-dependent constitutive model (Fig. 5.15).

For loading path O_3, with the samples mechanically loaded beyond the apparent preconsolidation pressure under T_1 (25°C in static cooling and 5 °C in static heating), the differences between the static heating and cooling paths are the largests. Yet, this is captured well with the temperature-dependent model, see Fig. 5.16.

The accuracy in modelling the sensitive clay under combined thermal and mechanical loading is significantly improved when the temperature-dependent Creep-SCLAY1ST model is used. The results particularly improved for stress levels beyond the apparent preconsolidation pressure in samples with significant apparent bonding, see the compression curves (Figs. 5.15(a) & 5.16(a)) and the time-void ratio curves (Figs. 5.15(b) & 5.16(b)).

Similarly to the remoulded samples, the intact clay samples with identical stress histories are thermally loaded from an equal temperature for heating (15 °C to 20 °C) and cooling (15 °C to 10 °C) in loading path O_1. The thermal steps are well predicted in with the modified model as plotted in Fig. 5.17. The differences between the heating and cooling

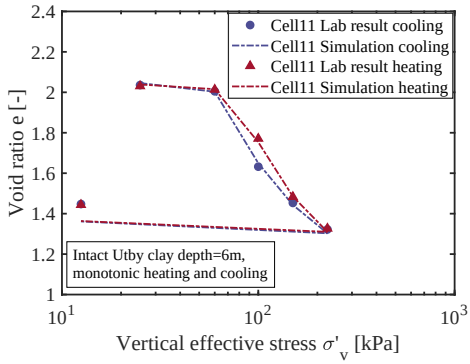

(a) Stress strain for Cell11

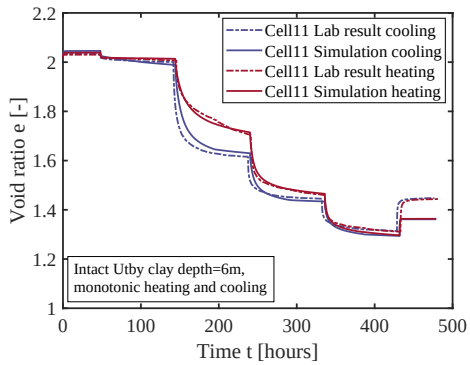

(b) Time displacement for Cell 11

Figure 5.15: Simulation results on intact sample from 9 meter Cell 11 with Creep-SCLAY1ST.

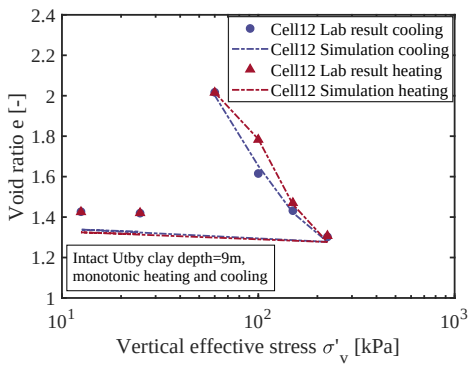

(a) Stress strain for Cell12

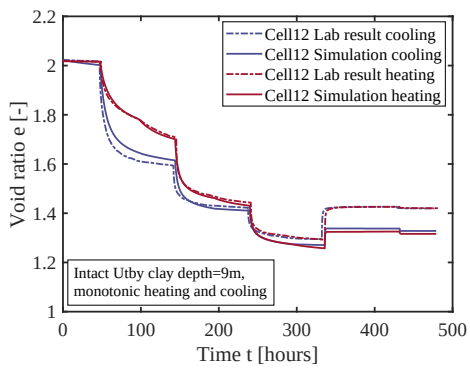

(b) Time displacement for Cell 12

Figure 5.16: Simulation results on intact sample from 9 meter Cell 12 with Creep-SCLAY1ST.

are significantly improved for the clay samples from 6 meters depth (Fig. 4.26(a) vs. Fig. 5.17(a)) and 9 meters depth (Fig. 4.27(a) vs. Fig. 5.17(b)).

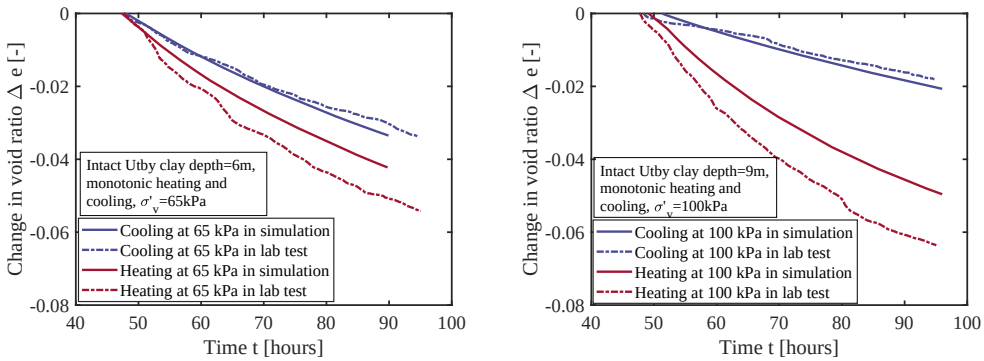

(a) depth=6m (b) depth=9m

Figure 5.17: Results on thermal loading steps with Creep-SCLAY1ST.

5.3.2 Simulations of other loading paths in compression

An additional series of simulations are performed to verify the performance of the model for other loading paths in compression. First, constant rate of strain (CRS) tests are modelled, before considering undrained triaxial compression tests.

The reference temperature T_{ref} is 7 °C for all simulations of CRS tests using Creep-SCLAY1ST. The boundary level simulations are for samples that are 50 mm in diameter and 18 mm in height as shown in Fig. 5.18(a), where d is the displacement and u is the excess pore pressure on the boundary. The samples are axially loaded on the upper boundary with a displacement rate of 0.0024 mm/min, equal to the Swedish practice. The model parameters are the same as listed in Table 4.1, except for the structure parameter χ_0 which represents the initial amount of bonding.

The initial structure of the high quality block samples from the depth of 6 and 9 meters varies between 26 and 32, see Karlsson et al. (2016). The compression curves for the simulated CRS tests under different temperatures (5 °C, 10 °C, 15 °C, 20 °C, 25 °C) are shown in Fig. 5.19 for samples from 9 meters with two different amounts of initial bonding: $\chi_0 = 14$ & $\chi_0 = 25$. The temperature-dependency of the apparent preconsolidation pressure is substantially larger for samples with a larger amount of initial bonding χ_0. Furthermore, the natural bonding affects the stiffness after yield.

When assuming an equal size for the intrinsic yield surface p'_{ico}, but a different amount of bonding χ_0, the preconsolidation pressure increases with an increase in the amount of bonding, given that $p'_c = (1+\chi_0)p'_{ico}$. At a higher temperature of 25 °C, the clay samples

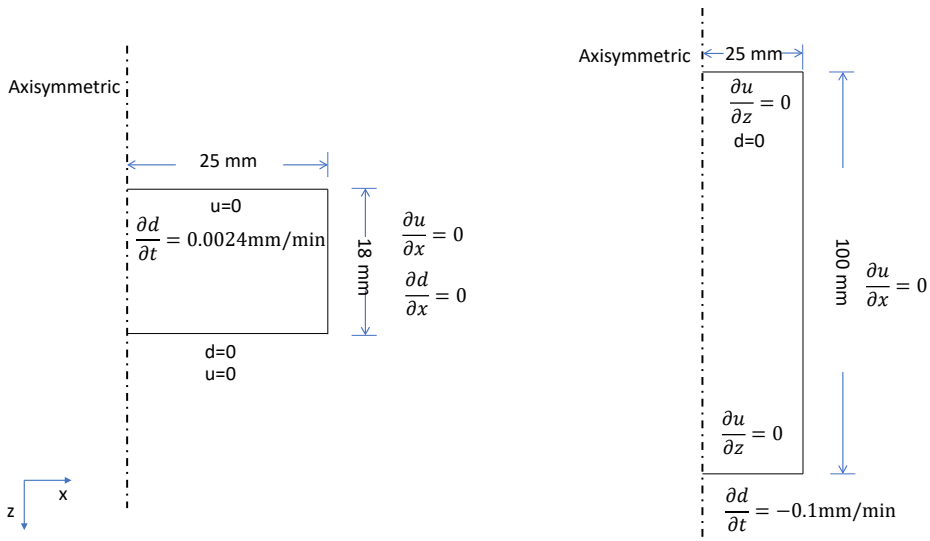

(a) CRS tests

(b) Undrained triaxial tests

Figure 5.18: Boundary conditions for CRS and undrained triaxial tests.

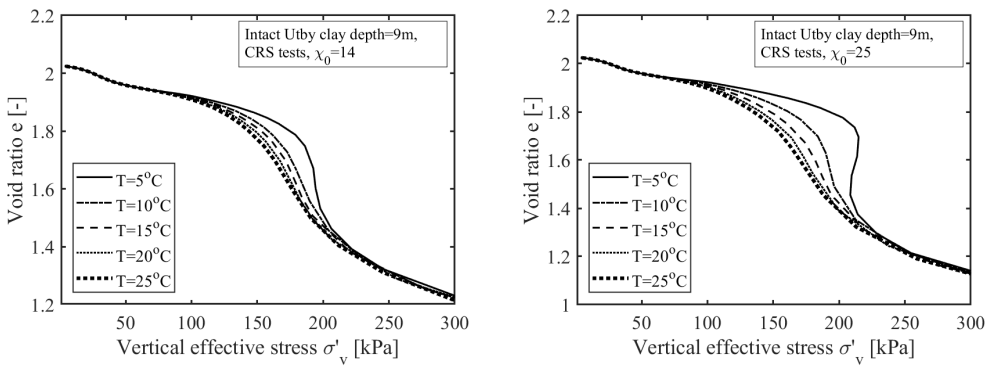

(a) $\chi_0 = 14$

(b) $\chi_0 = 25$

Figure 5.19: Simulations of CRS test under different temperatures with Creep-SCLAY1ST.

reach the intrinsic compression lines faster than under 10 °C, i.e the bonds between the particles degrade faster with a larger temperature increment T/T_{ref}, as plotted in Fig. 5.20.

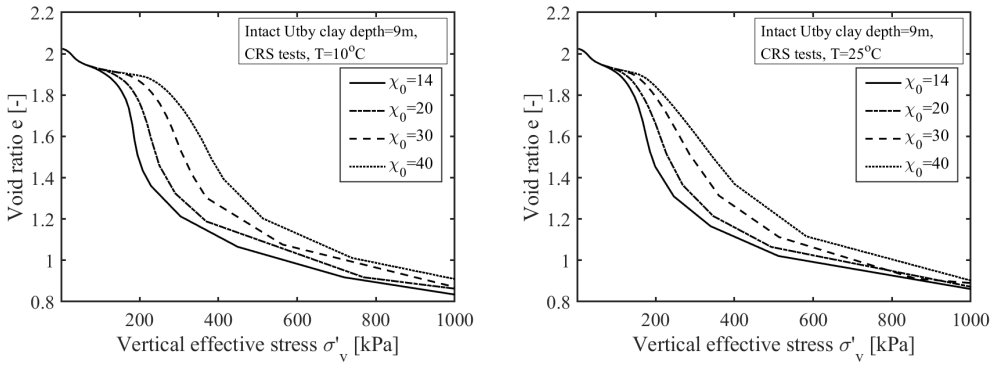

(a) $T = 10$ °C (b) $T = 25$ °C

Figure 5.20: Simulations of CRS test with different amounts of initial bonding with Creep-SCLAY1ST.

5.3.3 Simulation of undrained triaxial tests

A series of consolidated undrained triaxial tests are simulated with Creep-SCLAY1ST, in order to study the influence of temperature and the initial amount of bonding under shearing.

In the simulations, the triaxial samples are 50 mm in diameter and 100 mm in height as shown in Fig. 5.18(b). These samples are first isotropically loaded to the mean effective stress of $p' = K_0^{NC}\sigma'_{v0}$, and subsequently loaded at the bottom boundary with a vertical strain rate of 0.001%/min (0.1mm/min). The simulations are carried out using the values listed in Table 4.1, except for the initial structure parameter χ_0.

In Fig. 5.21, samples with different amount of bonding (χ=14 in Fig. 5.21(a) and χ=30 in Fig. 5.21(b)) are simulated under different temperature (5 °C, 10 °C, 15 °C, 20 °C, 25 °C). The apparent preconsolidation pressure decreases with increasing temperature when comparing the $p' - q$ curves in Fig. 5.21. This phenomenon is more pronounced in clays with a higher amount of initial bonding χ_0, as seen by comparing Fig. 5.21(a) and 5.21(b).

In this Chapter, a new version of the Creep-SCLAY1S model, called Creep-SCLAY1ST, which has temperature- and initial bonding-dependent apparent preconsolidation pressure is developed, using the data from the incrementally loaded oedometer tests. The new model is by simulating CRS tests and undrained triaxial tests, because of the lack of

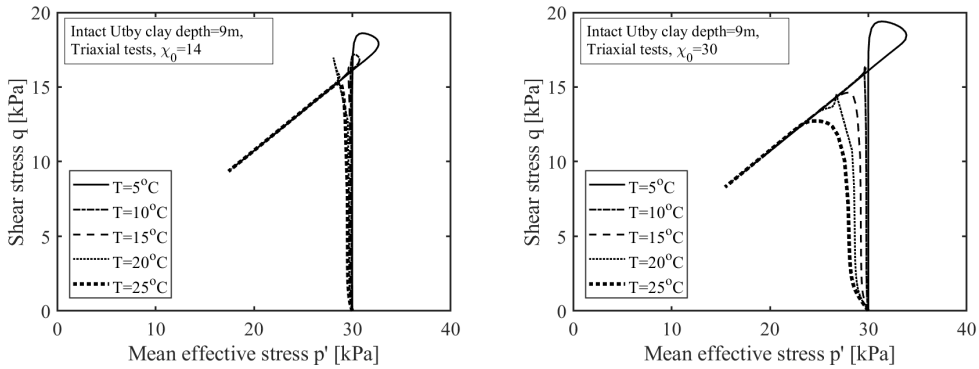

(a) $\chi_0 = 14$ (b) $\chi_0 = 30$

Figure 5.21: Simulation results of undrained triaxial shearing at different temperatures with Creep-SCLAY1ST.

available laboratory tests, and the results seem reasonable. The modified model, however, need be further validated using the results from independent laboratory tests (both CRS and triaxial) conducted at various temperatures. In the next Chapter, the modified model is applied to the simulation of the oedometer tests with thermal cycles to study the long-term behaviour of sensitive clays under periodical temperature changes.

6 Oedometer tests with thermal loading cycles

In this Chapter, the behaviour of sensitive clays under cyclic thermal loads is investigated experimentally and compared to the numerical simulations. The thermal loading programme is designed to study conditions that are representative for geothermal energy foundations in general, and the field tests performed on the Utby test site by Bergström (2017) in particular.

6.1 Clay with thermal cycles in laboratory tests

6.1.1 Test details

So far only the effects of monotonic thermal loading, i.e, the slow tests, that lead to drained loading paths have been studied to assist the model development. Most geothermal structures, however, induce thermal loading cycles into the soil. Hence, a series of thermal cyclic oedometer tests has been performed in order to investigate the effect of thermal load cycles on the emerging rate-dependent response of sensitive clays. The thermal loading rate remains relatively low, reflecting in-situ conditions near energy foundations. Another main interest is to study the effect of the initial amount of bonding on the response in more detail, as the monotonic test results indicate that this is a crucial mechanism.

The fast thermal loading setup that uses a water circulation system has been used for Cells 01, 02 & 03 depicted in Fig. 3.6. The hydraulic and thermal boundary conditions of this test are summarised in Fig. 6.1. The lower boundary of the oedometer cell is closed to facilitate pore water pressure measurements, whilst the upper boundary is an open boundary that facilitates dissipation of excess pore water pressures. In addition to the vertical displacements, also the temperature and excess pore water pressure measurements have been monitored in all three cells. All readings are calibrated to include (minor) temperature effects. Given the long test periods and slow precesses, the sampling period was five minutes in the majority of the tests. The latter gives sufficient data to apply a 5-sample moving average filter on the pore pressure measurements that suppresses some of the high frequency peaks in the original data.

In all cyclic tests the applied thermal load follows a harmonic function as described in Equation 3.22 *bis* with an amplitude A_T of 10°C and an average temperature T_{avg} of 15°C. As a result the applied temperature T varies between 5°C and 25°C. As described in Section 3.4.2 the loading period t_p is sequentially increased for each group of 10 cycles, i.e. $t_p = 4$, 8, 12 & 16 h. This implies that before the $t_p = 12$ h, the sample already experienced 20 loading cycles. The effective stress levels are varied in-between the three test cells,

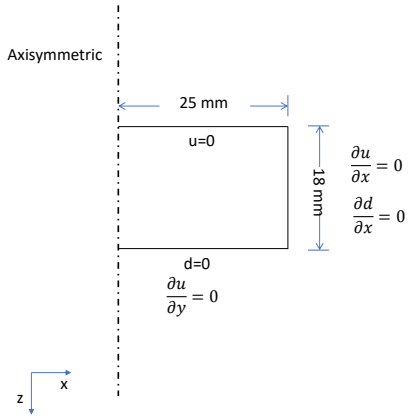

Figure 6.1: Boundary conditions for oedometer tests with thermal cycles.

i.e. $\sigma'_v = 60$ (Cell 01), 100 (Cell 02), 150 kPa (Cell 03). The apparent preconsolidation pressure for the samples from 9 m depth is $\sigma'_{pc} \approx 70$ kPa.

$$T = A_T \sin(\frac{2\pi}{t_p}\frac{t}{3600} + \frac{3\pi}{2}) + T_{avg} \qquad (3.22\ bis)$$

The applied temperature cycles in the tests, as measured in the experimental results are plotted in Fig. 6.2. In addition to the temperatures measured in the water bath surrounding the sample, two additional traces are plotted: the setpoint and the temperature in the water tank. Fig. 6.2(a) plots the results for the cyclic tests with a period t_p of 8 hours whilst Fig. 6.2(b) shows data for the tests with a loading period of t_p of 12 hours. Consistent performance is achieved, given the simplicity of the system. Closer inspection of the data, however, shows that the temperature in the water bath slightly differs from the set-point, due to the differences in the response time and efficiency of the heater and climate room. This particular setup uses the climate room, set to (5°C), to cool the sample when the heater is switched off. As a result for a relatively short thermal loading period t_p, the lowest temperature target of 5°C is not reached in time. In contrast, the highest temperature for all thermal cycles with different periods overshoots the setpoint (25°C). This behaviour of the control loop is due to the asymmetry in the available energy for cooling (climate room installation) and heating (a modest 1000 W heater in a water bath) which is difficult to optimise in a simple PID loop.

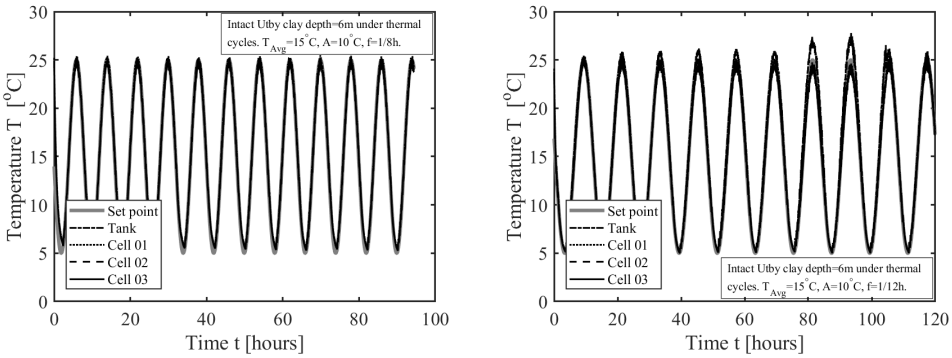

(a) T_P=8h (b) T_P=12h

Figure 6.2: Temperature in oedometer tests with temperature cycles.

6.1.2 Test results

The cyclic results that will be presented represent intact and remoulded samples from a depth of 9 meters at Utby site. The initial results from the static oedometer tests from a depth of 6 meters seem to deviate too much from the static reference tests used for model calibration, and thus do not provide reliable comparison for complementary cyclic data. By reducing the loading period, the peak heating rate ranges from 3.9 °C/h (t_p = 16 hours) to 15.7 °C/h (t_p = 4 hours). This change in the thermal loading period has only a rather small effect on the magnitude of the generated excess pore water pressures, i.e. $\approx$ 2% of the effective stress level of the loading step, which is largest in the reconstituted samples. Therefore, this Chapter will only present and discuss the results for one loading period at different effective stress levels, with a focus on studying the effect of the initial amount of bonding. For further reference, a complete overview of all results is given in Appendix B. The loading period of t_p = 12 hours is selected as this provides the most reliable data set in terms of test continuity and sample quality. Please note that this refers to a thermal cyclic loading stage performed after completion of 10 load cycles with t_p = 4 hours, and 10 load cycles with t_p = 8 hours, for a total of 120 hours.

Figs. 6.3 & 6.4 present the measured time series for void ratio e and excess pore water pressures Δu for three load steps (σ'_v = 60, 100 & 150 kPa) for both the intact and remoulded samples from 9 m depth. The thermal loading cycles applied in these tests are already presented in Fig. 6.2(b), however for completion, the curve for the temperature setpoint is repeated above the void ratio and pore pressure graphs. Note that the vertical scale is not constant throughout the subfigures, in order to discern the small changes in each individual test. For ease of comparison, the results are combined and plotted in Fig. 6.5.

The measured changes in void ratios are practically in phase with the temperature change

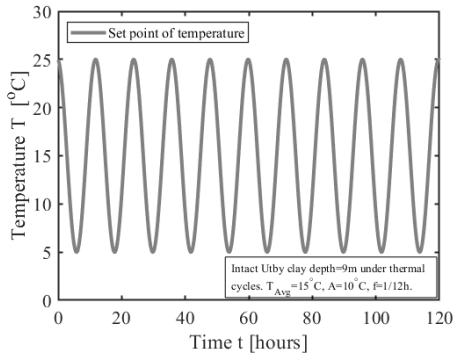

(a) Setpoint for intact samples

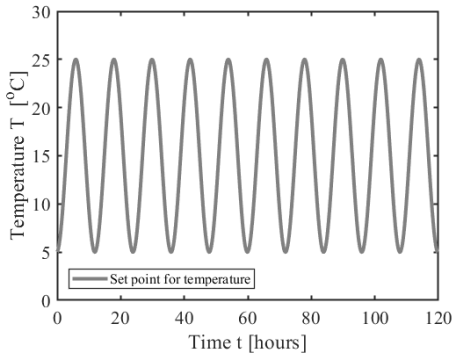

(b) Setpoint for remoulded samples

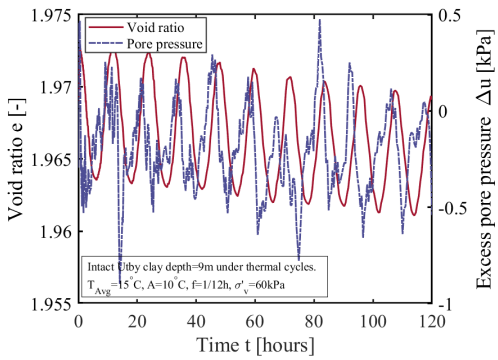

(c) Intact 60 kPa

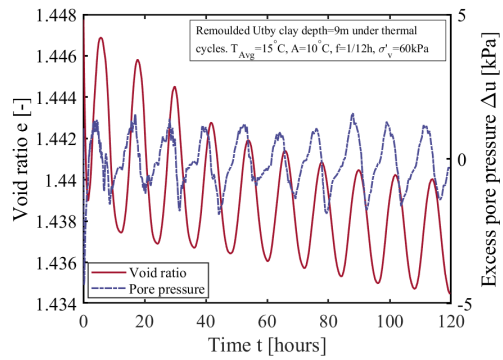

(d) Remoulded 60 kPa

Figure 6.3: Pore pressure and void ratio of samples at 60 kPa during thermal cycles with a period of 12 hours.

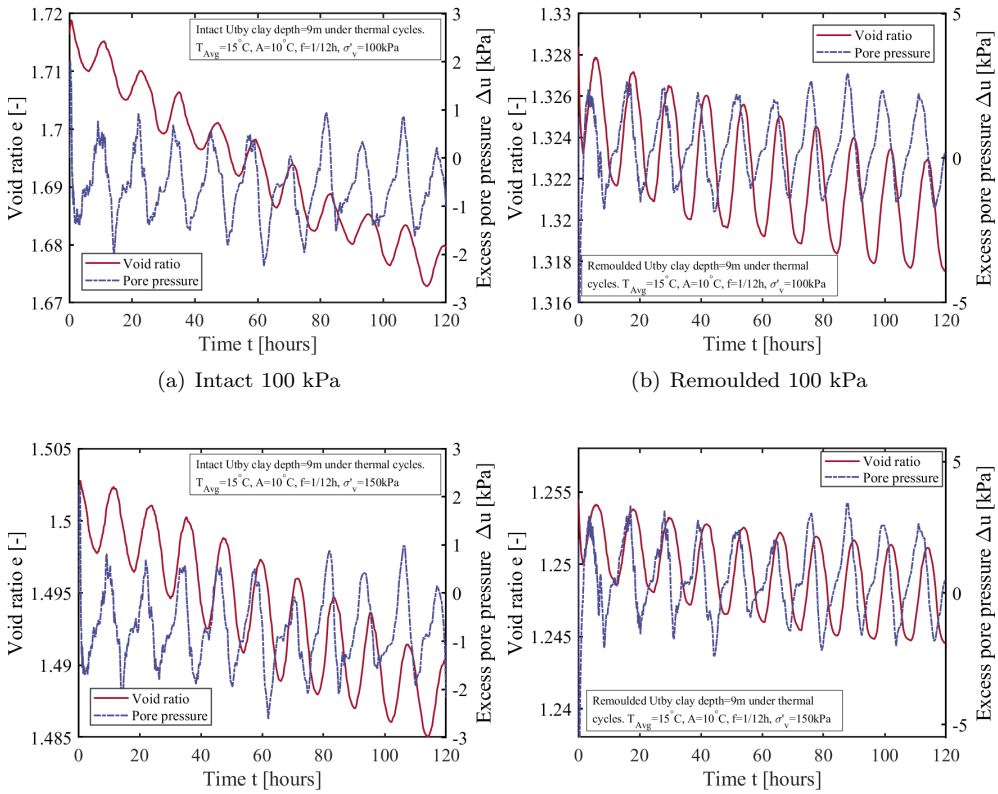

(a) Intact 100 kPa

(b) Remoulded 100 kPa

(c) Intact 150 kPa

(d) Remoulded 150 kPa

Figure 6.4: Pore pressure and void ratio of samples under different stress levels during thermal cycles with a period of 12 hours.

applied for all load steps studied. In contrast the peak in excess pore water pressures is largest for the largest heating rates, and hence is shifted a half period t_p in time to be in sync with the steepest part of the temperature signal. The somewhat irregular shape of the excess pore water pressure curves is for a large part a result of the small magnitudes close to the resolution of the pressure transducer (0.5 kPa).

The excess pore water pressures are benign and for heating and cooling cycles a direct consequence of the restricted flow resulting from the dissimilar thermal expansion of the pore water and the soil matrix. The smallest magnitudes are registered for the load step before the apparent preconsolidation pressure, whilst for the other load steps the amplitude of the measured pore water pressures A_u increases with effective stress level ($A_{u60kPa} < A_{u100kPa} < A_{u150kPa}$) in Fig. 6.5(a) & 6.6(a). The largest magnitudes are found for the remoulded samples, which have perhaps a higher degree of saturation than the intact specimens. The absolute magnitude of measured change in pore pressures is rather low for all load steps in intact and remoulded samples, i.e. $|u|$ is less than 5 kPa. This is consistent with the excess pore water pressures measured in the field tests on floating thermal piles in sensitive clays with thermal cycles conducted by Bergström (2017), where the maximum excess pore pressure measured in field tests were less than 5 kPa.

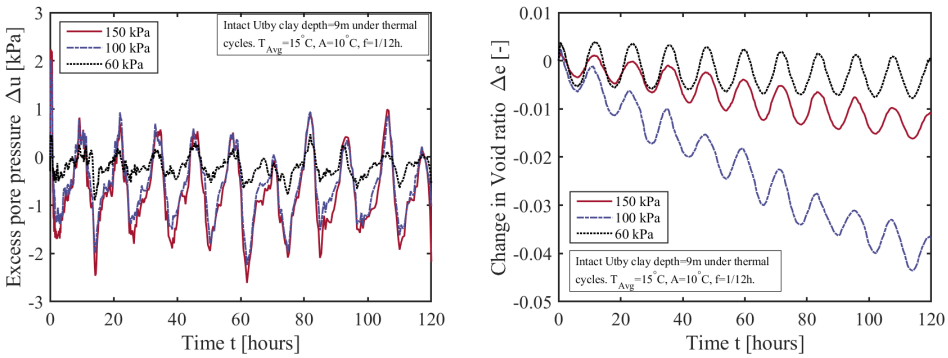

(a) Pore pressure

(b) Change in void ratio

Figure 6.5: Pore pressure and change in void ratio in oedometer tests with temperature cycles with a period of 12 hours for intact clay.

Compared to prior work performed in undrained conditions and large temperature variations, the current research focuses on thermal loading cycles with open drainage and relatively small thermal loading amplitudes. As a result, no accumulation of excess pore water pressures is observed in the current tests. This small change of 5 kPa in effective stress is unlikely to trigger additional settlements in a deposit of sensitive clay as it is in the same order of magnitude as the natural seasonal fluctuation of the groundwater table.

The effective stress cycles resulting from the measured excess pore water pressures

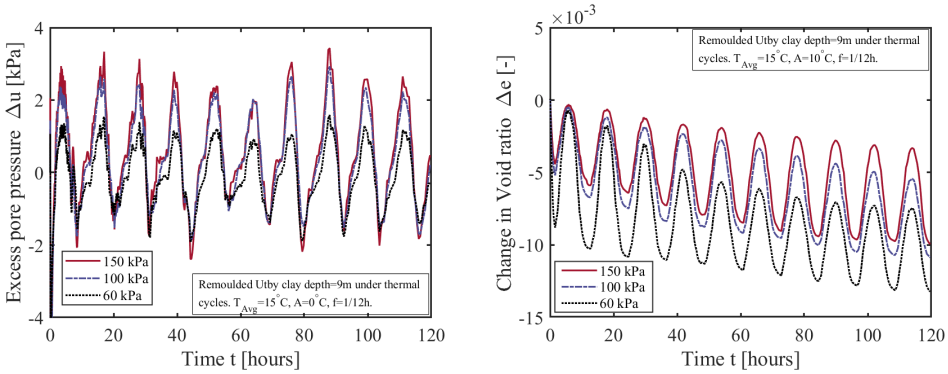

(a) Pore pressure

(b) Change in void ratio

Figure 6.6: Pore pressure and change in void ratio in oedometer tests with temperature cycles with a period of 12 hours for remoulded clay.

corresponds, for the stiffness of the tested clay, to a change of void ratio in the order of Δe=0.01. Additional volumetric thermal expansion and contraction effects with a similar magnitude of $\Delta e = 0.01$ of the clay matrix itself are expected. These mechanisms are additive, as associated with an increase in temperature, a (volumetric) thermal expansion and a reduction in effective stress both lead to a volume expansion. Finally, it is expected that thermal softening effects can trigger additional viscoplastic strains resulting from a reduced apparent pre-consolidation pressure.

When studying the void ratio response in more detail during thermal loading cycles, plotted in Fig. 6.4, there is an ongoing deformation with time, on which a cyclic signal with an amplitude Δe superimposed. The magnitude of this amplitude falls within the expected range $\Delta e = 0.01$ that results from changes in effective stress and thermal expansion/contraction effects. Given that the phase of Δe is in sync with the forced temperature change, it is most probable that the thermal expansion and contraction mechanisms are the primary effects observed in this test series.

The intact clay samples are more sensitive to temperature change than the remoulded samples, as well as that similarly to the monotonic heating and cooling tests, the largest change in void ratio is found in the sample that is subjected to a stress level of 100 kPa (Fig. 6.4(a)), a stress level just above the apparent preconsolidation pressure (σ'_{pc}=70 kPa). Compared to the response of intact clay near the apparent pre-consolidation pressure, the effects of thermal loading are more limited for the other stress levels for the intact samples, and negligible in remoulded clay samples when comparing 6.6(b) with Fig. 6.5(b).

Because of the two hardening mechanism (thermal softening and volumetric hardening), the mechanical strain and thermal strain cannot be separated for normally consolidated or slightly overconsolidated clays, especially under the conditions where pore water pressures change with temperature.

6.1.3 Comparison between slow and cyclic thermal loading

In order to investigate if the thermal cyclic loading substantially affects the creep rates, a comparison is made with the slow monotonic thermal loading tests.

In Step 71 and Step 72 (S_{71} and S_{72} in Table 3.5) of the static tests, samples from 9 m depth are thermally loaded from 15°C (with 5 °C increment and decrement) at an effective stress level of 100 kPa and 150 kPa, respectively. The results from this most representative load step (red: heating; blue: cooling) is compared against the cyclic data (black) in Fig. 6.7. When comparing the dashed lines for the stress level (σ'_v=100 kPa) just beyond the preconsolidation pressure, the change in void ratio is highest for the quasi-static tests with thermal cycles and lowest for static cooling tests. This is also observed in the samples under the vertical stress level of 150 kPa.

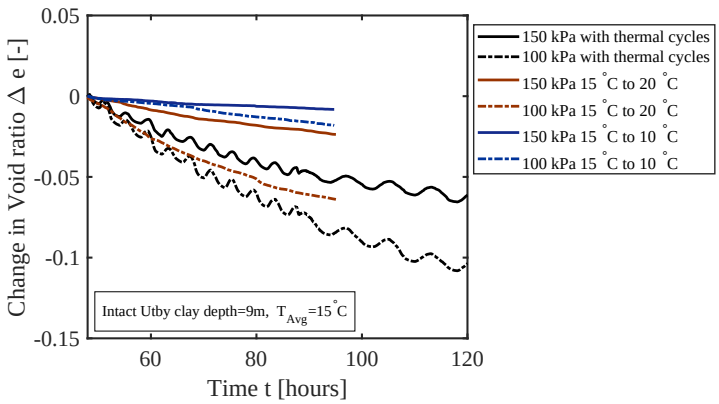

Figure 6.7: Strain evolution under mechanical loading after cyclic thermal loading.

In the quasi-static oedometer tests, the largest strain accumulated after 40 thermal cycles with 4 different periods t_p is around 6% for intact clay samples from the depth of 9 meters, with an ongoing strain rate that is not decreasing with time. This is most critical for the normally consolidated clay samples that are subjecting to cyclic thermal loading. For the clay under the vertical stress of 100 kPa, the change in void ratio Δe is 0.1 after 5 days of thermal cycles (Fig. 6.7).

Assuming that the in-situ void ratio of the clay deposit is 2 (which is similar to the initial void ratio in Table 3.1), the deformation found in the laboratory will translate to 333 mm in 5 days for a natural intact clay deposit that has a thickness of 10 m. These magnitudes have not been observed in the field test at Utby reported by Bergström (2017). This is partly due to stress states in the soil surrounding the pile that are not necessarily in the critical range, but more importantly partly linked to the state of the soil surrounding the pile, which is not intact due to the effects of pile installation.

During pile installation of displacement piles, as used in the field test, the soil around

the pile will be remoulded. A simplified estimate the extent of the disturbed zone can be obtained by coupling the Strain Path Method (Gudehus et al. 2008; Sagaseta and Whittle 2001) (that only resolves the strain path for an incompressible fluid) with a strain driver in which the SCLAY1S model is implemented, see Yannie (2016) for some details. The results of the SPM analysis are plotted with the temperature measurements from Bergström (2017) in Fig. 6.8. These quickly compiled results show that the largest change in temperature in the soil adjacent to the energy pile, as measured in the full-scale field test, coincide with the extent of the remoulded clay area as predicted by the SPM method (using the structure parameter χ). This explains the absence of large deformations in the field test. Further analyses incorporating pile installation effects, a multi-physics model and the newly developed model Creep-SCLAY1ST need to be performed to confirm these findings.

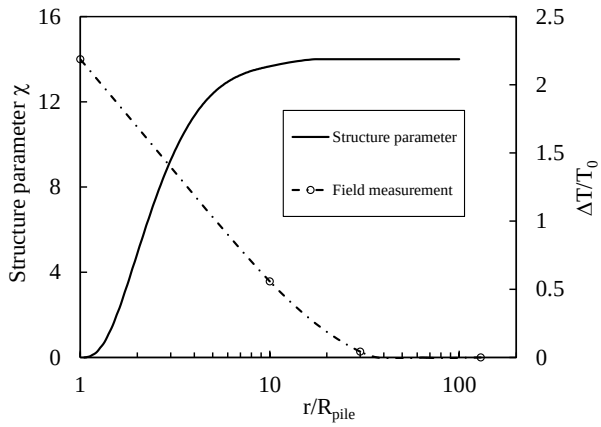

Figure 6.8: The area that is influenced by energy pile penetration and temperature change.

6.2 Simulation results on oedometer tests with thermal cycles

The oedometer tests with thermal loading cycles, presented above, are simulated at boundary value level using the temperature-invariant Creep-SCLAY1S model and the temperature-dependent Creep-SCLAY1ST model implemented in a fully coupled multi-physics framework, as presented in previous Chapters. Here the focus again is at simulating the experimental results for the cyclic thermal oedometer tests with loading period t_p 12 h on intact and remoulded samples from 9 m depth loaded to a vertical effective stress of σ'_v = 60, 100, and 150 kPa. The calibrated model parameters for Utby previously introduced are used in these simulations.

6.2.1 Change in effective stress

The pore water pressures calculated with the temperature-invariant model Creep-SCLAY1S and temperature-dependent model Creep-SCLAY1ST are shown in Fig. 6.9 for intact samples. For all three different simulated stress levels, the predicted pore water pressures with Creep-SCLAY1ST are slightly higher than those predicted with Creep-SCLAY1S. The change in the absolute pore water pressure $|\Delta u|$ is on average 1 kPa higher for Creep-SCLAY1ST. One source of this discrepancy is that the residual excess pore pressures are higher in the simulation with Creep-SCLAY1ST due to the larger strains predicted for the mechanical step prior to the cyclic thermal loading cycles.

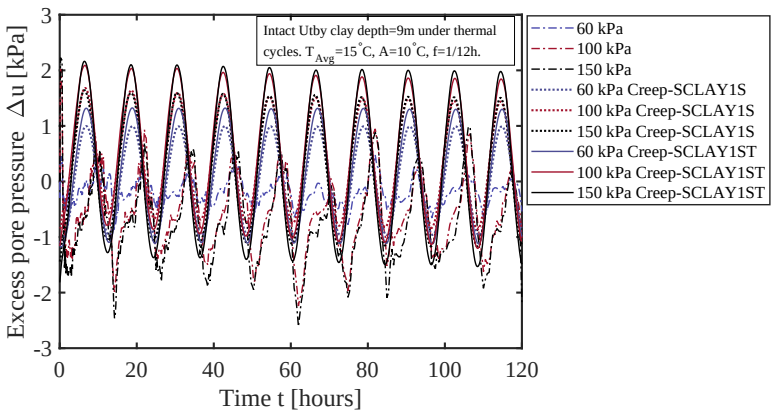

Figure 6.9: Excess pore water pressures resulting from thermal loading cycles simulated with Creep-SCLAY1S and Creep-SCLAY1ST.

In the simulated oedometer loading paths, the vertical effective stress is controlled by the dead weight load. The vertical stress starts from σ'_{v0} (in Table 3.4.2) before the application of thermal cycles. The axial stress $\sigma'_1 = \sigma_{v0} - u$, where u is the excess or negative pore water pressure generated upon heating or cooling. The radial stress $\sigma'_3 = \sigma'_1 K_0 = (\sigma_{v0} - u)K_0$, where K_0 is the the coefficient of lateral earth pressure at rest denothing the ratio between the horizontal (radial) effective stress and the vertical (axial) effective stress. The stress ratio η between the mean effective stress p' and the deviatoric stress q can be obtained as Eq. 6.1, which shows that the change in stress ratio q/p' depends solely on K_0. The stress ratio for the clay samples $\eta = q/p' = 0.94$ when assuming K_0=0.42 (using Jaky's relation).

$$\frac{q}{p'} = \frac{\sigma'_1 - \sigma'_3}{\frac{\sigma'_1 + 2\sigma'_3}{3}} = \frac{(\sigma_{v0} - u) - K_0(\sigma_{v0} - u)}{\frac{(\sigma_{v0} - u)}{3} + \frac{2(\sigma_{v0} - u)K_0}{3}} = \frac{3(1 - K_0)}{1 + 2K_0} \tag{6.1}$$

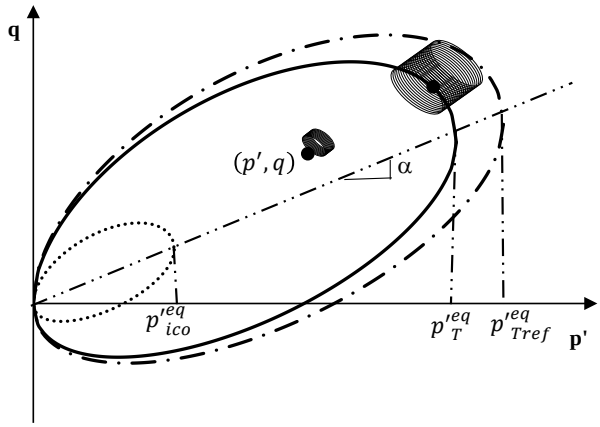

Figure 6.10: Cyclic 1D compression curve in p'-q space.

In a traditional oedometer test the horizontal stress cannot be measured directly or controlled. Thus, the stress ratio $\eta = q/p'$ is unknown and not necessarily constant during the test. If, for example, the clay samples compress under combined mechanical and cyclic thermal loading, the horizontal effective stress will increase. In these loading paths K_0 does not necessarily remain constant, as well as that ongoing stress relaxation or creep mechanisms further evolve the stress state (K_0). K_0 and the stress ratio are linked according to Eq. 6.1. Hence, the stress path of the samples can move out of the reference surface p'_{cT} as shown in Fig. 6.10.

The loading programme of the tested samples presented here is designed such that both an initial stress within the the reference surface (σ'_{v0} =60 kPa for Cell 01) and on the reference surface (σ'_{v0} =100 kPa for Cell 02 and 150 kPa for Cell 03) are studied. The simulated p'-q stress paths of the thermal cycling loading tests are plotted in Fig. 6.11 for the three different initial stress states. The solid lines represent the results from Creep-SCLAY1S model with pore pressure generation and the dashed line show the results using Creep-SCLAY1ST that also includes bonding-dependent thermal softening and pore pressure generation. The differences in the simulated stress-paths for the two models are rather small for all simulated stress levels.

6.2.2 Change in void ratio

The volumetric response of the intact and remoulded clay under thermal cyclic loading as simulated with Creep-SCLAY1S & Creep-SCLAY1ST are plotted in Fig. 6.12 for different loading periods t_p = 8 & 12 h. The change in void ratio Δe is predicted well by both models for each stress level. What is striking is that both models perform equally well. The largest differences between the simulations and the experimental data occur for the stress level just beyond the apparent preconsolidation stress σ'_v = 100 kPa. Both models

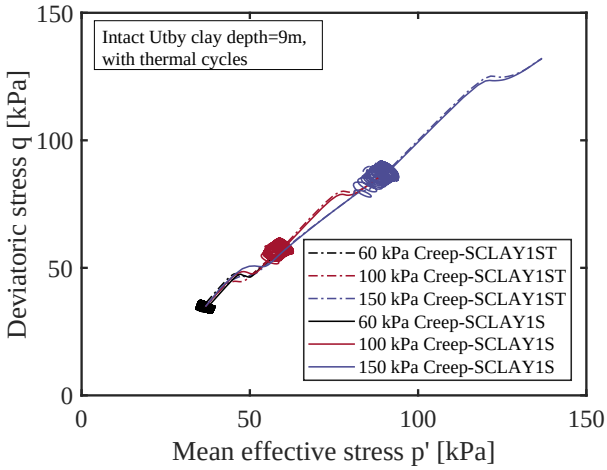

Figure 6.11: Simulated p'-q response for thermal cyclic oedometer tests using Creep-SCLAY1S & Creep-SCLAY1ST.

underpredict the data. In contrast, for stress levels below and beyond, i.e. $\sigma'_v = 60$ & 100 kPa both models underpredict the change void ratio. Crucially, despite the multi-physics simulations with all thermal expansion coefficients and coupling terms, the magnitude of the cyclic amplitude in Δe is not properly captured.

To further analyse the laboratory tests with the temperature-invariant model and temperature-dependent model, the mechanical and thermal cycles steps are plotted in the same time-void ratio plot in Fig. 6.13. The preconsolidated pressure is underestimated by both the temperature-dependent and temperature-invariant model, especially temperature-dependent model at the mechanical loading step just beyond the preconsolidation pressure (the red line in Fig. 6.13).

The differences in the simulated emerging creep rates after thermal cyclic loading are rather small. The results of both the simulations with Creep-SCLAY1S and Creep-SCLAY1ST after 40 simulated thermal cycles are comparable and reasonably close to the experimental data.

The temperature-dependent formulation of the apparent pre-consolidation in Creep-SCLAY1ST leads to a contraction of the reference surface (softening) when the clay is heated. This also leads, in addition to the thermal consolidation effects, to a further increase in excess pore water pressures. The mean effective stress decreases even more. In case the clay is cooled, the effective stress increases due to the generation of suction, as a result the reference surface expands. For a thermal loading cycle that incorporates both heating and cooling, the effects of temperature change is eased by the change of pore pressures for the temperature-dependent model. In contrast, for the temperature-invariant Creep-SCLAY1S model, the reference surface does not change, the stress state simply

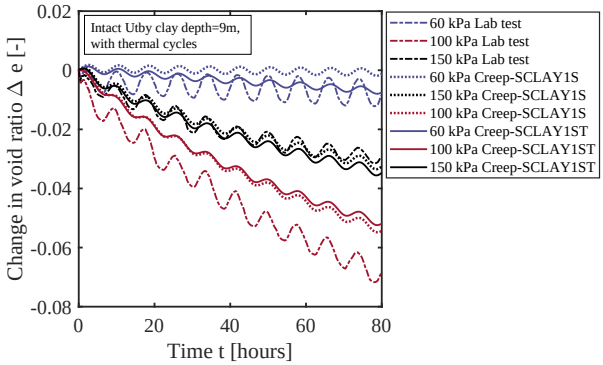

(a) Period=8 hours

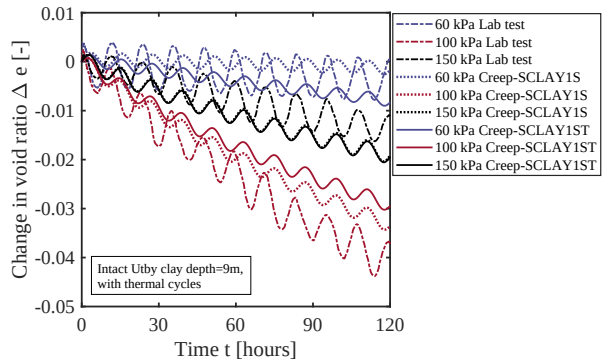

(b) Period=12 hours

Figure 6.12: Simulated time-void ratio curves for thermal cyclic oedometer tests using Creep-SCLAY1S & Creep-SCLAY1ST.

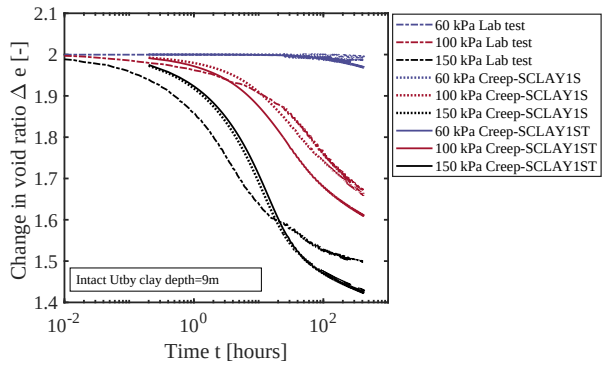

Figure 6.13: Simulated time-compression curves for thermal cyclic oedometer tests using Creep-SCLAY1S & Creep-SCLAY1ST - complete time series for all load steps.

moves within (or outside) the reference surface, and when the clay is heated (or cooled). This can be the explanation for the overprediction of deformations using Creep-SCLAY1S when compared to the simulated results of Creep-SCLAY1ST (Fig. 6.12).

The competing thermal softening and viscoplastic hardening mechanism are most pronounced for when a normally consolidated clay is heated. During heating the decrement in apparent preconsolidation pressure is partially compensated by the viscoplastic strain. This might not be always the case, if for example, the normally consolidated clays are loaded with thermal cycles with a very short loading period t_p, only very limited viscoplastic strain would develop that compensate for the thermal softening, because of the accumulated excess pore water pressures that lead to a reduction of effective stress. Thus, it is hypothesized that the accumulated viscoplastic strains would be rather small under thermal loading cycles when the pore water pressures cannot dissipate. This scenario might however lead to failure under undrained cyclic loading.

In case of thermal loading cycles with substantially longer loading periods t_p ($>>$ 16 hours) that are more representative for energy foundations, the change in pore water pressures cannot be detected. In this case, heating up a clay deposit with a substantial initial amount of natural bonding χ_0 leads to unfavourable irreversible strains due widening of the (negative) gap between the apparent preconsolidation pressure (after thermal softening which is more severe for large values of χ_0), and the current stress state ($\sigma'_v > \sigma'_{pc}$).

6.3 Discussion

In conclusion, the experimental results indicate that the creep rate is altered by thermal cyclic loading. Based on the test series in this Thesis, the effects are minor and are most pronounced in normally (or sligthly overconsolidated) sensitive clays with a large amount of initial bonding. Thermal loading cycles lead to larger permanent strains than the static heating and cooling paths.

7 Conclusions and recommendations

A systematic series of thermal 1D incremental loading tests on intact and remoulded samples of sensitive clay from two depths have been performed in a temperature range of 5 °C – 25 °C. This involves incremental heating and decremental cooling tests with steps of 5 °C. The focus is on quantifying the effect of temperature change on the emerging creep rate as function of the stress level and the initial structure of the clay. The temperature range (5 °C to 25 °C) studied in this work is representative for geothermal energy foundation in Scandinavia.

The simultaneous testing of comparable samples, and the subsequent reconstruction of compression curves from multiple samples, allows to obtain the data required with a significant reduction in total testing time.

The creep rate for the intact samples has proven to be very sensitive to a temperature change, with the largest effects found for stress levels around the apparent preconsolidation pressure. There is no clear trend in the data, other than that it appears that for most stress levels the creep rate peaks between 10 °C to 15 °C before reducing at 20 °C and 25 °C. These results are corroborated by the thermal cyclic loading tests where the largest change in void ratio are registered for effective stress levels around the apparent preconsolidation pressure. In contrast, the remoulded samples did not show sensitivity to temperature changes in the range of temperatures tested, neither in the static nor cyclic thermal loading tests.

Heating increments show larger changes in the creep rate than the cooling decrements. Both, however, lead to a measurable change of the creep rate in the intact clay samples, whereas the reference tests on remoulded samples of the same clay did not show much sensitivity to a temperature change, regardless of the stress level.

The intrinsic permeability of the material, as derived from the hydraulic conductivity, compensated for temperature effects on the dynamic viscosity and density of the pore water, did not show a clear temperature dependence. The arrangement of macro-structural level pores, through which free water flows, depends more on the mechanical loads rather than on the temperature.

In conclusion, the significant thermal creep triggered in sensitive clays is primarily an effect of the change in the structure of the natural clay, which can be due to micro-structural water transfer (Hueckel 1992) or interaggragate links (Delage and Lefebvre 1984), and is most pronounced around the apparent preconsolidation pressure.

Fully coupled thermo-hydro-mechanical numerical analyses of the experimental results at boundary value level are carried out to study the response of sensitive natural clays. The comparisons between experimental results and the simulations show that the rate-dependent behaviour of natural clays under a moderate temperature change (5-25 ^{o}C) is reasonably well predicted by using the temperature-invariant Creep-SCLAY1S model

implemented in a multi-physics Finite Element framework. For almost normally consolidated highly sensitive clays, however, the model needs to be extended to account for the temperature dependency of the apparent preconsolidation pressure. The latter is shown to be highly dependent on the amount of bonding.

The newly developed Creep-SCLAY1ST model, implemented at boundary value level in the COMSOL multi-physics framework, has a temperature- and bonding -dependent apparent preconsolidation pressure that has been calibrated against the experimental data. The new model improved the accuracy of the predictions of the rate-dependent and temperature-dependent response of intact sensitive clay in static oedometer tests, especially for the stress states just above the preconsolidation pressure.

In addition, oedometer tests with thermal loading cycles have been conducted to simulate the clay response adjacent to geothermal energy foundations. The results show that for thermal loading cycles between 5 and 25 °C, with sequentially increasing loading pediods ranging from 4 to 16 hours, the generated excess pore pressures were < 5 kPa for all stress levels. This value which is ca. 2% of the effective stress level, corroborates the findings of the field test on energy piles at the Utby test site performed by Bergström (2017). In the laboratory tests, the effect of the loading period on the generation of excess pore water pressures and strain seems to be negligible. The modelling of the cyclic tests proved to be unsatisfactory, which can be expected as the model on which Creep-SCLAY1ST is based, also lacks the necessary model features for properly capturing effective stress-driven cyclic loading.

During the long-term utilisation of geothermal energy foundations in sensitive clays, temperature triggered creep will accumulate under the seasonally cyclic thermal loading. The effects are largest for normally consolidated intact clays. Energy piles that remould the soil during pile installation (i.e. displacement piles) will be less likely to trigger additional thermal creep deformations during the operation of the geothermal system, as long as the soil volume affected by temperature changes falls within the disturbed zone resulting from installation.

As the systematic testing done as part of this study is limited to one-dimensional conditions only, it would be prudent to extend the test series to study more comprehensive loading paths. In addition, it would be beneficial to study the effects of temperature changes at different strain rates. Thus, it would be possible to fully understand the temperature-dependency of the apparent preconsolidation pressure, the mobilised stiffness and the emerging strength, and how these are related to the amount of natural bonding in sensitive clays.

Fully coupled multi-physics simulations should be combined with state of the art constitutive models, such as the one developed as part of this research, to extrapolate the monitoring data from full-scale energy foundations in sensitive clays, in order to predict the performance of the foundation over its complete life-time.

Finally, the results suggests that the temperature dependency of sensitive natural clays

originates at the micro-structural level. Hence, the conventional element level geotechnical testing methods should be complemented with new techniques originally developed in Materials Sciences that are able to resolve the mechanism at the relevant scale.

A Appendix A. Calibration of the oedometer cells

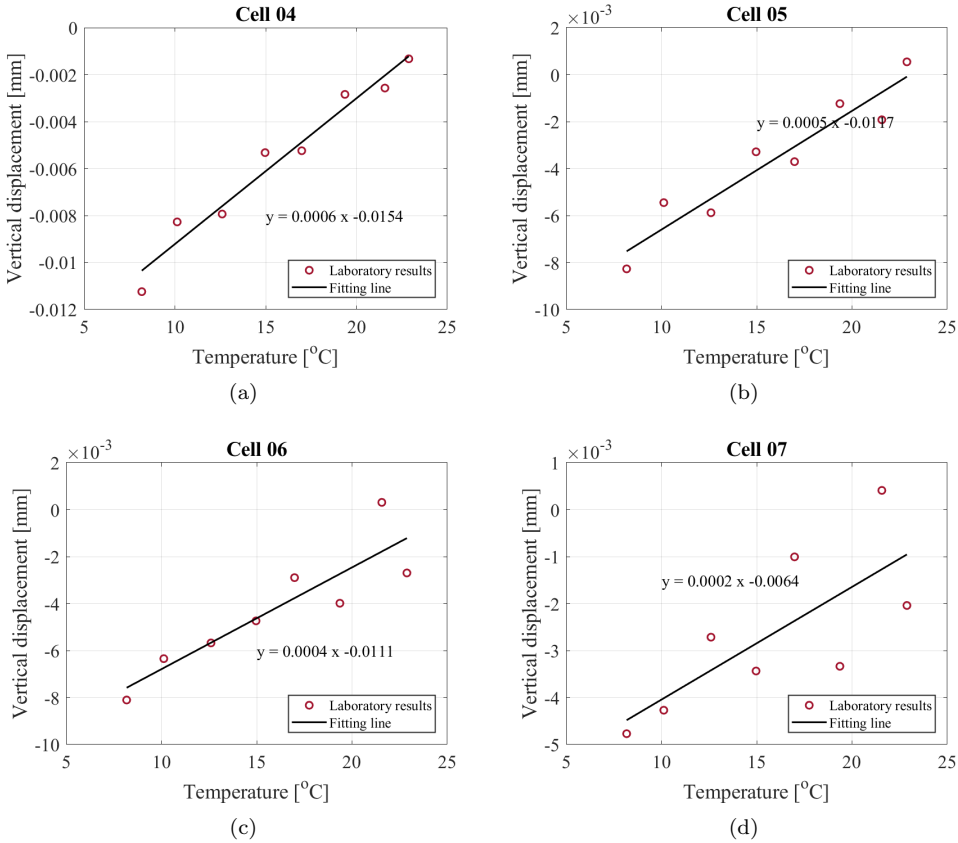

Figure A.1: Calibration on Cell 04 to Cell 07.

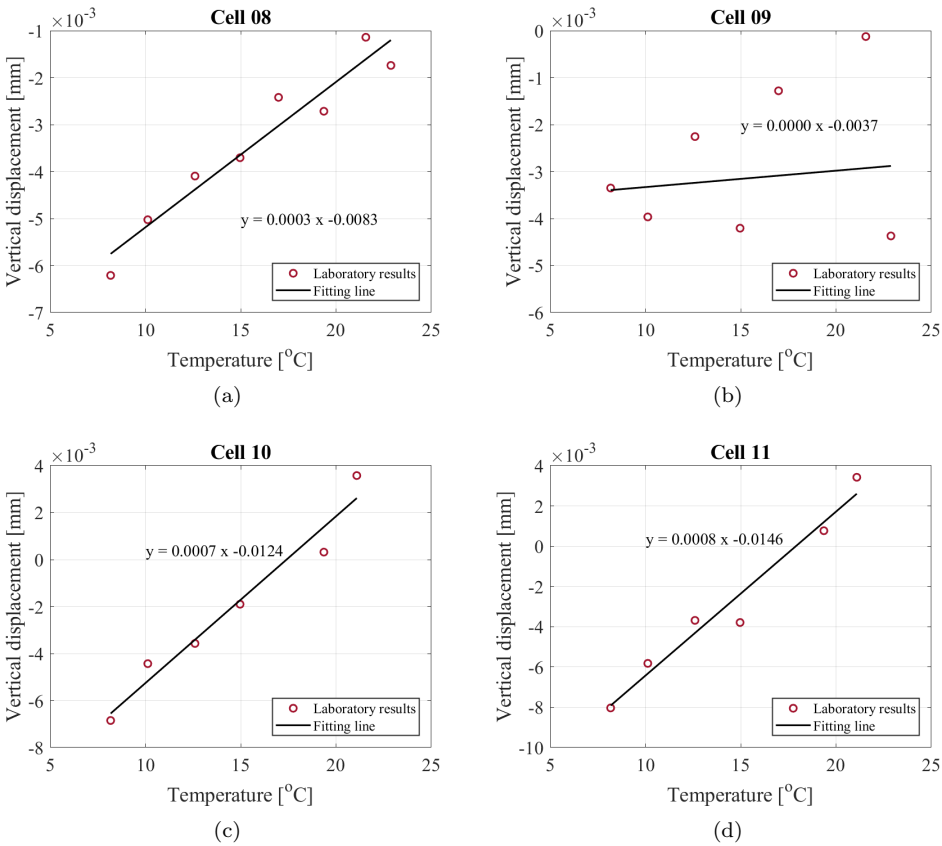

Figure A.2: Calibration on Cell 08 to Cell 11.

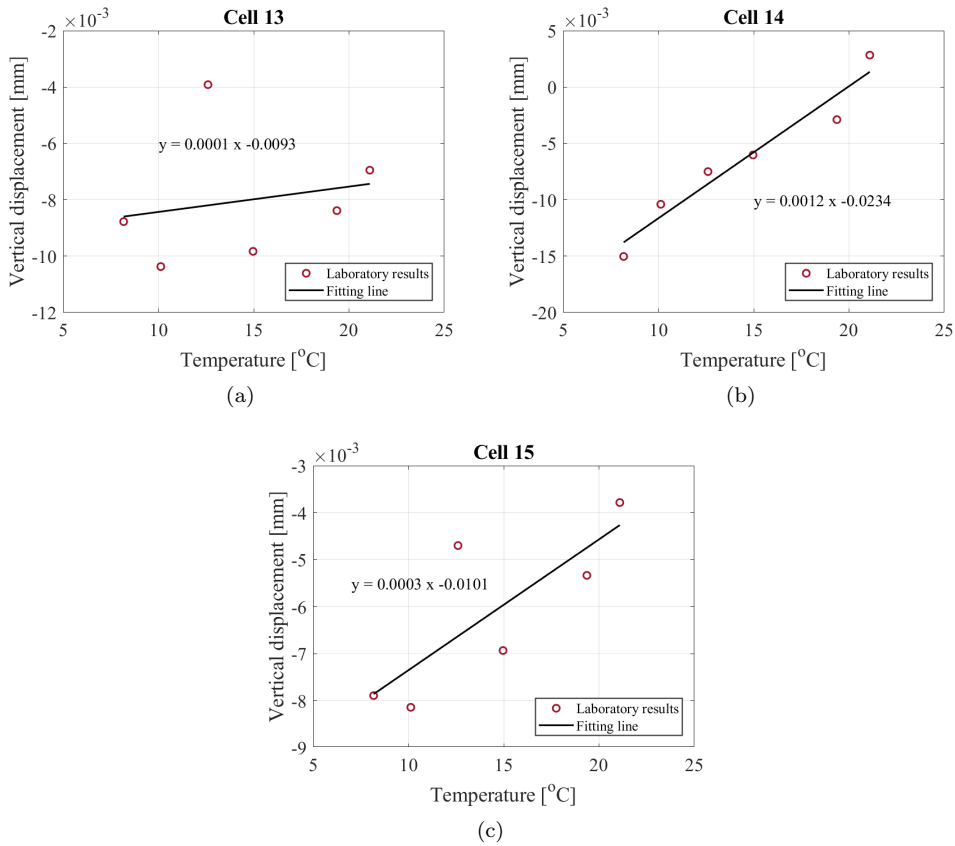

Figure A.3: Calibration on Cell 13 to Cell 15.

B Appendix B. Experimental results with cyclic thermal loading

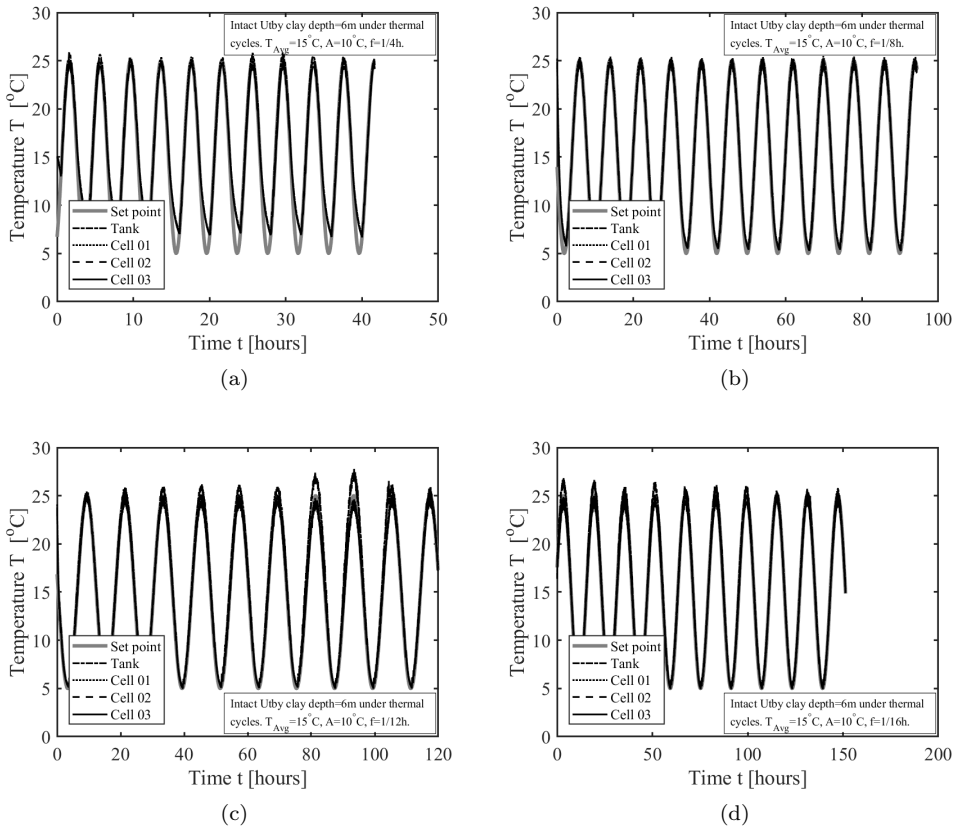

Figure B.1: Temperature in oedometer tests with temperature cycles for intact sample.

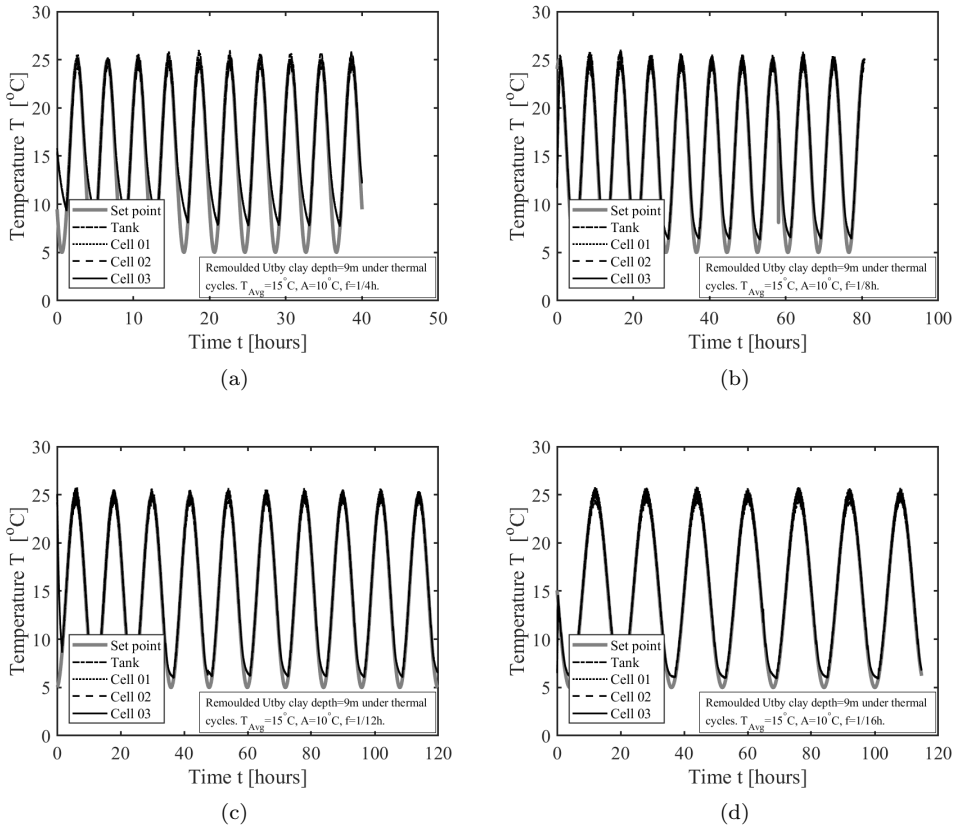

Figure B.2: Temperature in oedometer tests with temperature cycles for remoulded sample.

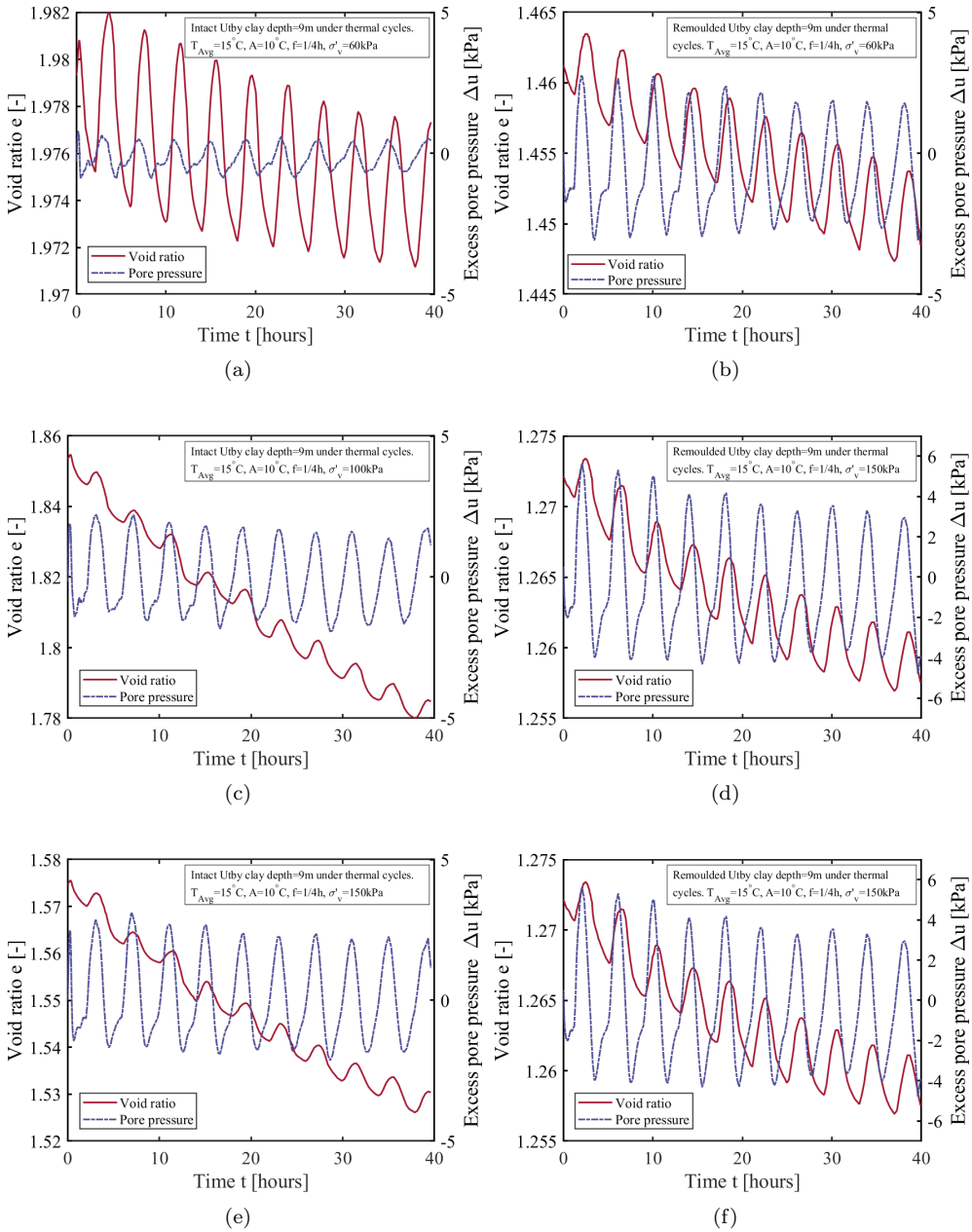

Figure B.3: Pore pressure and void ratio of samples under different stress levels during thermal cycles, t_P =4 hours.

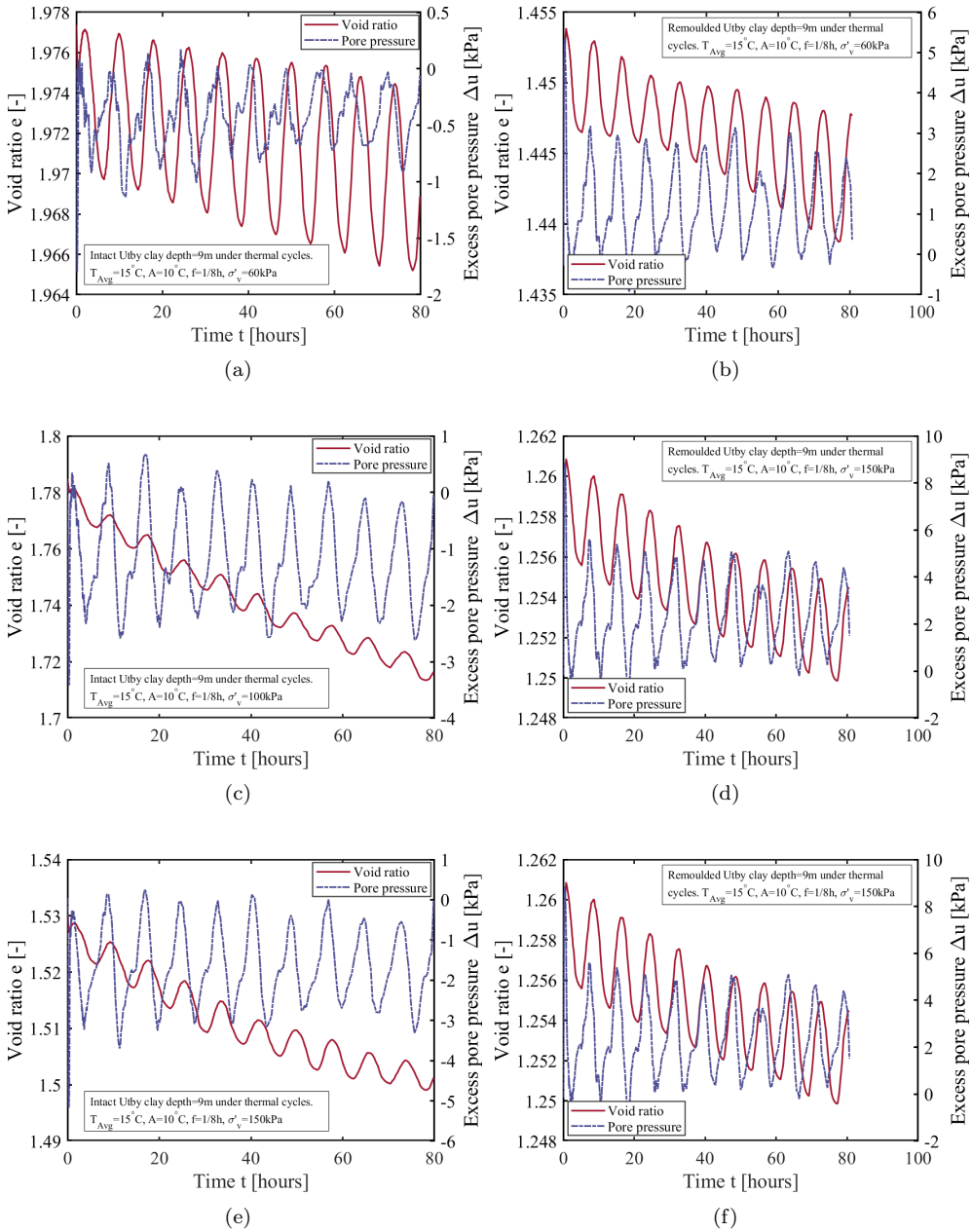

Figure B.4: Pore pressure and void ratio of samples under different stress levels during thermal cycles, t_P =8 hours.

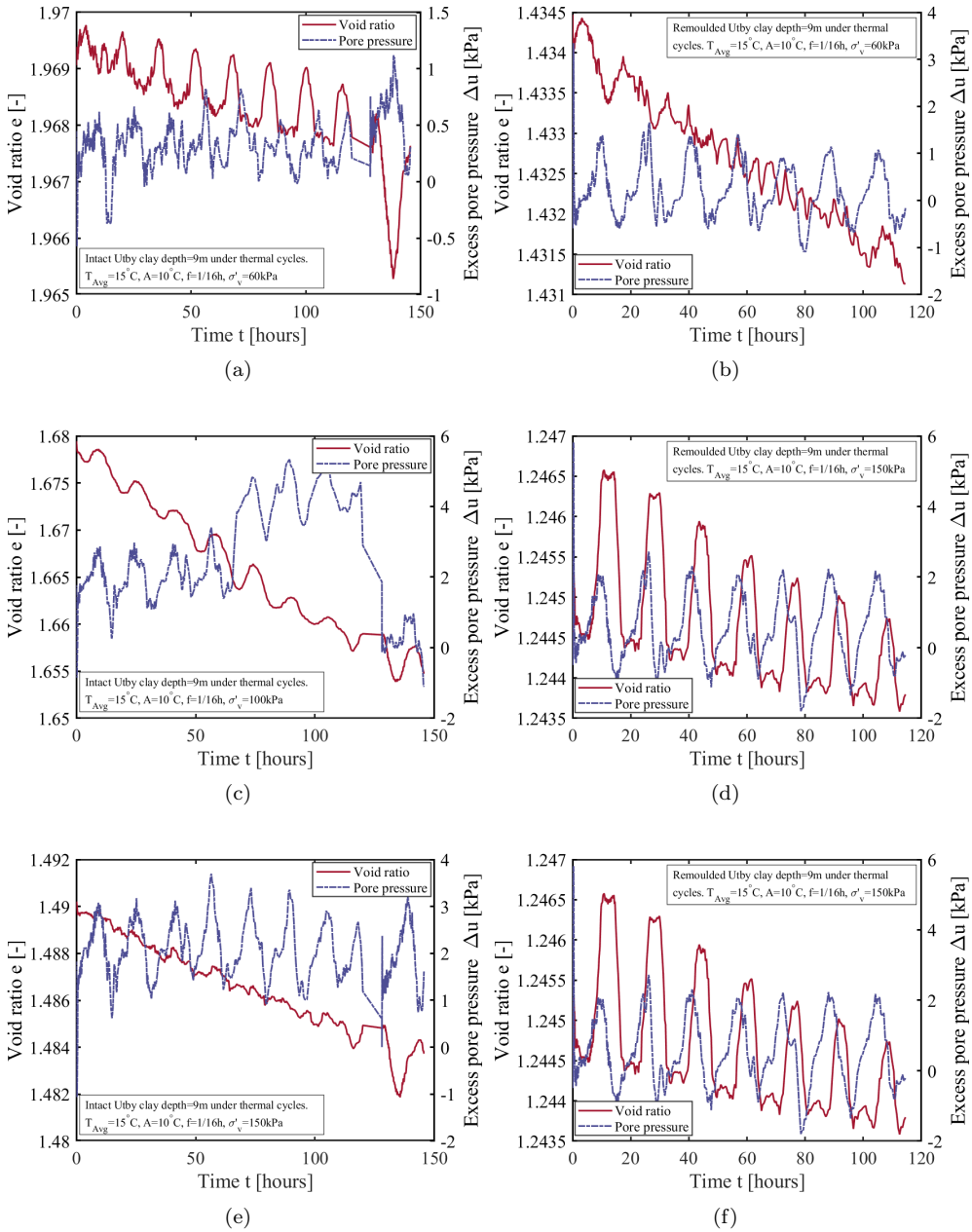

Figure B.5: Pore pressure and void ratio of samples under different stress levels during thermal cycles, t_P =16 hours.

References

Abdelaziz, S. L., Ozudogru, T. Y., Olgun, C. G., & Martin, J. R. (2014). Multilayer finite line source model for vertical heat exchangers. *Geothermics*, *51*, 406–416.

Abuel-Naga, H. M., Bergado, D. T., & Bouazza, A. (2007). Thermally induced volume change and excess pore water pressure of soft Bangkok clay. *Engineering Geology*, *89*(1), 144–154.

Abuel-Naga, H. M., Bergado, D. T., & Bouazza, A. (2008). Thermal conductivity evolution of saturated clay under consolidation process. *International Journal of Geomechanics*, *8*(2), 114–122.

Abuel-Naga, H. M., Bergado, D. T., Bouazza, A., & Pender, M. (2009). Thermomechanical model for saturated clays. *Geotechnique*, *59*(3), 273–278.

Abuel-Naga, H. M., Bergado, D. T., Bouazza, A., & Ramana, G. (2007). Volume change behaviour of saturated clays under drained heating conditions: Experimental results and constitutive modeling. *Canadian Geotechnical Journal*, *44*(8), 942–956.

Abuel-Naga, H. M., Bergado, D. T., & Lim, B. F. (2007). Effect of temperature on shear strength and yielding behavior of soft Bangkok clay. *Soils and Foundations*, *47*(3), 423–436.

Akagi, H., & Komiya, K. (1995). Constant rate of strain consolidation properties of clayey soil at high temperature. In *Proc. Int. Symp. Compression and Consolidation of Clayey Soils–IS–Hiroshima* (Vol. 95, pp. 3–8).

Akrouch, G. A., Sánchez, M., & Briaud, J.-L. (2014). Thermo-mechanical behavior of energy piles in high plasticity clays. *Acta Geotechnica*, *9*(3), 399–412.

Amatya, B., Soga, K., Bourne-Webb, P., Amis, T., & Laloui, L. (2012). Thermo-mechanical behaviour of energy piles. *Géotechnique*, *62*(6), 503–519.

Andersson-Sköld, Y., Torrance, J. K., Lind, B., Odén, K., Stevens, R. L., & Rankka, K. (2005). Quick clay—A case study of chemical perspective in Southwest Sweden. *Engineering Geology*, *82*(2), 107–118.

Arson, C., Berns, E., Akrouch, G., Sanchez, M., & Briaud, J. L. (2013). Heat Propagation around geothermal piles and implications on energy balance. *Energy Book Series*, *1*, 628–635.

Baldi, G., Hueckel, T., & Pellegrini, R. (1988). Thermal volume changes of the mineral-water system in low-porosity clay soils. *Canadian Geotechnical Journal*, *25*(4), 807–825.

Bear, J. (1972). *Dynamics of fluids in porous media*. American Elsevier Publishing Company.

Bergström, A. (2017). *In-situ testing of floating thermal piles in soft sensitive clay*. Licentiate thesis , Chalmers University of Technology, Gothenburg.

Bernier, F., Li, X. L., & Bastiaens, W. (2007). Twenty-five years' geotechnical observation and testing in the Tertiary Boom Clay formation. *Géotechnique*, *57*(2), 229–237.

Boudali, M., Leroueil, S., & Murthy, B. S. (1994). Viscous behaviour of natural clays. In *Proceedings of the International Conference on Soil Mechanics and Foundation Engineering* (Vol. 1, pp. 411–411). AA Balkema.

Bourne-Webb, P. J., Amatya, B., & Soga, K. (2012). A framework for understanding energy pile behaviour. *Proceedings of the ICE-Geotechnical Engineering*, *166*(2), 170–177.

Bourne-Webb, P. J., Amatya, B., Soga, K., Amis, T., Davidson, C., & Payne, P. (2009). Energy pile test at Lambeth College, London: Geotechnical and thermodynamic aspects of pile response to heat cycles. *Géotechnique*, *59*(3), 237–248.

Brandl, H. (2006). Energy foundations and other thermo-active ground structures. *Géotechnique*, *56*(2), 81–122.

Brochard, L., Honório, T., Vandamme, M., Bornert, M., & Peigney, M. (2017). Nanoscale origin of the thermo-mechanical behavior of clays. *Acta Geotechnica*, 1–19.

Burghignoli, A., Desideri, A., & Miliziano, S. (1992). Deformability of clays under non isothermal conditions. *Rivista Italiana di Geotecnica*, *4*, 227–236.

Burghignoli, A., Desideri, A., & Miliziano, S. (2000). A laboratory study on the thermomechanical behaviour of clayey soils. *Canadian Geotechnical Journal*, *37*(4), 764–780.

Campanella, R. G., & Mitchell, J. K. (1968). Influence of temperature variations on soil behavior. *Journal of the Soil Mechanics and Foundations Division*, *94*(3), 609–734.

Cekerevac, C., & Laloui, L. (2004). Experimental study of thermal effects on the mechanical behaviour of a clay. *International Journal for Numerical and Analytical Methods in Geomechanics*, *28*(3), 209–228.

Coccia, C. J. R., & McCartney, J. S. (2016a). Thermal volume change of poorly draining soils i: Critical assessment of volume change mechanisms. *Computers and Geotechnics*, *80*, 26–40.

Coccia, C. J. R., & McCartney, J. S. (2016b). Thermal volume change of poorly draining soils ii: Model development and experimental validation. *Computers and Geotechnics*, *80*, 16–25.

Collins, I. F., & Kelly, P. A. (2002). A thermomechanical analysis of a family of soil models. *Geotechnique*, *52*(7), 507–518.

Cui, Y. J., Sultan, N., & Delage, P. (2000). A thermomechanical model for saturated clays. *Canadian Geotechnical Journal*, *37*(3), 607–620.

Dao, L.-Q., Delage, P., Tang, A.-M., Cui, Y.-J., Pereira, J.-M., Li, X.-L., & Sillen, X. (2014). Anisotropic thermal conductivity of natural Boom Clay. *Applied Clay Science*, *101*, 282–287.

De Bruyn, D., & Thimus, J.-F. (1996). The influence of temperature on mechanical characteristics of Boom clay: the results of an initial laboratory programme. *Engineering Geology*, *41*(1), 117–126.

Dehkordi, S. E., & Schincariol, R. A. (2014). Guidelines and the design approach for vertical geothermal heat pump systems: current status and perspective. *Canadian Geotechnical Journal*, *51*(6), 647–662.

Delage, P., & Lefebvre, G. (1984). Study of the structure of a sensitive Champlain clay and of its evolution during consolidation. *Canadian Geotechnical Journal*, *21*(1), 21–35.

Delage, P., Sultan, N., & Cui, Y. J. (2000). On the thermal consolidation of Boom clay. *Canadian Geotechnical Journal*, *37*(2), 343–354.

Demars, K. R., & Charles, R. D. (1982). Soil volume changes induced by temperature cycling. *Canadian Geotechnical Journal*, *19*(2), 188–194.

Di Donna, A., & Laloui, L. (2015). Response of soil subjected to thermal cyclic loading: Experimental and constitutive study. *Engineering Geology*, *190*, 65–76.

Di Donna, A., Loria, A. F. R., & Laloui, L. (2016). Numerical study of the response of a group of energy piles under different combinations of thermo-mechanical loads. *Computers and Geotechnics*, *72*, 126–142.

Dupray, F., Laloui, L., & Kazangba, A. (2014). Numerical analysis of seasonal heat storage in an energy pile foundation. *Computers and Geotechnics*, *55*, 67–77.

Eriksson, L. (1989). Temperature effects on consolidation properties of sulphide clays. In *International Conference on Soil Mechanics and Foundation Engineering* (pp. 2087–2090). Balkema Publishers, AA/Taylor & Francis, The Netherlands.

Eslami, H., Rosin-Paumier, S., Abdallah, A., & Masrouri, F. (2017). Pressuremeter test parameters of a compacted illitic soil under thermal cycling. *Acta Geotechnica*, *12*(5), 1105–1118.

Florides, G., & Kalogirou, S. (2007). Ground heat exchangers-A review of systems, models and applications. *Renewable Energy*, *32*(15), 2461–2478.

Fox, P. J., & Edil, T. B. (1996). Effects of stress and temperature on secondary compression of peat. *Canadian Geotechnical Journal*, *33*(3), 405–415.

François, B., & Laloui, L. (2010). An oedometer for studying combined effects of temperature and suction on soils. *Geotechnical Testing Journal*, *33*(2), 112–122.

François, B., Laloui, L., & Laurent, C. (2009). Thermo-hydro-mechanical simulation of ATLAS in situ large scale test in Boom clay. *Computers and Geotechnics*, *36*(4), 626–640.

Gabrielsson, A., Lehtmets, M., & Moritz, L. (1997). *Heat Storage in Soft Clay: Field Tests with Heating (70 oC) and Freezing of the Soil*. Swedish Geotechnical Institute.

Gashti, E. H. N., Malaska, M., & Kujala, K. (2014). Evaluation of thermo-mechanical behaviour of composite energy piles during heating/cooling operations. *Engineering Structures*, *75*, 363–373.

Gens, A., & Nova, R. (1993). Conceptual bases for a constitutive model for bonded soils and weak rocks. In *Prof. International Symposium on Hard Soils- Soft Rocks, 1993; Athens* (pp. 485–494). A A Balkema, Rotterdam.

Gens, A., Vaunat, J., Garitte, B., & Wileveau, Y. (2007). In situ behaviour of a stiff layered clay subject to thermal loading: Observations and interpretation. *Géotechnique*, *57*(2), 207–228.

Gera, F., Hueckel, T., & Peano, A. (1996). Critical issues in modelling the long-term hydro-thermomechanical performance of natural clay barriers. *Engineering Geology*, *41*(1), 17–33.

Graham, J., Tanaka, N., Crilly, T., & Alfaro, M. (2001). Modified Cam-Clay modelling of temperature effects in clays. *Canadian Geotechnical Journal*, *38*(3), 608–621.

Gras, J.-P., Sivasithamparam, N., Karstunen, M., & Dijkstra, J. (2017). Strategy for consistent model parameter calibration for soft soils using multi-objective optimisation. *Computers and Geotechnics*, *90*, 164–175.

Gras, J.-P., Sivasithamparam, N., Karstunen, M., & Dijkstra, J. (2018). Permissible range of model parameters for natural fine-grained materials. *Acta Geotechnica*, *13*(2), 387–398.

Grimstad, G. (2009). *Development of effective stress based anisotropic models for soft clays*. PhD thesis, Norges teknisk-naturvitenskapelige universitet, Fakultet for ingeniørvitenskap og teknologi, Institutt for bygg, anlegg og transport.

Gudehus, G., Amorosi, A., Gens, A., Herle, I., Kolymbas, D., Mašín, D., ... Viggiani, G. (2008). The soilmodels.info project. *International Journal for Numerical and Analytical Methods in Geomechanics*, *32*(12), 1571–1572. doi:10.1002/nag.675

Hamidi, A., Tourchi, S., & Khazaei, C. (2014). Thermomechanical Constitutive Model for Saturated Clays Based on Critical State Theory. *International Journal of Geomechanics*, *15*(1), 4014038.

Hansen, E. L., Hemmen, H., Fonseca, D. d. M., Coutant, C., Knudsen, K., Plivelic, T., ... Fossum, J. O. (2012). Swelling transition of a clay induced by heating. *Scientific Reports*, *2*, 618.

Hicher, P. (2016). Experimental study of viscoplastic mechanisms in clay under complex loading. *Géotechnique*, *66*(8), 661–669.

Hong, P. Y., Pereira, J. M., Tang, A. M., & Cui, Y.-J. (2013). On some advanced thermomechanical models for saturated clays. *International Journal for Numerical and Analytical Methods in Geomechanics*, *37*(17), 2952–2971.

Houston, S. L., Houston, W. N., & Williams, N. D. (1985). Thermo-mechanical behavior of seafloor sediments. *Journal of Geotechnical Engineering*, *111*(11), 1249–1263.

Hueckel, T. (1992). Water–mineral interaction in hygromechanics of clays exposed to environmental loads: A mixture-theory approach. *Canadian Geotechnical Journal*, *29*(6), 1071–1086.

Hueckel, T., & Baldi, G. (1990). Thermoplasticity of saturated clays: experimental constitutive study. *Journal of Geotechnical Engineering*, *116*(12), 1778–1796.

Hueckel, T., François, B., & Laloui, L. (2009). Explaining thermal failure in saturated clays. *Géotechnique*, *59*(3), 197–212.

Hueckel, T., & Pellegrini, R. (1991). Thermoplastic modeling of undrained failure of saturated clay due to heating. *Soils and Foundations*, *31*(3), 1–16.

Hueckel, T., & Pellegrini, R. (1992). Effective stress and water pressure in saturated clays during heating–cooling cycles. *Canadian Geotechnical Journal*, *29*(6), 1095–1102.

Hueckel, T., Pellegrini, R., & Del Olmo, C. (1998). A constitutive study of thermo-elasto-plasticity of deep carbonatic clays. *International Journal for Numerical and Analytical Methods in Geomechanics*, *22*(7), 549–574.

Hyodo, M., Yasuhara, K., & Hirao, K. (1992). Prediction of clay behaviour in undrained and partially drained cyclic triaxial tests. *Soils and Foundations*, *32*(4), 117–127.

Jaradat, K. A., Darbari, Z., Elbakhshwan, M., Abdelaziz, S. L., Gill, S. K., Dooryhee, E., & Ecker, L. E. (2017). Heating-freezing effects on the orientation of kaolin clay particles. *Applied Clay Science*, *150*, 163–174.

Jeong, S., Lim, H., Lee, J. K., & Kim, J. (2014). Thermally induced mechanical response of energy piles in axially loaded pile groups. *Applied Thermal Engineering*, *71*(1), 608–615.

Jerbo, A., & Hall, F. (1961). Några synpunkter påhögsensitiva bottniska sediment. *GFF*, *83*(3), 312–313.

Karlsson, M., Emdal, A., & Dijkstra, J. (2016). Consequences of sample disturbance when predicting long-term settlements in soft clay. *Canadian Geotechnical Journal*, *53*(12), 1965–1977.

Karstunen, M., Krenn, H., Wheeler, S. J., Koskinen, M., & Zentar, R. (2005). Effect of anisotropy and destructuration on the behavior of Murro test embankment. *International Journal of Geomechanics*, *5*(2), 87–97.

Kimoto, S., Shahbodagh Khan, B., Mirjalili, M., & Oka, F. (2013). Cyclic elastoviscoplastic constitutive model for clay considering nonlinear kinematic hardening rules and structural degradation. *International Journal of Geomechanics*, *15*(5), A4014005.

Knellwolf, C., Peron, H., & Laloui, L. (2011). Geotechnical analysis of heat exchanger piles. *Journal of Geotechnical and Geoenvironmental Engineering*, *137*(10), 890–902.

Korson, L., Drost-Hansen, W., & Millero, F. J. (1969). Viscosity of water at various temperatures. *The Journal of Physical Chemistry*, *73*(1), 34–39.

Kuntiwattanakul, P., Towhata, I., Ohishi, K., & Seko, I. (1995). Temperature effects on undrained shear characteristics of clay. *Soils and Foundations*, *35*(1), 147–162.

Kutter, B., & Sathialingam, N. (1992). Elastic-viscoplastic modelling of the rate-dependent behaviour of clays. *Géotechnique*, *42*(3), 427–441.

Laloui, L., & Cekerevac, C. (2003). Thermo-plasticity of clays: an isotropic yield mechanism. *Computers and Geotechnics*, *30*(8), 649–660.

Laloui, L., & Cekerevac, C. (2008a). Non-isothermal plasticity model for cyclic behaviour of soils. *International Journal for Numerical and Analytical Methods in Geomechanics*, *32*(5), 437.

Laloui, L., & Cekerevac, C. (2008b). Numerical simulation of the non-isothermal mechanical behaviour of soils. *Computers and Geotechnics*, *35*(5), 729–745.

Laloui, L., & Di Donna, A. (2011). Understanding the behaviour of energy geo-structures. In *Proceedings of the Institution of Civil Engineers-Civil Engineering* (Vol. 164, *4*, pp. 184–191). Thomas Telford Ltd.

Laloui, L., & François, B. (2009). ACMEG-T: soil thermoplasticity model. *Journal of engineering mechanics*, *135*(9), 932–944.

Laloui, L., Leroueil, S., & Chalindar, S. (2008). Modelling the combined effect of strain rate and temperature on one-dimensional compression of soils. *Canadian Geotechnical Journal*, *45*(12), 1765–1777.

Laloui, L., Nuth, M., & Vulliet, L. (2006). Experimental and numerical investigations of the behaviour of a heat exchanger pile. *International Journal for Numerical and Analytical Methods in Geomechanics*, *30*(8), 763–781.

Leroueil, S., Kabbaj, M., Tavenas, F., & Bouchard, R. (1985). Stress–strain–strain rate relation for the compressibility of sensitive natural clays. *Géotechnique*, *35*(2), 159–180.

Leroueil, S., & Soares Marques, M. E. (1996). Importance of strain rate and temperature effects in geotechnical engineering. In *Measuring and Modeling Time Dependent Soil Behavior* (pp. 1–60). ASCE.

Leroueil, S., & Vaughan, P. (1990). The general and congruent effects of structure in natural soils and weak rocks. *Géotechnique*, *40*(3), 467–488.

Li, Y., Dijkstra, J., & Karstunen, M. (2018). Thermomechanical creep in sensitive clays. *Journal of Geotechnical and Geoenvironmental Engineering*, *144*(11), 04018085.

Lingnau, B., Graham, J., & Tanaka, N. (1995). Isothermal modeling of sand-bentonite mixtures at elevated temperatures. *Canadian Geotechnical Journal*, *32*(1), 78–88.

Lingnau, B., Graham, J., Yarechewski, D., Tanaka, N., & Gray, M. (1996). Effects of temperature on strength and compressibility of sand-bentonite buffer. *Engineering Geology*, *41*(1-4), 103–115.

Liu, E. L., & Xing, H. L. (2009). A double hardening thermo-mechanical constitutive model for overconsolidated clays. *Acta Geotechnica*, *4*(1), 1–6.

Loveridge, F. A., & Powrie, W. (2013). Pile heat exchangers: thermal behaviour and interactions. In *Proceedings of the Institute of Civil Engineers: Geotechnical Engineering* (Vol. 166, *2*, pp. 178–196).

Lunne, T., Berre, T., & Strandvik, S. (1997). Sample disturbance effects in soft low plastic Norwegian clay. In *Symposium on Recent Developments in Soil and Pavement Mechanics*.

Ma, C., & Hueckel, T. (1993). Thermomechanical effects on adsorbed water in clays around a heat source. *International Journal for Numerical and Analytical Methods in Geomechanics*, *17*(3), 175–196.

Marques, M. E. S., Leroueil, S., & Soares de Almeida, M. d. S. (2004). Viscous behaviour of st-roch-de-l'achigan clay, quebec. *Canadian Geotechnical Journal*, *41*(1), 25–38.

McCartney, J. S., & Rosenberg, J. E. (2011). Impact of heat exchange on side shear in thermo-active foundations. In *Geo-Frontiers 2011: Advances in Geotechnical Engineering* (pp. 488–498).

McCartney, J. S., Sanchez, M., & Tomac, I. (2016). Energy geotechnics: Advances in subsurface energy recovery, storage, exchange, and waste management. *Computers and Geotechnics*, *75*, 244–256.

Mimouni, T., & Laloui, L. (2014). Towards a secure basis for the design of geothermal piles. *Acta Geotechnica*, *9*(3), 355–366.

Mitchell, J. K. (1969). Temperature effects on the engineering properties and behavior of soils. *Highway Research Board Special Report*, (103).

Mitchell, J. K., & Soga, K. (2005). *Fundamentals of soil behavior*. Wiley New York.

Modaressi, H., & Laloui, L. (1997). A thermo-viscoplastic constitutive model for clays. *International Journal for Numerical and Analytical Methods in Geomechanics*, *21*(5), 313–335.

Moritz, L. (1995). *Geotechnical properties of clay at elevated temperatures*. Swedish Geotechnical Institute, Linköping, Sweden.

Navarro, V., & Alonso, E. (2001). Secondary compression of clays as a local dehydration process. *Géotechnique*, *51*(10), 859–869.

Nguyen, V. T., Tang, A. M., & Pereira, J.-M. (2017). Long-term thermo-mechanical behavior of energy pile in dry sand. *Acta Geotechnica*, 729–737.

Noble, C. A., & Demirel, T. (1969). Effect of temperature on strength behavior of cohesive soil. In *Int. Conf. Effects of Temperature and Heat on Engineering Behaviour of Soils. Highway Res. Board Publ* (pp. 204–219).

Olsson, M. (2013). *On rate-dependency of Gothenburg clay*. PhD thesis, Chalmers University of Technology, Gothenburg.

Pasten, C., & Santamarina, J. C. (2014). Thermally induced long-term displacement of thermoactive piles. *Journal of Geotechnical and Geoenvironmental Engineering*, *140*(5), 06014003.

Pasten, C., Shin, H., & Santamarina, J. C. (2013). Long-term foundation response to repetitive loading. *Journal of Geotechnical and Geoenvironmental Engineering*, *140*(4), 04013036.

Plum, R. L., & Esrig, M. I. (1969). Some temperature effects on soil compressibility and pore water pressure. *Special Report-Highway Research Board*, (103), 231.

Popiel, C. O., Wojtkowiak, J., & Biernacka, B. (2001). Measurements of temperature distribution in ground. *Experimental thermal and fluid science*, *25*(5), 301–309.

Rankka, K., Andersson-Sköld, Y., Hultén, C., Larsson, R., Leroux, V., & Dahlin, T. (2004). Quick clay in Sweden. *Swedish Geotechnical Institute Report*, *65*.

Robinet, J.-C., Rahbaoui, A., Plas, F., & Lebon, P. (1996). A constitutive thermomechanical model for saturated clays. *Engineering Geology*, *41*(1), 145–169.

Sagaseta, C., & Whittle, A. J. (2001). Prediction of ground movements due to pile driving in clay. *Journal of Geotechnical and Geoenvironmental Engineering*, *127*(1), 55–66.

Salciarini, D., Ronchi, F., & Tamagnini, C. (2017). Thermo-hydro-mechanical response of a large piled raft equipped with energy piles: A parametric study. *Acta Geotechnica*, *12*(4), 703–728.

Savvidou, C., & Britto, A. (1995). Numerical and experimental investigation of thermally induced effects in saturated clay. *Soils and Foundations*, *35*(1), 37–44.

Sherif, M. A., & Burrous, C. M. (1969). Temperature effects on the unconfined shear strength of saturated, cohesive soil. *Highway Research Board Special Report*, (103).

Sivasithamparam, N., Karstunen, M., & Bonnier, P. (2015). Modelling creep behaviour of anisotropic soft soils. *Computers and Geotechnics*, *69*, 46–57.

Sultan, N., Delage, P., & Cui, Y. (2002). Temperature effects on the volume change behaviour of Boom clay. *Engineering Geology*, *64*(2), 135–145.

Suryatriyastuti, M. E., Mroueh, H., & Burlon, S. (2012). Understanding the temperature-induced mechanical behaviour of energy pile foundations. *Renewable and Sustainable Energy Reviews*, *16*(5), 3344–3354.

Suryatriyastuti, M. E., Mroueh, H., & Burlon, S. (2014). A load transfer approach for studying the cyclic behavior of thermo-active piles. *Computers and Geotechnics*, *55*, 378–391.

Tanaka, N., Graham, J., & Crilly, T. (1997). Stress-strain behaviour of reconstituted illitic clay at different temperatures. *Engineering Geology*, *47*(4), 339–350.

Tarnawski, V. R., & Wagner, B. (1991). TheHyProS: Thermal and hydraulic properties of soils. Thermal Energy System. *Computer Analysis and Design*.

Tidfors, M., & Sällfors, G. (1989). Temperature effect on preconsolidation pressure. *Geotechnical Testing Journal*, *12*(1), 93–97.

Towhata, I., Kuntiwattanakul, P., & Kobayashi, H. (1993). A preliminary study on heating of clays to examine possible effects of temperature on soil-mechanical properties. *Soils and Foundations*, *33*(4), 184–190.

Towhata, I., Kuntiwattanakul, P., Seko, I., & Ohishi, K. (1993). Volume change of clays induced by heating as observed in consolidation tests. *Soils and Foundations*, *33*(4), 170–183.

Tsutsumi, A., & Tanaka, H. (2012). Combined effects of strain rate and temperature on consolidation behavior of clayey soils. *Soils and Foundations*, *52*(2), 207–215.

Vieira, A., & Maranha, J. R. (2016). Thermoplastic analysis of a thermoactive pile in a normally consolidated clay. *International Journal of Geomechanics*, *17*(1), 04016030.

Wang, L., Wang, K., & Hong, Y. (2016). Modeling temperature-dependent behavior of soft clay. *Journal of Engineering Mechanics*, *142*(8), 04016054.

Wheeler, S. J., Näätänen, A., Karstunen, M., & Lojander, M. (2003). An anisotropic elastoplastic model for soft clays. *Canadian Geotechnical Journal*, *40*(2), 403–418.

Yannie, J. (2016). *On the long-term behaviour of tension loaded piles in natural soft soils.* PhD thesis, Chalmers University of Technology, Gothenburg.

Yavari, N., Tang, A. M., Pereira, J.-M., & Hassen, G. (2016). Effect of temperature on the shear strength of soils and the soil–structure interface. *Canadian Geotechnical Journal*, *53*(7), 1186–1194.

Ye, W. M., Zhang, Y. W., Chen, Y. G., Chen, B., & Cui, Y. J. (2013). Experimental investigation on the thermal volumetric behavior of highly compacted GMZ01 Bent. *Applied Clay Science*, *83*, 210–216.

Yin, Z.-Y., Karstunen, M., Chang, C. S., Koskinen, M., & Lojander, M. (2011). Modeling time-dependent behavior of soft sensitive clay. *Journal of Geotechnical and Geoenvironmental Engineering*, *137*(11), 1103–1113.

Zhang, F., Zhang, Z. Z., Low, P. F., & Roth, C. B. (1993). The effect of temperature on the swelling of montmorillonite. *Clay Minerals*, *28*, 25.

Zhou, C., & Ng, C. W. W. (2015). A thermomechanical model for saturated soil at small and large strains. *Canadian Geotechnical Journal*, *52*(8), 1101–1110.

Zymnis, D. M., Whittle, A. J., & Cheng, X. (2018). Simulation of long-term thermo-mechanical response of clay using an advanced constitutive model. *Acta Geotechnica*, 1–17.